Development and application of in-fibre Bragg grating contact force sensors for application to the human hip

by

Christopher Raymond Stuart Dennison
B.Eng., University of Victoria, 2006
M.A.Sc., University of Victoria, 2008

A Dissertation Submitted in Partial Fulfillment
of the Requirements for the Degree of

DOCTOR OF PHILOSOPHY

in the Department of Mechanical Engineering

Supervisory Committee

Development and application of in-fibre Bragg grating contact force sensors for application to the human hip

by

Christopher Dennison
B.Eng., University of Victoria, 2006
M.A.Sc., University of Victoria, 2008

Supervisory Committee

Dr. Peter Wild, Department of Mechanical Engineering
Supervisor

Dr. Martin Jun, Department of Mechanical Engineering
Departmental Member

Dr. Bradley Buckham, Department of Mechanical Engineering
Departmental Member

Dr. Thomas Darcie, Department of Electrical and Computer Engineering
Outside Member

Abstract

Supervisory Committee
Dr. Peter Wild, Department of Mechanical Engineering
Supervisor
Dr. Martin Jun, Department of Mechanical Engineering
Departmental Member
Dr. Bradley Buckham, Department of Mechanical Engineering
Departmental Member
Dr. Thomas Darcie, Department of Electrical and Computer Engineering
Outside Member

This dissertation presents contact force sensors that are based on an emerging fibre-optic sensing technology, the in-fibre Bragg grating (FBG), for contact force measurements between cartilage surfaces in the human hip. There are two main motivations for force measurement in hips (and other joints). First, there is clinical evidence that suggests excessive force magnitude and duration can cause painful degeneration of joints. Second, insights from *ex vivo* force measurements during simulated physiologic loading are the basis of the rationale for corrective surgeries meant to halt degeneration and restore proper joint function by restoring natural joint mechanics. The current standard tools for force measurements in joints are force/stress sensitive films.

There are problems associated with inserting these films into joints that affect the force/stress measurements. To insert the films, the joint must be dissected of surrounding soft tissues and, ultimately, the joint must be taken apart (disarticulated). Following disarticulation, films are fixed to cartilage surfaces, and the joint is re-assembled so that physiologic loads can be applied. The negative consequence of dissection and disarticulation is that the natural mechanics of the intact joint are permanently lost and, therefore, film measurements do not indicate the actual joint mechanics. Moreover,

covering cartilage surfaces with rigid films alters the natural contact mechanics of the joint.

The force sensors presented in this dissertation are designed for *local force measurement* over the region of the optical fibre containing the FBG and address limitations of force/stress sensitive films. The FBG force sensors are extremely small (major diameters ranging from 0.165 mm to 0.24 mm) and can be inserted into joint spaces without dissection of soft tissues and disarticulation thereby allowing the joint to remain intact. Theoretical and experimental results indicate that FBG sensor measurements are less affected by the mechanical properties of cartilage than are film sensors.

The sensors presented in this dissertation also address limitations with previous FBG based force sensors and are the first application of FBGs in intact human hips. The sensors are smaller, and therefore less invasive, and insensitive to orientation, axial strain and temperature, unlike other FBG sensors presented in the literature.

Table of Contents

Supervisory Committee ii
Abstract iii
Table of Contents v
List of Figures vi
Acknowledgments viii
Chapter 1: Introduction 1
1.1 Introduction 1
1.2 Overview of hip anatomy, mechanics and clinical motivations for research 1
1.3 Review of force/stress measurement techniques and limitations 7
1.4 Objectives 13
1.5 Organization of dissertation 14
Chapter 2: In-fibre Bragg gratings (FBGs) 16
2.1 Principles of optical fibre and FBGs 16
2.2 Stress-optic and strain-optic principles 23
2.3 Pragmatic considerations: force sensing in the hip with FBGs 27
Chapter 3: Contributions 30
3.1 Characterization of FBGs for conforming contacts and demonstration of modulus-independent contact-force measurements 30
3.2 Development of a contact-force sensor with modulus- and orientation-independent sensitivity and application to cadaveric human hips 32
3.3 Development of a contact force sensor without co-sensitivity to axial strain and temperature 35
Chapter 4: Conclusions and future work 38
4.1 Conclusions and summary of contributions 38
4.2 Future work 40
Bibliography 43
Appendix A: Sensitivity of Bragg gratings in birefringent optical fibre to transverse compression between conforming materials 52
Appendix B: An in-fibre Bragg grating sensor for contact force and stress measurements in articular joints 88
Appendix C: A super-structured fibre-optic contact force sensor with minimal co-sensitivity to temperature and axial strain 133

List of Figures

Figure 1-1: joint models with soft-tissues omitted showing: a) antero-lateral view of bone model showing articulating region of hip and anatomy; b) antero-lateral exploded view of hip showing cartilage surfaces of acetabulum and femur as well as bone envelope for acetabular fossa; c) lateral view of flexion-extension path of femur relative to fixed pelvis. Section plane A-A also shown (refer to Figure 1-2); d) anterior view of abduction-adduction path and internal rotation axis; e) postero-lateral view showing fibrocartilagenous labrum fixed to acetabulum; f) inferior view of pelvis showing internal acetabulum and labrum with inferior transition..... 3

Figure 1-2: a) section A-A (refer to Figure 1-1c) showing bone and soft tissue anatomy including joint capsule, synovial fluid spaces and fossa as well as forces transmitted across joint; b) schematic showing cartilage to cartilage contact and contact stresses over the cartilage contact length. Hydrostatic pressures in the central synovial fluid space (refer to a)) also contribute to force equilibrium across the joint space. 5

Figure 1-3: a) Capacitive Novel AJP sensor system (Novel GmbH, Munich, Germany). Sensing area is rectangular tip at end of slender support connected to data acquisition cable. b) Resistive Tekscan sensor system (Tekscan®, Boston, MA). Sensing area is square and located at end of the flexible support connected to data acquisition cable. Reproduced with permission from Clinical Orthopaedics and Related Research© [26]. .. 8

Figure 1-4: a) Tekscan sensor inserted into the capsule of cadaveric spine facet joint. Image reproduced with permission from the Journal of Biomechanics© [33]; b) Tekscan inserted between condyles of cadaveric tibial plateau. Image reproduced with permission from the Journal of Biomechanics© [31]. 10

Figure 1-5: a) image showing Fuji Prescale affixed to femoral head. Prescale shown is pre-cut to allow film to conform to femoral head, while avoiding wrinkling of film. Before joint was loaded and contact stresses were measured, the femoral head with Prescale was inserted into the acetabulum (b) that houses the femoral head in the natural joint. Image reproduced with permission from the Journal of Orthopaedic Trauma [35]. 10

Figure 1-6: a) Pre-cut Prescale film positioned above the cartilage surface of femoral head; b) Peak stress recordings on Prescale film. Stress magnitudes may be inferred from color scale. Reproduced with kind permission from Springer Science+Business Media: Unfallchirurg, Quantitative bestimmung der druckverteilung im huftgelenk wahrend des gangzyklus, 102, 1999, 625-631, Eisenhart-Roth, R.v., Witte, H., Steinlechner, M., Muller-Gerbl, M., Putz, R., Eckstein, F., Figures 3 and 4, ©Springer-Verlag 1999. 11

Figure 2-1: a) schematic (not to scale) showing relevant features of conventional single-mode fibre. A plane electromagnetic light wave [40] propagates and is retained within the core of the fibre. Inset cross section of fibre (to scale) shows relative sizes of fibre core

and clad. Hatched ellipses along fibre core represent a Bragg grating comprising regions of modified refractive index; b) representative refractive index profile along the length of the Bragg grating. The hatched ellipses shown in a) correspond to the locations along the axis z where the refractive index increases from n_0 to n'; c) representative reflected spectrum of FBG; d) typical equipment configuration used to illuminate FBG and measure Bragg wavelength. 17

Figure 2-2: a) schematics of Bow Tie birefringent fibre and D-shape birefringent fibre showing refractive indices along slow and fast axes; b) representative Bragg spectra reflected from a Bragg grating inscribed in a birefringent fibre. 22

Figure 2-3: a) schematic showing contact forces applied to the clad of optical fibre. Both conventional (left) and Bow Tie birefringent (right) fibre cross sections are shown; b) representative plots showing typical changes in the Bragg spectrum for (left) conventional fibre and (right) birefringent fibre that result from applied contact forces. 27

Figure 4-1: schematic hip cross-section showing force sensor inserted through access bore in acetabulum and embedded into the cartilage of the acetabulum. 42

Acknowledgments

This completion of this dissertation is a result of the support of several people who offered both professional and personal encouragement. Dr. Peter Wild, my supervisor, provided professional and personal guidance and support throughout every aspect of this work. He also challenged me, in particular on topics related to writing, to continuously improve and strive to provide the clearest and most accessible presentation of academic writing to a broad audience. Guidance was also provided by Drs. David Wilson and Mike Gilbart (UBC) to establish context and motivation for the work.

I would also like to acknowledge financial support from the Natural Sciences and Engineering Research Council of Canada.

It is impossible to articulate all the ways in which Lindsay made this dissertation possible. Actually, without her, this dissertation would not exist.

Chapter 1: Introduction

1.1 Introduction

This dissertation describes the optical and mechanical design, modeling and validation of FBG contact force/stress sensors as well as application of the sensors in biomechanical pilot experiments in cadaveric hips. The work in this dissertation spans optics, mechanics, design, and biomechanics disciplines. To put the objectives of this dissertation into context, an overview of the mechanics of force/stress in the hip, as well as clinical and biomechanical motivations for contact force/stress measurements, is given in Section 1.1.2 because they guide sensor design, modeling and validation described in subsequent sections. In Section 1.2, a literature review of existing force/stress sensing technologies is included because the limitations of these technologies also guide sensor design and modeling.

1.2 Overview of hip anatomy, mechanics and clinical motivations for research

The hip is a ball-and-socket joint [1] that allows relative motion between the pelvis and femur (Figure 1-1a). The relative motion is defined for three rotational degrees of freedom: flexion/extension anteriorly to posteriorly (Figure 1-1c); abduction/adduction laterally to medially (Figure 1-1d); and internal rotation about the superior-to-inferior axis (Figure 1-1d). Articulation is between the acetabulum of the pelvis and the femoral head (Figure 1-1a and 1-1b).

The articular cartilage surfaces of the acetabulum and femoral head are comprised of hyaline cartilage which has a low coefficient of friction (Figure 1-1b). This cartilage is comprised of a collagenous solid matrix with interconnected pores that contain joint

lubricating synovial fluid [2]. The mechanical properties of cartilage can vary over a considerable range. For example, in studies where cartilage strains are assumed infinitesimal, linear elastic modulus values have been estimated to range, nominally, from 0.5 MPa [2] to 20 MPa [3]. However, in studies where strain magnitudes are finite (or large relative to infinitesimal strains), non-linear elastic models based on strain energy density are used [4]. Among the many non-linear models, the two-parameter Mooney-Rivlin formulation has been shown to closely approximate the non-linear elastic behavior of cartilage [5-7]. Like the linear-elastic modulus of cartilage, the two Mooney-Rivlin parameters, that have the same units as modulus, can also vary over a considerable range from, nominally, 0.3 MPa to 4 MPa.

Between the cartilage surfaces of the acetabulum and femoral head is a central synovial fluid space (Figure 1-2a). The synovial fluid in the porous matrix of the cartilage and central space are in fluid contact. Synovial fluid is retained in the central space by the labrum (Figure 1-1e and 1-1f and Figure 1-2a), a fibrocartilagenous lip that is attached the acetabulum. The labrum spans the superior rim of the acetabulum (Figure 1-1e and Figure 1-2a) and inferiorly transitions smoothly into the transverse ligament (Figure 1-1f, ligament shown in cross section of Figure 1-2a) [2]. There is also synovial fluid, outside of the central space, in contact with the regions of the femoral head and femoral neck not covered the labrum. This fluid occupies a peripheral space between the femoral head/neck and interior surface of the fibrous capsule (Figure 1-2a). The fibrous capsule encapsulates the entire joint, both superiorly and inferiorly.

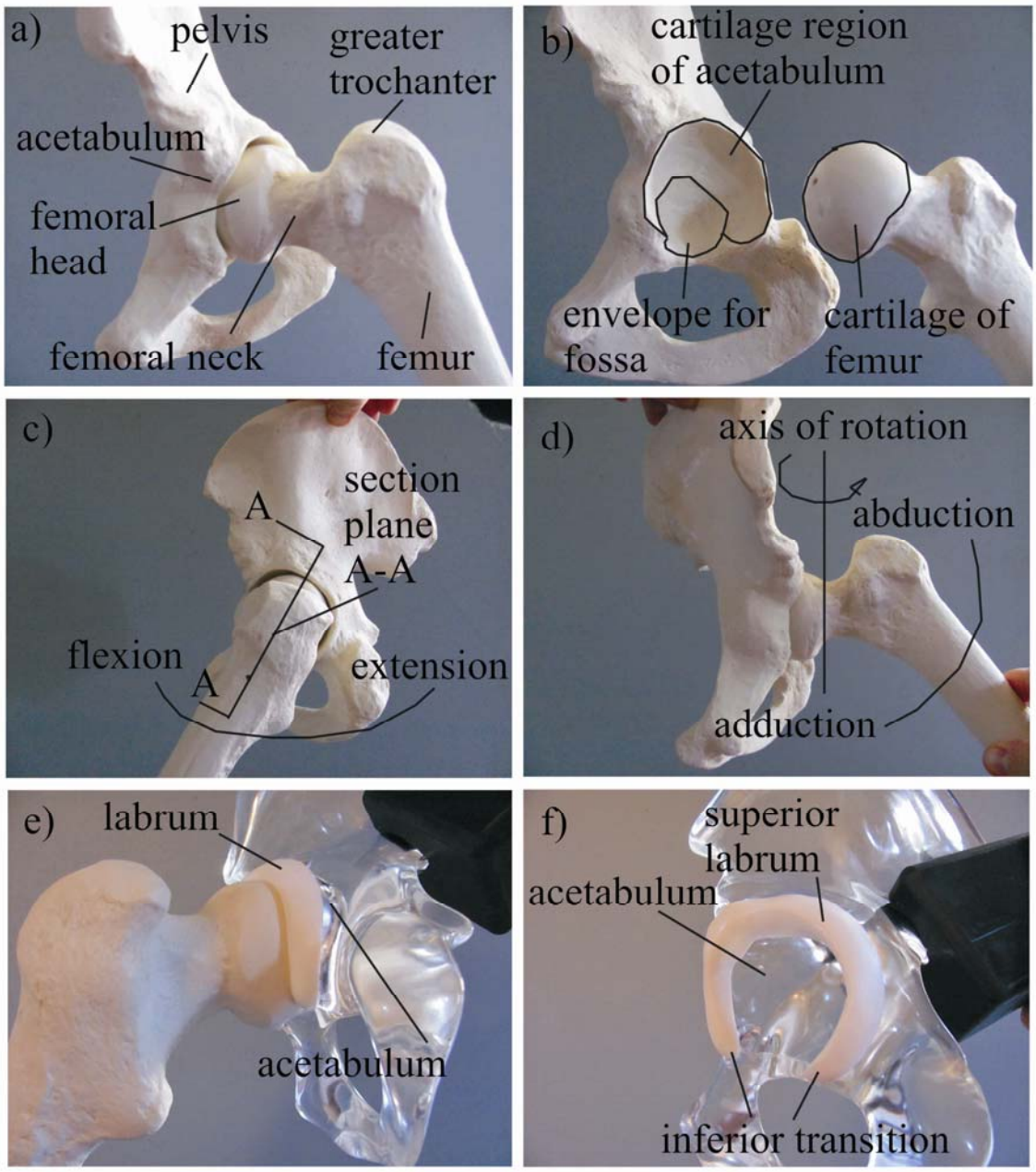

Figure 1-1: joint models with soft-tissues omitted showing: a) antero-lateral view of bone model showing articulating region of hip and anatomy; b) antero-lateral exploded view of hip showing cartilage surfaces of acetabulum and femur as well as bone envelope for acetabular fossa; c) lateral view of flexion-extension path of femur relative to fixed pelvis. Section plane A-A also shown (refer to Figure 1-2); d) anterior view of abduction-adduction path and internal rotation axis; e) postero-lateral view showing fibrocartilagenous labrum fixed to acetabulum; f) inferior view of pelvis showing internal acetabulum and labrum with inferior transition.

Physiologic forces transmitted through the pelvis to the femur can be carried by either hydrostatic pressure of the synovial fluid in the porous matrix and the central space

(Figure 1-2a), or, when cartilage contact between the femoral head and acetabulum occurs, by solid stresses within the porous matrix itself (Figure 1-2b) [2]. The relative proportion of forces carried by each mechanism depends on a wide range of factors, including the force magnitude, the integrity and morphology of joint structures such as the labrum, and the integrity of the cartilage [2]. Today, there is significant clinical interest in the relationship between forces and the integrity of joints because of the potential to improve the understanding of articular joint disorders, and efficacy of clinical orthopaedic treatments that are meant to restore or preserve joint function. Articular joint disorders are the most common of the musculoskeletal disorders [1] and contemporary orthopaedic research is principally concerned with understanding their etiology [8].

Knowledge of *in vivo* forces and the stresses and strains (*i.e.* the mechanics) they induce in the structures of articular joints, such as the knee, hip, ankle and shoulder, is of great value to clinicians, researchers and prosthetic implant designers [9]. Understanding the mechanics is thought to be central in understanding etiology and progression of degenerative joint diseases such as osteoarthritis (OA) [9] as well as the effects of clinical interventions that are meant to halt or slow the progression of joint degeneration [9, 10], and the performance of prosthetic implants [9-15].

OA is a multi-factorial disease that is characterized by degeneration of either, or both, the cartilage surfaces and lubricating synovial fluid of articular joints. The primary mechanism of OA that leads to breakdown of the joint is cartilage damage in the form of tears or thinning. Symptoms include pain, swelling of joints, reduced range of motion and mobility, and joint stiffness. OA affects 10% of Canada's population, with increased

prevalence in the elderly, and is the leading cause of functional limitations in people over 55 years. By the age of 70 years, most Canadians have OA [16].

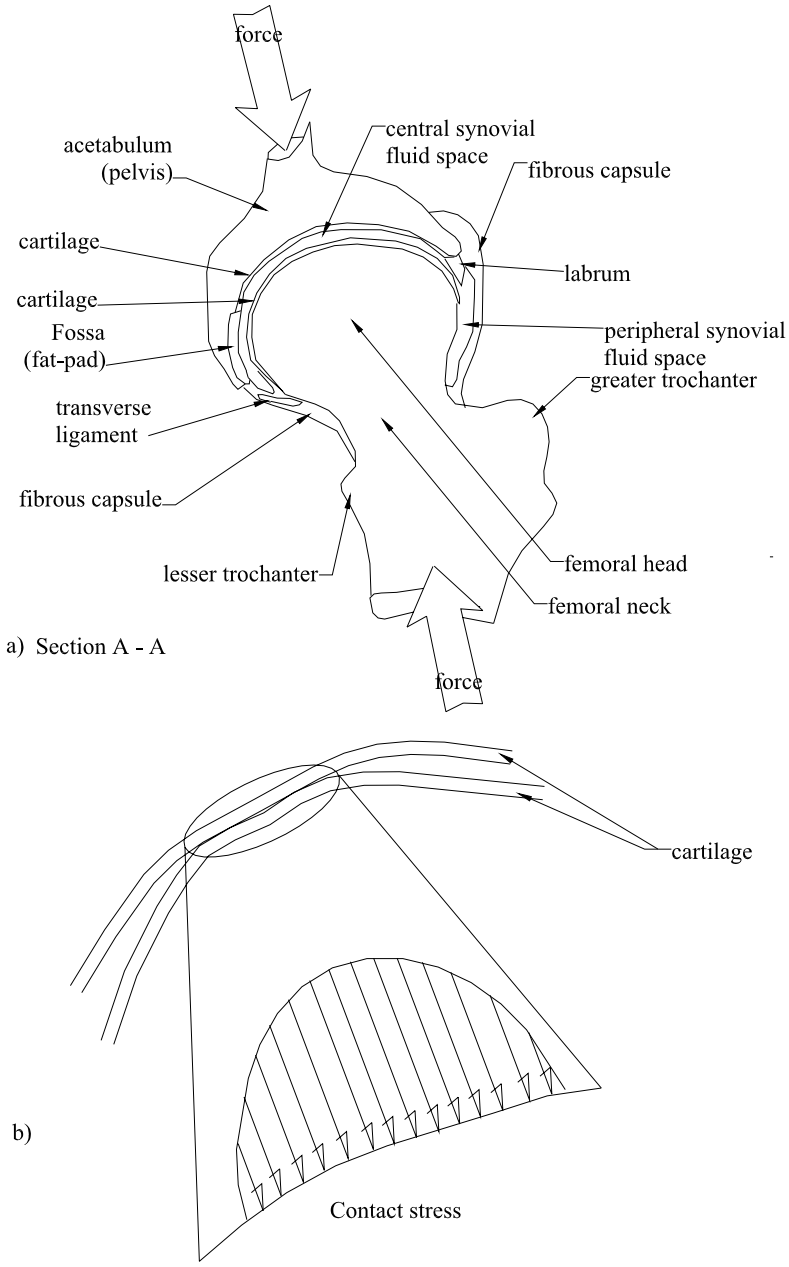

Figure 1-2: a) section A-A (refer to Figure 1-1c) showing bone and soft tissue anatomy including joint capsule, synovial fluid spaces and fossa as well as forces transmitted across joint; b) schematic showing cartilage to cartilage contact and contact stresses over the cartilage contact length. Hydrostatic pressures in the central synovial fluid space (refer to a)) also contribute to force equilibrium across the joint space.

In the case of forces/stresses in hips, it has been demonstrated that excessive duration and magnitude of force/stress on the conforming cartilage layers can cause the onset of OA [17, 18]. As well as forces and stresses, changes in the mechanical structure of the hip including the conforming cartilage layers can provide the necessary stimulus to initiate degenerative processes [19]. Degeneration of the cartilage layers can be influenced by abnormalities of bone, synovial fluid, tendons, ligaments, or soft tissue accessory structures [19]. In the hip joint (Figure 1-2), one such accessory structure is the acetabular labrum. The role of the acetabular labrum in hip mechanics is not well understood but acetabular dysfunction and damage has been clinically linked to the onset of OA [18]. It is also widely believed that clinical symptoms such as pain and cartilage degeneration are related to how force/stress is distributed across the joint [20, 21]. Measurements of force/stress in joints have been done, primarily in dead-tissue (i.e. *ex vivo*), in biomechanics experiments to understand the mechanics of the joint and the role of anatomy in hip mechanics.

Ex vivo measurements of mechanical quantities in cadaver joints are the basis of the mechanical rationale for many conservative and surgical treatments for joint disorders. These have been done in the knee [22] and in the hip [23, 24]. In these studies, cadaveric (*i.e.* dead-tissue) specimens are loaded in test rigs to simulate the physiological loads applied during standing, weight-bearing or activity. Measurements of contact area, force and stress distribution are made between the conforming cartilage surfaces at the joint. Although *ex vivo* studies are limited because a) simplified loading in *ex vivo* studies can only simulate *in vivo* loading conditions and b) morphological adaptations due to the disease process cannot be studied in cadavers, they are still useful

for predicting the immediate effects of treatment on joint mechanics. Unfortunately, currently available sensing technologies are not satisfactory for the reasons expanded upon below.

1.3 Review of force/stress measurement techniques and limitations

Currently available contact force/stress sensing technologies are stress sensitive films. These films operate using three main stress sensing approaches; stress induced: resistance variation [25], capacitance variation [26] and density variation of stains [27]. These sensors allow measurement of stress distributions through discrete sensing elements that are embedded in a regular array over the film area. Figure 1-3 shows two commercially available stress sensitive film systems.

In resistive films [25-27] (Figure 1-3b), the film contains the sensor array and is comprised of three distinct layers arranged in a laminar stack. A first layer contains a pattern of conductors with their principle axes parallel to, and of the same length, as the length dimension of the sensing area. The second layer consists of a resistive material that has variable resistance proportional to the stress-induced compression of the layer. This layer is sized such that it is identical in length and width to the sensing area. The third and final layer contains a pattern of conductors that are oriented perpendicular to those of the first layer, or aligned along the width direction. Each location where the three layers intersect is a sensing location. Stress is measured over the sensing area by measuring the variation in resistance at each sensing location.

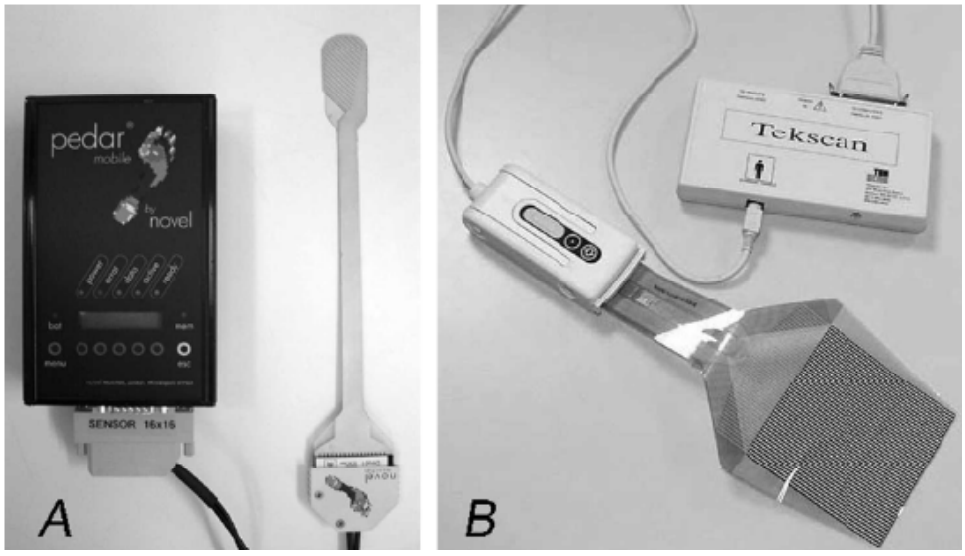

Figure 1-3: a) Capacitive Novel AJP sensor system (Novel GmbH, Munich, Germany). Sensing area is rectangular tip at end of slender support connected to data acquisition cable. b) Resistive Tekscan sensor system (Tekscan®, Boston, MA). Sensing area is square and located at end of the flexible support connected to data acquisition cable. Reproduced with permission from Clinical Orthopaedics and Related Research© [26].

Capacitive films [26] (Figure 1-3a) are constructed similarly; however, in the capacitive laminar stack a dielectric is placed between the perpendicular array of conductors. Stress is measured over the sensing area by measuring the variation in capacitance at each sensing location. The area of each sensing location in both capacitive and resistive films is of the order mm^2 [25].

Stain-recording films operate on a third, non-electrical, principle [27, 28]. These films also utilize laminar stack construction [28]. The first layer consists of substrate material to which the second layer is fixed. The second layer consists of microspheres of varying size evenly distributed over the first layer; these microspheres contain a colorless fluid. The third layer consists of a color-development material. When static stress is applied to the film a range of sizes of microspheres, including the smallest up to a given maximum size, will burst; the maximum size of the burst microspheres is a function of the stress magnitude. When the microspheres burst, the colorless fluid is released onto the

color-development material resulting in a pink stain. In regions subjected to higher stress, a larger range of (i.e. more) microspheres will burst resulting in a dense pink stain. In regions of lower stress the stains will have lower density. Applied stress is inferred by comparing the density of the stains that develop on the film to manufacturer supplied scales. Manufacturers such as Fuji Film (Fuji Photo Film Co. Ltd., Tokyo, Japan) claim spatial resolution on the order of tens of μm^2 for their Prescale [27] line of films (Figure 1-5a). Stain-recording films record a single, non-reversible, pattern of stains and are therefore only applied to measurements of peak forces in static loading [28].

Resistive and capacitive films have been applied *ex vivo* to several dynamic and static contact stress measurements in several anatomies of the human body including the foot [29], ankle [30], knee [31, 32] (Figure 1-4b), and spine [33] (Figure 1-4a). Capacitive films have been applied to contact stress measurements in prosthetic hips *ex vivo* [14]. Stain-recording films have been applied to stress measurements in a similar variety of anatomies [28], including cadaveric hips (Figure 1-5) [34, 35], but for static measurements. Figure 1-5a shows the most popularly applied stress sensitive film, Prescale, which has been pre-cut to allow a conformal fit to the femoral head [34, 35]. Resistive and capacitive films have not been applied to the contoured surfaces of the hip because they cannot be pre-cut to allow a conformal fit to the femoral head.

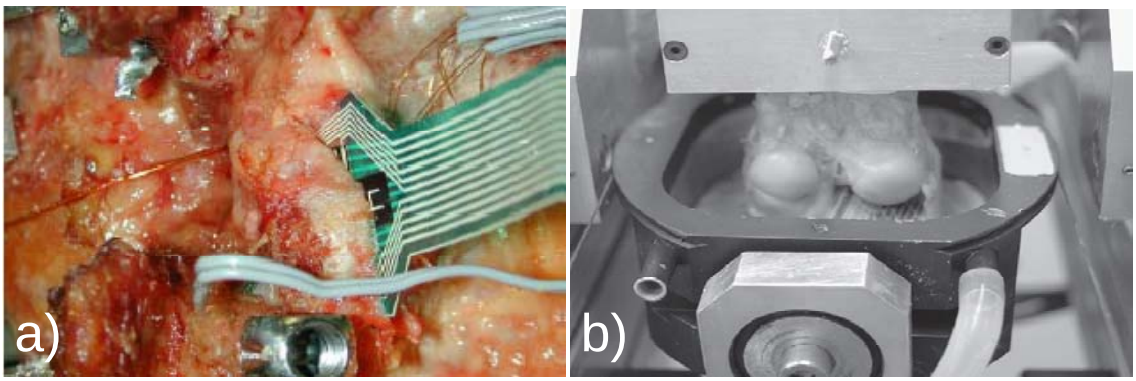

Figure 1-4: a) Tekscan sensor inserted into the capsule of cadaveric spine facet joint. Image reproduced with permission from the Journal of Biomechanics© [33]; b) Tekscan inserted between condyles of cadaveric tibial plateau. Image reproduced with permission from the Journal of Biomechanics© [31].

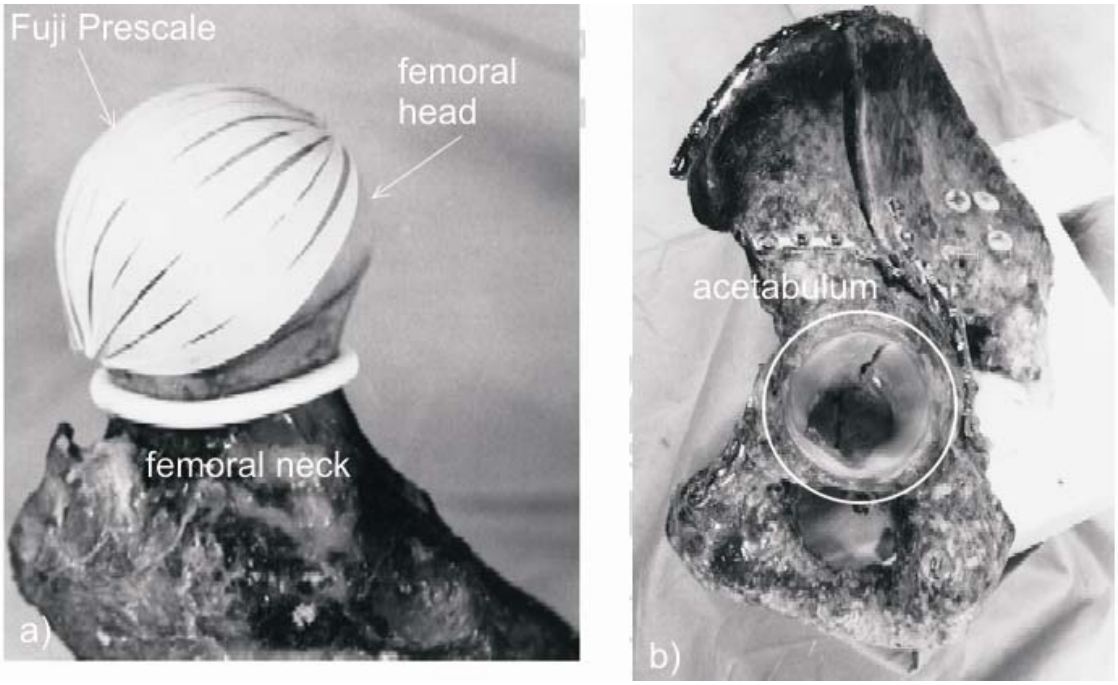

Figure 1-5: a) image showing Fuji Prescale affixed to femoral head. Prescale shown is pre-cut to allow film to conform to femoral head, while avoiding wrinkling of film. Before joint was loaded and contact stresses were measured, the femoral head with Prescale was inserted into the acetabulum (b) that houses the femoral head in the natural joint. Image reproduced with permission from the Journal of Orthopaedic Trauma [35].

There are several limitations with the stress sensitive films discussed above that limit their application in biomechanics and in particular articular joints [17]. Prescale film is the most widely-used transducer for measuring contact stress in joints. It is limited to measuring the highest applied stress at a given location on the contact interface

(Figure 1-6) and it cannot be used to measure how stress changes as joints move in simulated loaded activity. Typically, the continuously changing contact area and stress at cartilage interfaces have been inferred from measurements made at discrete intervals through the joint's range of movement. This is clearly a disadvantage because the rate of change of stress and the position of the center of stress cannot be determined and because key changes in the pattern of contact stress may be missed. A further disadvantage is that static measurements of contact stress may not reflect the contact stress during dynamic activity. Because of the substantial time-dependence of cartilage material properties [19, 36], due to cartilage consolidation, it is reasonable to assume that measurements of contact stress will vary substantially between static and dynamic loading.

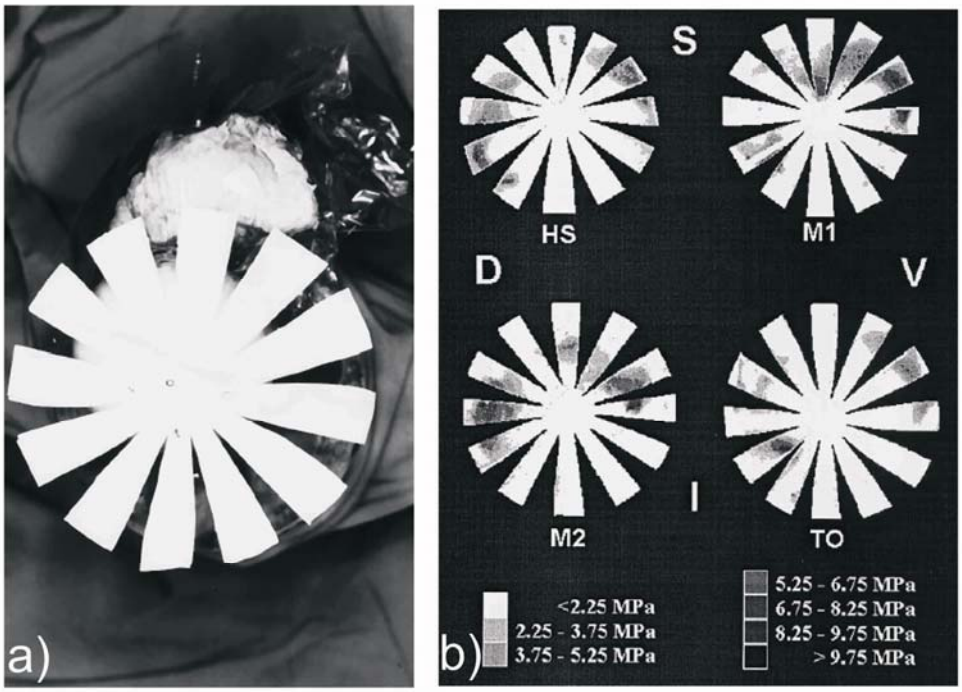

Figure 1-6: a) Pre-cut Prescale film positioned above the cartilage surface of femoral head; b) Peak stress recordings on Prescale film. Stress magnitudes may be inferred from color scale. Reproduced with kind permission from Springer Science+Business Media: Unfallchirurg, Quantitative bestimmung der druckverteilung im huftgelenk wahrend des gangzyklus, 102, 1999, 625-631, Eisenhart-Roth, R.v., Witte, H., Steinlechner, M., Muller-Gerbl, M., Putz, R., Eckstein, F., Figures 3 and 4, ©Springer-Verlag 1999.

A further limitation of Prescale film is that it is difficult to use in joints with substantial curvature such as the hip because of the tendency of the material to crinkle when it is used on a curved surface – an artefact that distorts measurements by up to 28% [37]. A final limitation of Fuji film is that it must be inserted in the joint interface, which necessarily disrupts contact mechanics [37].

The Tekscan sensor that measures force, stress and area continuously with a thin, flexible sensor addresses some of the static measurement-limitations of Prescale film but cannot be used in many joints. The limitations of this system are: a) that it cannot be used in joints with substantial curvature such as the hip because the sensor does not work when excessively bent along curved surfaces, b) the sensor exhibits significant time-dependence (drift) of load measurements, c) the sensor must be attached to the joint with adhesive, which adversely affects its repeatability [32], and d) like Fuji film, the sensor must be inserted in the joint interface, which disrupts contact mechanics [37].

The degree to which Tekscan and Prescale sensors affect the joint mechanics is a function of several factors: film thickness and elastic modulus, film curvature and cartilage elastic modulus [32, 37, 38]. Moreover, experimental evidence shows the accuracy of these sensors is a function of the modulus of the contacting material (*i.e.* cartilage) [37]. As a consequence, these sensors must be pre-calibrated using materials with similar modulus to those found *in situ* or sample materials of identical modulus which, in the case of biological tissues, are rarely available *a priori*.

There are also limitations associated with application of these sensors in the human hip specifically. To apply these sensors, the hip must first be dissected to allow access to the femoral head. Dissection can include large incisions in, or complete removal

of, biomechanically relevant accessory structures such as the joint capsule. These incisions must be sized comparably to the film dimensions to allow insertion. These accessory structures play a crucial role in hip mechanics and preserving synovial fluid layers [2, 19, 39]. Once dissection is complete, access to the femoral head is gained by removing the femoral head from the acetabulum (Figure 1-5). This process is referred to as disarticulation and has been shown to negatively impact natural hip mechanics by disrupting synovial fluid layers, pressurization and lubrication which are all thought to be closely coupled to contact force/stress [2, 19, 39]. Because film based sensors require dissection of biomechanically relevant structures (*i.e.* joint capsules and the labrum), that would be intact *in vivo*, it has been impossible to validate the mechanical rationale underlying preventive or corrective surgeries, that repair these structures, by conducting stress measurements in intact (cadaveric or living hips with all accessory structures in place) hips.

Moreover, as a consequence of disarticulation and loss of synovial fluid layers, it has been impossible to conduct simultaneous measurements of force/stress and synovial fluid pressure to understand the relationships between stress and pressure within intact joints. To date, experimental investigations of hip mechanics have measured either synovial fluid pressure [19] or contact force/stress [18].

1.4 Objectives

The overarching objective of this work is to develop sensors to measure local contact forces/stresses between the conforming cartilage surfaces of intact hip joints using a fibre-optic sensor technology: the *in-fibre Bragg grating* (FBG). The work of this

dissertation is organized into three sub-objectives that are structured to systematically progress toward fulfilling the overarching objective.

The first sub-objective is to perform the first theoretical and experimental characterization of the sensitivity, to contact force, of gratings subjected to conforming contact. This characterization is a crucial step that will quantify the extent to which the compressive modulus of contacting materials affects sensor sensitivity. Quantification of modulus dependant changes in grating sensitivity will allow estimation of modulus dependant measurement errors similar to those previously described for the film-based sensors.

The second sub-objective is to use insights gained from the characterization to develop prototype contact force/stress sensors based on Bragg gratings. A component of this development process will include characterization for sensitivity to transverse force/stress and modulus dependence of sensitivity, among other parameters.

The third sub-objective is to apply FBG sensors to contact force/stress measurements in cadaveric hip specimens. To achieve this sub-objective, minimally invasive methods will be developed to insert the FBG sensors into the hips and make measurements of local contact force/stress.

1.5 Organization of dissertation

The work of this dissertation is presented using the manuscript format that comprises a *body* and a series of *appendices*. In the body of the dissertation, motivation and background material is presented as well as a summary of contributions. The summary of contributions describes and links the detailed presentation of work that comprises a series of manuscripts, each contained in a separate appendix.

With the clinical motivations and limitations of existing force/stress sensors already described in Chapter 1, background material for optics and force sensing principles of FBGs is presented in Chapter 2. Chapter 2 concludes with a short discussion that emphasises the limitations of existing force/stress sensors based on films and FBGs to give context to the summary of sensor development contributions of Chapter 3. In Chapter 3, the progression of sensor development is summarized through a description of three studies. Chapter 4 concludes the dissertation and briefly outlines planned directions for future work.

Chapter 2: In-fibre Bragg gratings (FBGs)

This chapter provides background information on optical fibre, FBGs and force sensing with FBGs to give context to sensor development and application to the hip. To allow the simplest possible introduction to this material, fundamental concepts including Bragg reflection and polarization are introduced first with reference to conventional single-mode optical fibre. Subsequently, these concepts are extended to polarization maintaining highly birefringent optical fibres. Theory and pragmatic considerations and an overview of FBG force sensors is included to give context to the sensor design contributions in Chapter 3.

2.1 Principles of optical fibre and FBGs

In this dissertation, a conventional single-mode optical fibre (hereafter referred to as conventional fibre) comprises the standard telecommunication coaxial fibre geometry shown in Figure 2-1a. The majority of light propagating through the optical fibre is retained within the core (Figure 2-1a) which is nominally 8 μm in diameter and typically comprises Germanium-doped silica glass. Surrounding the core is the clad (Figure 2-1a) which has a nominal outside diameter of 125 μm and typically comprises pure silica. Light propagating in the direction $\underline{k}$ (Figure 2-1a) is retained within the core because the conditions for total internal reflection are satisfied for the coaxial fibre geometry [40].

While the electromagnetic principles fundamental to total internal reflection and mode propagation are beyond the scope of this chapter, a qualitative discussion regarding relevant fibre characteristics is included.

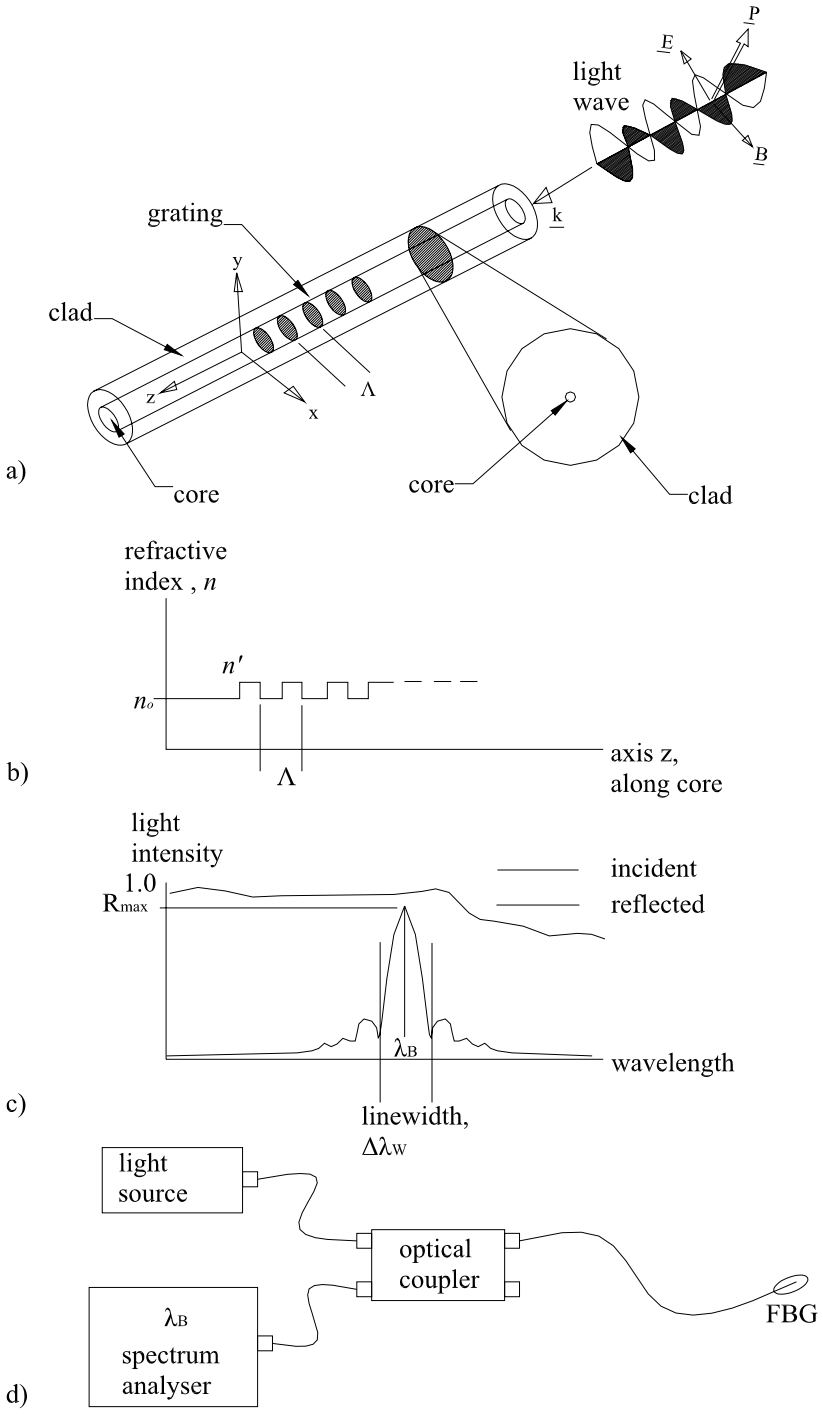

Figure 2-1: a) schematic (not to scale) showing relevant features of conventional single-mode fibre. A plane electromagnetic light wave [40] propagates and is retained within the core of the fibre. Inset cross section of fibre (to scale) shows relative sizes of fibre core and clad. Hatched ellipses along fibre core represent a Bragg grating comprising regions of modified refractive index; b) representative refractive index profile along the length of the Bragg grating. The hatched ellipses shown in a) correspond to the locations along the axis z where the refractive index increases from n_0 to n'; c) representative reflected spectrum of FBG; d) typical equipment configuration used to illuminate FBG and measure Bragg wavelength.

For an optical fibre, total internal reflection requires that the refractive index, *n*, of the core exceed the refractive index of the clad [40-42]. In conventional fibre, Germanium-doping of pure silica increases the refractive index of the core by 0.4% relative to the un-doped clad [43]. This 0.4% difference between the core and clad indices is sufficient to satisfy total internal reflection in single-mode fibre of the given dimensions. The fibre dimensions also partially dictate the number of modes transmitted through an optical fibre.

The term mode refers to solutions of the electromagnetic wave equation for light transmission in the fibre. Specifically, there are several forms of light waves that transmit in optical fibre, each corresponding to a different solution of the electromagnetic wave equation. Each solution is referred to as a light transmission mode and is partially governed by the optical and geometric properties of the fibre [41]. Some fibres are designed to transmit a single mode (Figure 2-1a), sometimes referred to as the lowest bound mode, whereas others transmit multiple modes. Bragg gratings used for sensing are designed to reflect the lowest bound mode and are, therefore, formed within single mode fibres [40].

FBGs are formed in optical fibres by creating a periodic variation in the refractive index of the fibre core [40, 44] (Figure 2-1a and 2-1b). The length of the FBG and the magnitude and period of the variation in the refractive index determine the optical spectrum that is reflected by the FBG [40, 45]. When light spanning a broad range of wavelengths is incident on the Bragg grating (Figure 2-1c), a single-peaked spectrum of wavelengths is reflected. This spectrum is centered at the Bragg wavelength, λ_B, which is given by:

$$\lambda_B = 2\Lambda n_0 \qquad (2\text{-}1)$$

where, as shown in Figure 2-1a and 2-1b, Λ is the spatial-period of the variation in the refractive index and, n_0, is the effective refractive index of the fibre core [40]. In conventional fibre, the effective refractive index is the same for all polarization directions, P, and, therefore, the Bragg wavelength will be the same for any state of polarization. As mentioned above, the shape of the spectrum is determined by the length and refractive index profile of the FBG [40]. More specifically, the maximum reflectivity, R_{max}, is a function of the spatial period; length of the grating, L; and index difference $n' - n_0 = \Delta n$ [40]:

$$R_{max} = \tanh^2\left[\pi\left(\frac{\Delta n}{2n_0}\right)\left(\frac{L}{\Lambda}\right)\right] \qquad (2\text{-}2)$$

and the linewidth, $\Delta\lambda_W$ (width in the wavelength domain of Figure 2-1c), is given by [40]:

$$\Delta\lambda_W = 2\lambda_B\left[\left(\frac{\Lambda}{L}\right)\left(\frac{\Delta n}{2n_0}\right)\right]^{1/2} \qquad (2\text{-}3)$$

The magnitudes of the Bragg wavelength, maximum reflectivity and linewidth are typically specified based on the specifications of the optical equipment used to detect the Bragg wavelength, the light transmission properties of the optical fibre and the requirements of the application in which the FBG is used as a sensor [40]. Figure 2-1d shows a typical equipment configuration where light from a source is directed *via* optical fibre into a bi-directional coupler, which directs light into a fibre containing an FBG. The spectrum reflected by the FBG is directed back into the coupler and into a spectrum analyser that measures the Bragg wavelength of the reflected spectrum. Common

magnitudes for the Bragg wavelength and maximum reflectivity are 1550 nano-meters (nm) and 90% of the peak intensity of incident light, respectively. The linewidth typically varies from as low as 0.2 nm (10 mm FBG length, L) to 1 nm (1mm FBG length) [40]. An FBG formed in a highly birefringent polarization maintaining fibre reflects two spectra, each similar in form to that described above, because of non-uniform index of refraction in the fibre core.

The primary difference distinguishing highly birefringent polarization maintaining fibre from conventional fibre is that highly birefringent fibre has differing refractive indices along two orthogonal directions, the slow and fast axes, in the fibre core (Figure 2-2a). The difference in refractive index, $n_s - n_f$, along the slow and fast axes (Figure 2-2a) is referred to as the *birefringence*, B, and in highly birefringent fibre is of the order 10^{-4} [40]. In general, due to external influences of force and strain or due to fibre construction, conventional fibre can also exhibit birefringence that is typically of the order 10^{-5} or less. Birefringence in conventional fibre is not desirable because it leads to dispersion of optical signals in telecommunications applications and it is not prescribed along known slow or fast axes. Conversely, birefringence in highly birefringent fibre is desirable because it can be used to maintain the polarization direction, P (Figure 2-1a), of telecommunications signals along known slow and fast axes, and also has beneficial implications in the context of sensing [40].

Two examples of highly birefringent polarization maintaining fibre (hereafter referred to as birefringent fibre) are shown in Figure 2-2a. The underlying source of birefringence in these fibres is described fully in the manuscripts that are the subject of Chapter 3. The reader is referred to those manuscripts for detailed discussion that

augment details provided here. The Bow Tie fibre (Figure 2-2a) is one example of birefringent fibre that is based on *stress-induced birefringence* [46] created by stress-applying parts in the fibre clad; whereas the D-shape fibre that has an elliptical core (Figure 2-2a) is one example of fibre that is based on *geometric birefringence* [47]. Both fibres shown in Figure 2-2a have different refractive indices along orthogonal slow and fast axes. Because there exists two distinct refractive indices along the slow and fast axes, the Bragg condition for reflection expressed as Equation 2-1 is re-expressed as two equations, one for each axis:

$$\lambda_s = 2\Lambda n_s$$
$$\lambda_f = 2\Lambda n_f \qquad (2\text{-}4)$$

where the subscripts s and f refer to the slow and fast axis, respectively [40]. A representative plot of the Bragg spectra corresponding to the slow and fast axis is shown in Figure 2-2b.

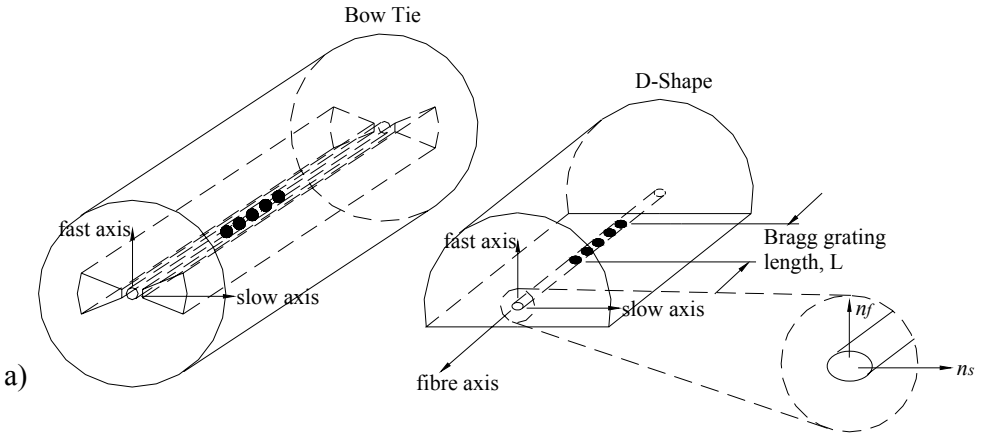

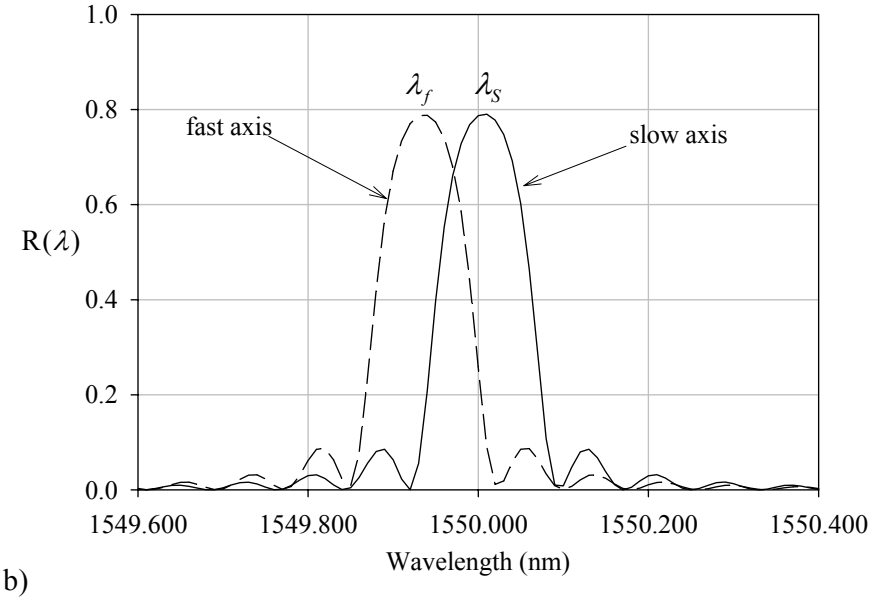

Figure 2-2: a) schematics of Bow Tie birefringent fibre and D-shape birefringent fibre showing refractive indices along slow and fast axes; b) representative Bragg spectra reflected from a Bragg grating inscribed in a birefringent fibre.

The Bragg spectrum corresponding to the slow axis (Figure 2-2b) has polarization vector, P (Figure 2-1a), aligned with the slow axis of the fibres (Figure 2-2a); whereas the spectrum corresponding to the fast axis is aligned with, or polarized along, the fast axis. For Bragg gratings in both conventional and birefringent fibre, the magnitudes of the Bragg wavelengths will change due to applied mechanical parameters (*e.g.* strain, temperature, pressure etc.). The fundamental principle underlying Bragg grating sensors

is detecting Bragg wavelength changes as functions of these mechanical parameters. To understand the Bragg grating force sensors developed in this work, principles governing Bragg wavelength changes due to applied force are presented below.

2.2 Stress-optic and strain-optic principles

Contact forces applied to optical fibres (Figure 2-3a) cause changes in the Bragg wavelength and shapes of the Bragg spectra. These forces affect Bragg wavelength changes by changing both the grating period and index of the fibre core (Equation 1). The force-induced changes in grating period and index can be modeled using either stress-optic or strain-optic formulations [40, 42].

While these formulations can be shown to be mathematically equivalent, the conventions of the stress-optic formulation allow the simplest modeling of changes in overall fibre birefringence, $n_s - n$, between to the two polarization directions (slow and fast axis) caused by changes in contact forces. These changes in overall birefringence can then be used to explain overall changes in the Bragg spectra. On the other hand, the equations of the strain-optic formulation are suited to calculating changes in index along any single polarization direction (either slow or fast) and, therefore, are best suited to calculating Bragg wavelength shifts specific to either the fast or slow axis.

To convey an overall understanding of force induced changes in the Bragg spectrum the stress-optic formulation is presented first. Subsequently, to convey changes in the Bragg spectrum on each polarization, the presentation will transition to strain-optic principles.

For any optical fibre, the birefringence in the fibre core can be expressed as the sum of three contributions [48]:

$$B = n_s - n_f = B_G + B_{IS} + B_E \tag{2-5}$$

where B_G is the geometric contribution that, typically, is found only in optical fibres with asymmetric or elliptical cores (e.g. D-shape fibre in Figure 2-2a); B_{IS} is the internal stress contribution that, typically, is found in optical fibres with internal stress applying parts (e.g. Bow Tie fibre in Figure 2-2a); and B_E is the external contribution to fibre birefringence that is typically caused by externally applied contact forces. According to the stress-optic formulation, the external contribution to birefringence can be calculated as:

$$B_E = C(\sigma_x - \sigma_y) \tag{2-6}$$

where C is a stress-optic coefficient for the given optical fibre and material comprising the fibre and σ_x and σ_y are contact force-induced principal stresses that are referred to the fibre co-ordinate system shown in Figure 2-3a. The *spectral separation* between the slow and fast axis Bragg wavelengths, $\lambda_s - \lambda_f$ is given by:

$$\lambda_s - \lambda_f = 2\Lambda(n_s - n_f) = 2\Lambda B \tag{2-7}$$

where, as stated previously, the refractive index difference between the slow and fast axis is referred to as the birefringence, B.

In a conventional fibre (Figure 2-1a) birefringence is, nominally, zero when there is no contact force because all the entries in the right-hand side of Equation 5 are zero. The shape of the Bragg spectrum resembles that shown in Figure 2-3b (at left) where there is no spectral separation. When forces are applied, the external contribution, B_E, increases because the difference in principal stresses increases. The corresponding change in the Bragg spectrum is shown in Figure 2-3b (at left) and is characterized by a

decrease in peak reflectivity and an increase in linewidth [40, 42]. Unlike an FBG in a birefringent fibre that reflects two distinct spectra, the spectrum shown has a single peak because Bragg gratings in conventional fibre are typically illuminated with nominally un-polarized light. However, if contact forces on the conventional fibre are continually increased birefringence will continually increase (Equation 2-6) and the single peak spectrum will ultimately split into two spectra, each single peaked.

In a birefringent fibre, B_G and B_{IS} are large enough to create a detectable spectral separation when the fibre is not subjected to contact force (Figure 2-2b). When contact forces are applied to a birefringent fibre (Figure 2-3a at right), the contribution B_E increases and the spectral separation between the slow and fast axis also increases (Figure 2-3b at right) [40, 42].

To determine the direction of the Bragg wavelength shift on either the slow or fast axis, or for light polarized along the y and x axes (Figure 2-3), strain-optic equations are used. The changes in the Bragg wavelength of light polarized along the slow axis and fast axis are given by:

$$\begin{aligned} \Delta\lambda_s &= \lambda_s \left[\varepsilon_z - \frac{n_s^2}{2}\left(p_{xz}\varepsilon_z + p_{xx}\varepsilon_x + p_{xy}\varepsilon_y \right) \right] \\ \Delta\lambda_f &= \lambda_f \left[\varepsilon_z - \frac{n_f^2}{2}\left(p_{yz}\varepsilon_z + p_{yx}\varepsilon_x + p_{yy}\varepsilon_y \right) \right] \end{aligned} \tag{2-8}$$

where $\Delta\lambda$ denotes a change in Bragg wavelength; ε denotes mechanical strain with the subscripts referencing the fibre coordinate system shown in Figure 2-3a; and $p_{xz} = p_{xy} = p_{yx} = p_{yz} = 0.252$ and $p_{xx} = p_{yy} = 0.113$ are strain-optic constants for a typical Germanium-doped fibre core [40]. Note that the subscripts on the photoelastic constants are referred to the fibre coordinate system. For a conventional fibre with un-polarized

light, it is reasonable to assume that half the light is aligned along each of the y and x axes to calculate the spectral separation resulting in increased linewidth. The mechanical strains are in Equations 8 are due to the applied contact forces [40, 42].

The preceding overview of theory provides background for the in-depth theory and modeling described in the manuscripts presented in this dissertation. The reader is referred to these manuscripts for further details and context-specific application of this theory.

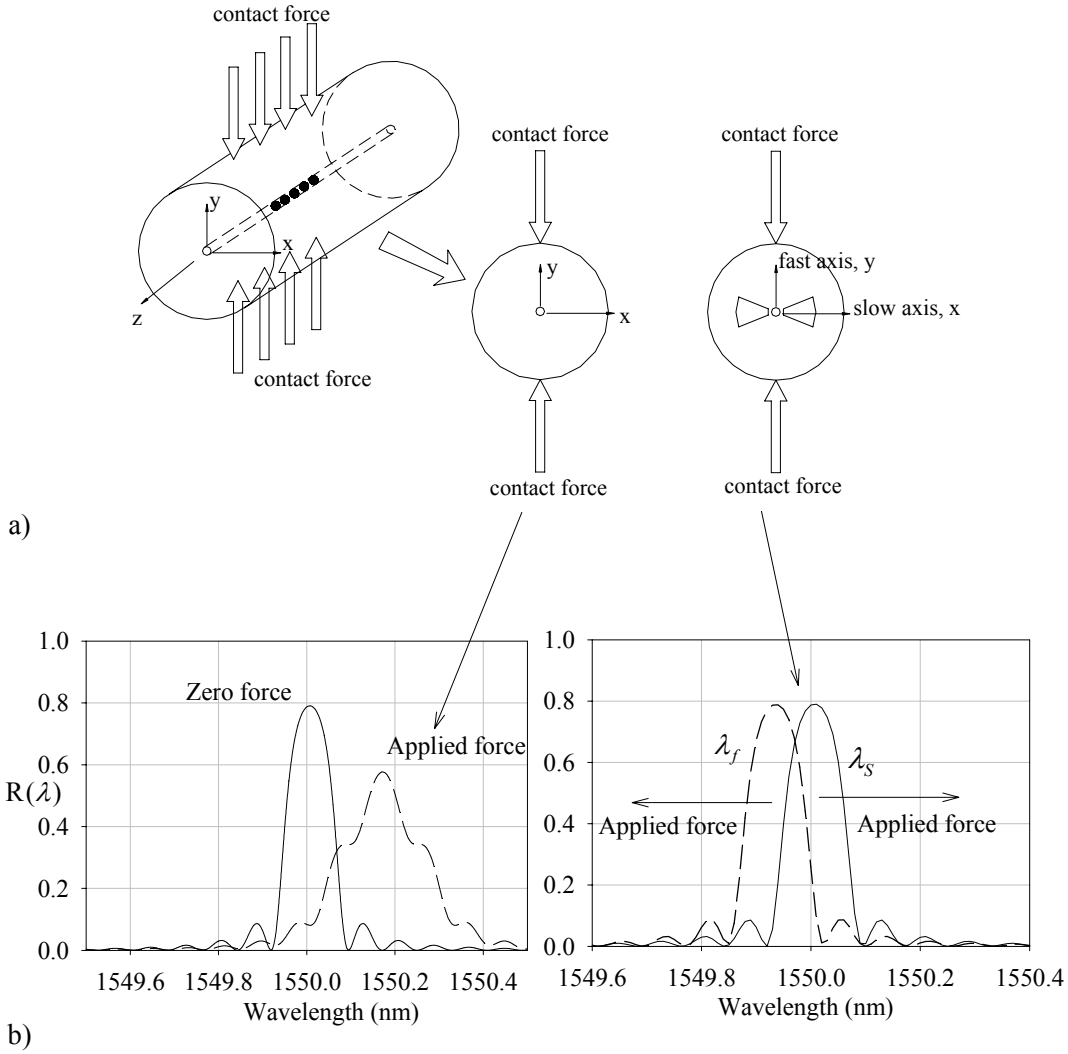

Figure 2-3: a) schematic showing contact forces applied to the clad of optical fibre. Both conventional (left) and Bow Tie birefringent (right) fibre cross sections are shown; b) representative plots showing typical changes in the Bragg spectrum for (left) conventional fibre and (right) birefringent fibre that result from applied contact forces.

2.3 Pragmatic considerations: force sensing in the hip with FBGs

In the context of application to force measurements in the hip, FBGs possess key characteristics that will allow these sensors to be implanted into the hip joint while avoiding some of the limitations of film sensors:

1. *Extremely small size*: optical fibres are nominally 125 μm in diameter and various methods exist to reduce fibre diameter to as small as 20 μm [49-51], thereby allowing insertion into joint spaces using techniques that may not otherwise be possible with the film based sensors (*e.g.* arthroscopically) and that do not require

removal of biomechanically relevant accessory structures. In the context of *in vivo* application, these sensors could be implanted through extremely small incisions thereby allowing measurements *in vivo*.

2. *Biocompatibility*: optical fibre is constructed using silica glass that is chemically inert. Low-power, non-electrical, optical signals are retained within fibres and do not interact with tissues that surround the sensor. Non-electrical signals also eliminate risk of electric shock. Unlike the film-based sensors, these sensors are also compatible with contemporary medical imaging techniques such as computer-aided tomography and magnetic resonance imaging.
3. *Mechanical compliance and robustness*: due to their size optical fibres have extremely low flexural rigidity and therefore offer negligible resistance to applied loads. This is attractive for biomechanics applications because fibre based sensors minimally impact the natural mechanics of the host structures. Optical fibres also have extremely high tensile and compressive strength and can sustain strains exceeding 5000 microstrain before fracture.

While these characteristics make FBGs attractive, the current state of the art in force sensing with FBGs does not address several pragmatic considerations that prevent successful application of FBGs to the hip. These considerations are related to (1) the nature of cartilage-cartilage contact in hips and (2) the geometry and characteristics of the of the joint and synovial fluid layers and difficulties with sensor insertion and alignment in the interior of the joint

As described in Chapter 3, in articular joints such as the hip, contact between cartilage surfaces and contact between fibre sensors and cartilage will be *conforming*. In conforming contact, the contact lengths between the fibre cross section (e.g. Figure 2-3a at right) and cartilage are comparable to the fibre diameter and dependent on the elastic modulus of the cartilage surfaces. These modulus-dependent contact lengths affect force sensitivity of FBGs and have not been modeled or experimentally tested. To the contrary,

FBGs have only been applied to measurement of contact forces in *Hertzian contact*. Udd *et al.* (1996) [52] applied Bragg gratings in 3M, Fujikura and Corning birefringent fibres to simultaneously measure temperature and force. Wierzba and Kosmowski (2003) [53] applied Side-Hole birefringent fibre to force measurements. Chehura *et al.* (2004) [54] investigated the force sensitivity of D-shape, Elliptical core, TruePhase, Panda, Bow Tie and Elliptical clad birefringent fibres as a function of fibre orientation. More recently, Abe *et al.* (2006) [49] measured force using chemically-etched Bow Tie and Elliptical clad birefringent fibres to understand the influence that reduction in fibre diameter has on fibre birefringence and force sensitivity.

In all of the studies outlined above, the fibre orientation relative to contact forces was controlled because the force sensitivity of FBGs in birefringent fibres is also dependent on fibre orientation. When FBG sensors are implanted into joints, it is impossible to orient and control orientation with respect to contacting cartilage surfaces. It is impossible to orient, and control the orientation after insertion, of fibre sensors because (1) the joint capsule prevents optical access to the interior joint thereby preventing visual determination of fibre-to-cartilage orientation and (2) wet cartilage surfaces and synovial fluid layers prevent fibre fixation.

In Chapter 3, details of sensor development are used to articulate the contributions of this thesis with reference to the ultimate application of force measurements in intact hips.

Chapter 3: Contributions

This dissertation presents the results of three studies organized under Section 3.1, 3.2 and 3.3. These studies are described in detail in the manuscripts included as Appendix A through C. In this chapter, an overview of the motivations, methods, key results, and logical progression between studies is presented. The logical progression is structured to describe systematic progress toward the overarching objective: development of sensors to measure local contact forces/stresses between the conforming cartilage surfaces of intact hip joints FBGs.

3.1 Characterization of FBGs for conforming contacts and demonstration of modulus-independent contact-force measurements

The primary objective of this study is to perform the first characterization and validation of FBGs for contact-force sensitivity in conforming contact. In the context of sensor development for the hip, this characterization and validation is a critical first step that will quantify the extent to which variations in the compressive modulus of cartilage will affect FBG sensor sensitivity. Understanding the effect of compressive modulus on sensitivity allows quantification of errors in FBG contact force measurements as a function of cartilage modulus. This is a critical step to establish bounds on error of FBG measurements over the range of cartilage modulii that are found in hips. Moreover, insights from this characterization are used to inform future sensor development described in subsequent contributions.

Prior to this work, all previous FBG-based force sensors have been characterized for Hertzian contact in which the optical fibre comprising the sensor is contacted above and below by materials of similar elastic modulus to the glass fibre [52, 54-58]. Recently, researchers led by Ngoi (2004) attempted to model contact between FBGs and conforming materials but applied an inappropriate contact model based *only* on Hertzian contact [59]. More recently, following publication of the modeling described in this contribution, FBG sensors using conforming contact have been reported for non-biomedical applications [60]. However, as described below, the modeling detailed for this contribution is the first to apply an appropriate contact model with stress-optic formulations to characterize FBGs for application in conforming contact.

The characterization and validation for contact-force sensitivity comprised both theoretical and experimental work. A theoretical, semi-analytic, contact model originally developed for pin-in-hole contact between elastically dissimilar materials [61] was adapted to model contact between the circular cross section of an optical fibre and a flat surface. The results of the contact model were applied in a plane elasticity model [62] to predict the contact force-induced principal stresses within the fibre that indicate contact force-induced birefringence. The modeling was completed for a range of contact scenarios defined primarily by a range on cartilage modulus.

Experimental work focused on validating results from modeling. Experimental apparatii were constructed to apply contact forces to birefringent optical fibres through materials of varying compressive modulus. To simulate cartilage layers, Viton® (dipolymer of hexafluoropropylene and vinylidine fluoride) with a Young's Modulus of 5

MPa was used. Data from the reflected spectrum of FBGs for varying contact forces were recorded and ultimately compared to the model predictions.

A key result from this work was that contact length and, therefore, contact induced principal stresses within the optical fibre, for any given contact force, were approximately constant for the range of modulus values typical of articular cartilage. Because principal stresses do not vary with cartilage modulus, variations in birefringence are a function of contact-force alone, not cartilage modulus. This result and practical observations of the conforming contact were ultimately used to develop methods for *modulus-independent* contact force measurements.

Modulus-independent measurements of contact force can be achieved with sensor designs with contact lengths, between the sensor and contact surface, that do not vary with modulus of the contacting material. Like previous work with FBGs in birefringent fibre, this study also indicates strong orientation-dependence of sensitivity. This study led to the sensor design presented in the subsequent study that has both modulus-independent sensitivity and orientation-independent sensitivity.

The reader is referred to Appendix A for the details of the study described in Section 3.1

3.2 Development of a contact-force sensor with modulus- and orientation-independent sensitivity and application to cadaveric human hips

The objectives of this study are to: (1) develop an FBG-based contact force sensor that has both modulus- and orientation-independent force sensitivity; (2) to develop methods to insert the sensor into cadaveric human hips without removing the joint capsule; and (3) to perform the first simultaneous measurements of contact force and hydrostatic pressure

in intact cadaveric hips. In the context of sensor development for the hip, this work addresses two of the limitations of film-sensors described in Chapter 1: modulus-dependence of force measurements *and* the necessity to dissect the joint capsule to implant sensors. The limitations of films have prevented measurements in intact hips including simultaneous measurement of contact force and synovial fluid pressures which are thought to be closely linked to each other and also to indicate natural hip mechanics. This work also addresses one limitation of FBG sensors in birefringent fibre: orientation-dependence of sensitivity.

Prior this work, FBG-based contact force sensors had limitations that prevented their application to articular joints. As described above, FBG sensors in birefringent fibre posses orientation-dependence of sensitivity [52, 54, 57, 58, 63, 64]. Orientation-dependence of sensitivity is a key limitation because the internal structure of the joint does not allow sensor alignment or fixation to preserve alignment. FBG contact force sensors in conventional fibre had been developed [59] but were too large to fit between the cartilage surfaces of the hip which are separated by a synovial fluid layer of approximately 0.4 mm or smaller [2]. FBGs in conventional fibre had been adapted into prosthetic devices, like tibial spacers, and applied to the knee [65], but, again, these sensors are too large to implant in the hip and require removal of joint capsules.

This study comprised design, theoretical and experimental work. Based on insights from the study of Section 3.1, a prototype FBG contact force sensor was designed using conventional fibre to have: orientation- and modulus-independent sensitivity; a major outside diameter of only 0.24 mm; and the highest force sensitivity relative to all other FBG-based force sensors. Theoretical work included finite-element

(FE) modeling of contact and sensor performance for conforming contact between non-linear materials with mechanical properties specified to simulate cartilage. Experimental work comprised a series of sensor calibrations with materials of different modulus to validate FE-predictions of modulus-independence. Calibration was also performed for several sensor orientations to confirm orientation-independence.

Experimental work in cadaveric hips comprised development of new sensor insertion techniques to implant both FBG-based pressure sensors [66] and force sensors into the joint space while leaving the capsule intact. After sensor insertion, the FBG sensors were used to conduct the first pilot study with simultaneous measurements of synovial fluid pressures and contact forces.

Force measurements were not repeated using Prescale film and, therefore, there was no comparison of FBG measurements to Prescale measurements. The rationale to forgo this comparison was that Prescale insertion requires joint dissection and disarticulation which disrupts synovial fluid layers that were, presumably, left intact during FBG measurements. Disruption of synovial layers permanently alters the mechanics of the joint including contact forces and synovial fluid pressure and, therefore, prevents direct comparison between FBG and Prescale force measurements.

Force/pressure measurements were not repeated using the current standard film sensor because Prescale insertion requires dissection and disarticulation, which disrupts synovial fluid layers that were intact for FBG measurements. and, therefore, the mechanics of the joint. required large incisions in the joint capsule and disarticulation of the joint. As described in Chapter 1, disarticulation leads to loss of synovial fluid layers that are relevant to the mechanics of the joint. Therefore, because synovial fluid layers

While the theoretical FE results and the experimental calibration results combined to validate the performance of this sensor, the key result of this work was that FBG sensors and the insertion techniques can be applied to give repeatable measurements of contact force and hydrostatic pressure within intact hips. Further development and validation of this sensor and its insertion techniques are described in Chapter 4 (future work).

One limitation of this sensor is that it has co-sensitivity to applied axial strains and temperature changes, which are parameters that can confound measurements within the hip. These limitations are addressed with the sensor presented in the subsequent study that has negligible co-sensitivity to strain and temperature.

The reader is referred to Appendix B where the study described in Section 3.2 is detailed fully.

3.3 Development of a contact force sensor without co-sensitivity to axial strain and temperature

The objective of this study is to develop a FBG contact force sensor based on birefringent fibre that has no co-sensitivity to axial strain and temperature, two parameters that can confound measurements with the sensor described in Section 3.2, and, therefore, can confound force measurements in hips. The sensor described in this study also addresses a key limitation with previous FBG sensors in birefringent fibres, namely orientation dependence of sensitivity. In the context of application to the hip, the sensor addresses the limitations that can confound force measurements with FBG sensors in both conventional fibre and birefringent fibre.

Like the sensor described in Section 3.1 and 3.2, the sensor development in this contribution comprised design, theoretical and experimental work. A prototype FBG

contact force sensor was designed around birefringent D-shape fibre to have: no co-sensitivity to axial strain and temperature; a self-aligning super-structure that repeatably orients the sensor with respect to applied contact forces; force sensitivity comparable to the most sensitive FBG-based force sensors in birefringent fibre; and diameter of 0.165 mm in the direction of force application. The self-aligning super-structure insures that the force sensitivity is constant because it repeatably orients the sensor, and D-shape fibre, to a prescribed orientation relative to the applied force.

Theoretical work included development of an analytic plane elasticity and strain-optic model capable of predicting the performance of the sensor in terms of contact force-induced Bragg wavelength shifts. Experimental work comprised a series of sensor calibrations to validate the model predictions and the capacity of the self-aligning super-structure to correctly orient the sensor and, thereby, result in repeatable sensitivity to contact force. The efficacy of the alignment feature was established by calibrating the sensor in two stages. In stage 1, the sensor without the alignment feature was oriented, using external orientation control, and calibrated. This stage established the maximum achievable force sensitivity. In stage 2, the sensor with the alignment feature was calibrated, while sensor orientation was determined solely by the alignment feature. This stage established that the alignment feature repeatably oriented the sensor by demonstrating that sensitivity was near-constant (without external control) and comparable to the maximum achievable. Calibration was also performed to verify that the sensor had no co-sensitivity to axial strain or temperature changes.

The key results of this study are that: (1) the self-aligning superstructure correctly orients the sensor with respect to the contact force and; therefore, (2) the sensor has

constant force sensitivity; and (3) the sensor has no appreciable co-sensitivity to axial strain or temperature. Possible directions for further development and validation of this sensor and insertion techniques in hips is described in Chapter 4 (future work).

The reader is referred to Appendix C where the study described in Section 3.3 is detailed fully.

Chapter 4: Conclusions and future work

4.1 Conclusions and summary of contributions

The overarching objective of this dissertation was to develop sensors to measure local contact force between the conforming cartilage surfaces of intact hip joints using FBGs. A secondary objective was to develop minimally invasive methods to insert the FBG sensors into intact hips and make measurements of local contact force.

The work towards completion of these objectives spanned optics, mechanics, design, and biomechanics disciplines and included both theoretical and experimental work. Sensors were modeled through elasticity theory and stress- or strain-optic theory to predict sensor performance. Experimental work included calibration to validate modeled predictions in terms of sensitivity, orientation-dependence, modulus-dependence, and co-sensitivity to axial strain and temperature. Experimental methods to apply the sensors in cadaveric hips were also developed to allow *ex vivo* measurements of contact force.

The contributions in this dissertation are summarized below and organized with respect to the three studies, or sections, of Chapter 3:

1. Characterization of FBGs for conforming contacts and demonstration of modulus-independent contact-force measurements:

The first contribution of this study is characterization and experimental data for FBGs subjected to conforming contacts. The results of this characterization and practical observations of the conforming contact ultimately led to the second contribution of this study: methods for modulus-independent contact force measurements. While the

motivation of this work is force measurements in the hip, the characterization and experimental data will also have broad applicability to some of the other emerging applications of FBGs in conforming contact which are articulated in the introduction and discussion of Appendix A (or reference [67]).

2. Development of a contact-force sensor with modulus- and orientation-independent sensitivity and application to cadaveric human hips:

The first three contributions of this study are expressed in terms of the characteristics of the sensor. The sensor: (1) has the highest sensitivity reported for FBG force sensors; (2) addresses limitations with previous FBG force sensors including orientation-dependence of sensitivity; (3) addresses limitations of films including modulus-dependent sensitivity and the necessity to dissect joints. The fourth contribution is methods to insert the sensor to make the first simultaneous measurements of contact force and hydrostatic pressure in hips.

3. Development of a contact force sensor without co-sensitivity to axial strain and temperature:

The three contributions of this study are expressed in terms of the characteristics of the sensor. A sensor based on birefringent D-shape fibre is presented that: (1) addresses limitations with FBG force sensors in conventional fibre including co-sensitivity to axial strain and temperature; (2) addresses a limitation with FBG force sensors in birefringent fibre: the necessity to control fibre orientation; and (3) has force sensitivity comparable to the highest reported sensitivity of FBG force sensors based on birefringent fibre.

In the broader context of understanding hip biomechanics, the sensors presented in this dissertation could be used to answer controversial questions that cannot be

answered through measurements with stress sensitive films. For example, because the FBG sensors can be implanted in intact joints, the FBG sensors could be used to investigate the currently unknown relationships between synovial fluid pressures and contact stress magnitudes, which are thought to be relevant to the etiology of joint degeneration and the condition of accessory structures such as the labrum. The pilot results for pressure/force presented in this dissertation have established the feasibility of inserting FBG sensors into an intact joint and performing repeatable measurements that will be necessary to establish these relationships. Moreover, the characteristics of the FBG sensors are also desirable for applications in other articular joints such as facets of the spine, the shoulder and the knee.

4.2 Future work

The primary limitation of the insertion technique presented in this dissertation is that there is potential for sensors to translate within the joint space during motion because they are not fixed to either the femoral head or acetabulum. Sensor translation is an obstacle to continuous force measurements, at prescribed locations within the joint, because the location of sensors relative to the femoral head/acetabulum is unknown.

Continuous, FBG-based, force measurements during joint motion would constitute a contribution to hip biomechanics literature by offering mechanical understanding of hip pathologies that are linked to osteoarthritis. For example, femoroacetabular impingement has been linked to osteoarthritis genesis [68] and is partially characterized by reduced range of motion due to abutment between the femoral neck and acetabulum. Understanding the mechanical changes in the hip due to these hip

pathologies through force measurements at prescribed locations in the hip would inform the mechanical rationale behind corrective surgeries.

Below, one insertion approach is described that could allow insertion of multiple FBG force sensors at prescribed locations *and* that could serve to fix the sensors relative to the acetabulum. Access to the acetabular cartilage could be gained through the bone of acetabulum through an access bore, as shown in Figure 4-1. Mechanical drilling of the bone along several axes could create access bores leading to prescribed locations in the acetabular cartilage that are believed to be mechanically relevant. Following formation of the bores, force sensors could be introduced into the cartilage by first piercing the cartilage with a hypodermic needle with an inside diameter large enough to accommodate the force sensor. The needle could then be advanced into the cartilage to a prescribed depth, and then withdrawn, leaving the force sensor implanted into the cartilage (Figure 4-1). This insertion approach was developed for the force sensor based on conventional fibre. To use this approach with the super-structured D-shape fibre sensor, alterations to the alignment feature of the superstructure may be required to allow the sensor to be embedded within a hypodermic and aligned with respect to cartilage surfaces.

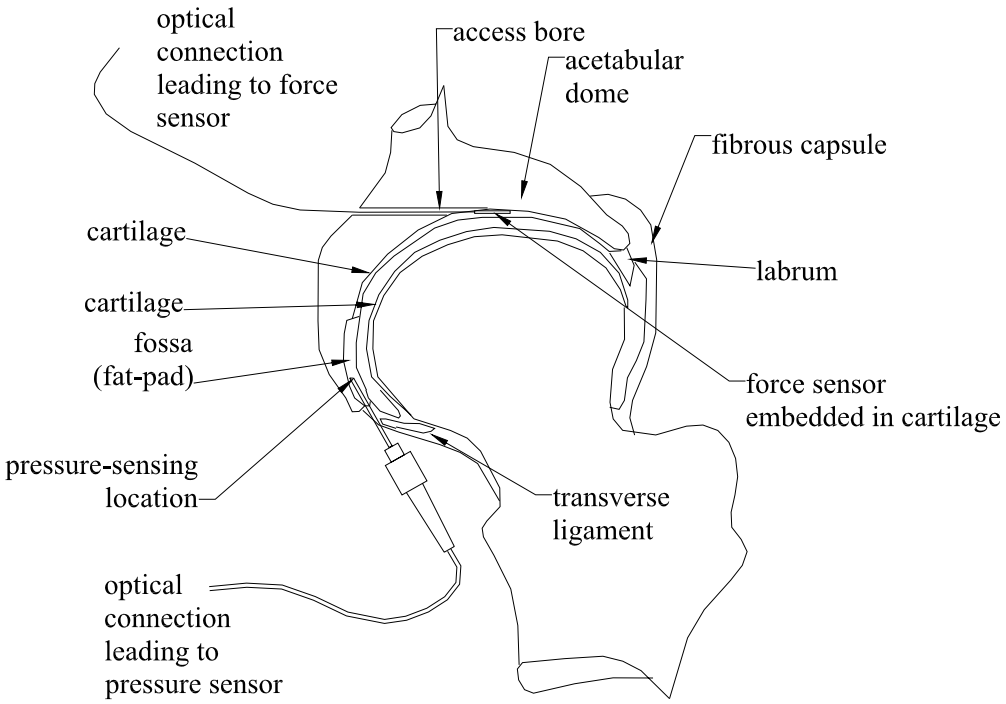

Figure 4-1: schematic hip cross-section showing force sensor inserted through access bore in acetabulum and embedded into the cartilage of the acetabulum.

Development of insertion approaches is ongoing with researchers and clinicians from the Department of Orthopaedic Engineering Research (UBC) and the Centre for Hip Health and Mobility (UBC, Vancouver Coastal Health Research Institute) who have interest in the mechanical changes associated with hip pathology.

Bibliography

[1] Sariali, E., Veysi, V., and Stewart, T., 2008, "Mini-Symposium: Essential biomechanics of hip replacement (i): Biomechanics of the human hip-consequences for total hip replacement " Current Orthopaedics, 22, pp. 371-375.

[2] Ferguson, S., Bryant, J., Ganz, R., and Ito, K., 2000, "The acetabular labrum seal: a poroelastic finite element model," Clinical Biomechanics, 15(6), pp. 463-468.

[3] Barker, M. K., and Seedhom, B. B., 2001, "The relationship of the compressive modulus of articular cartilage: does cartilage optimize its modulus so as to minimize the strains arising in it due to the prevalent loading regime?," Rheumatology, 40, pp. 274-284.

[4] Kim, J.-E., Zuoping, L., Ito, Y., Huber, C. D., Shih, A. M., Eberhardt, A. W., Yang, K. H., King, A. I., and Soni, B. K., 2009, "Finite element model development of a child pelvis with optimization-based material identification," Journal of Biomechanics, 42, pp. 2191-2195.

[5] Brown, C., Nguyen, T., Moody, H., Crawford, R., and Oloyede, A., 2009, "Assessment of common hyperelastic constitutive equations for describing normal and osteoarthritic articular cartilage," Proceedings of IMechE Part H: Journal of Engineering in Medicine, 223, pp. 643-652.

[6] Moody, H., 2006, "Benchmarking of the biomechanical characteristics of normal and degraded articular cartilage to facilitate mathematical modeling," Queensland University of Technology, Brisbane.

[7] Zuoping, L., Alonso, J. E., Kim, J.-E., Davidson, J. S., Etheridge, B. S., and Eberhardt, A. W., 2006, "Three-dimensional finite element models of the human pubic symphysis with viscohyperelatic soft tissues," Annals of Biomedical Engineering, 34(9), pp. 1452-1462.

[8] Lever, C. J., and O'Hara, J. N., 2008, "Adult Hip: Young adult hip disease: hip morphology and impingement," Current Orthopaedics, 22, pp. 414-421.

[9] Komistek, R. D., Kane, T. R., Mahfouz, M., Ochoa, J. A., and Dennis, D. A., 2005, "Knee mechanics: a review of past and present techniques to determine in vivo loads," Journal of Biomechanics, 38, pp. 215-228.

[10] D'Lima, D. D., Steklov, N., Fregly, B. J., Banks, S. A., and Jr., C. W. C., 2008, "In vivo contact stresses during activities of daily living after knee arthroplasty," Journal of Orthopaedic Research, doi: 10.1002/jor.20670.

[11] Varadarajan, K. M., Moynihan, A. L., D'Lima, D., Colwell, C. W., and Li, G., 2008, "In vivo contact kinematics and contact forces of the knee after total knee arthroplasty during dynamics weight-bearing activities," Journal of Biomechanics, 41, pp. 2159-2168.

[12] Hartofilakidis, G., Georgiades, G., and Babis, G. C., 2009, "A comparison of the outcome of cemented all-polyethylene and cementless metal-backed acetabular sockets in primary total hip arthroplasty," The Journal of Arthroplasty, 24(2), pp. 217-225.

[13] Jonkers, I., Sauwen, N., Lenaerts, G., Mulier, M., Perre, G. V. d., and Jaecques, S., 2008, "Relation between subject-specific hip joint loading, stress distribution in the proximal femur and bone mineral density changes after total hip replacement," Journal of Biomechanics, 41, pp. 3405-3413.

[14] Muller, O., Parak, W. J., Wiedemann, M. G., and Martini, F., 2004, "Three-dimensional measurements of the pressure distribution in artificial joints with a capacitive sensor array," Journal of Biomechanics, 37, pp. 1623-1625.

[15] Ong, K. L., Day, J. S., Kurtz, S. M., Field, R. E., and Manley, M. T., 2008, "Role of surgical position on interface stress and initial bone remodeling stimulus around hip resurfacing arthroplasty," The Journal of Arthroplasty, doi:10.1016/j.arth.2008.08.005.

[16] Canada, H., 2010, "Seniors and Aging - Osteoarthritis," http://www.hc-sc.gc.ca/hl-vs/iyh-vsv/diseases-maladies/seniors-aines-ost-art-eng.php.

[17] Wilson, D. R., McWalter, E. J., and Johnston, J. D., 2008, "The measurement of joint mechanics and their role in osteoarthritis genesis and progression," Rheumatic Disease Clinics of North America, 34, pp. 605-622.

[18] Anderson, A. E., Ellis, B. J., Maas, S. A., Peters, C. L., and Weiss, J. A., 2008, "Validation of finite element predictions of cartilage contact pressure in the human hip joint," Journal of Biomechanical Engineering, 130, p. 10pp.

[19] Ferguson, S. J., Bryant, J. T., Ganz, R., and Ito, K., 2003, "An in vitro investigation of the acetabular labral seal in hip joint mechanics," Journal of Biomechanics, 36, pp. 171-178.

[20] Herzog, W., Clark, A., and Wu, J., 2003, "Resultant and local loading in models of joint disease," Arthritis and Rheumatology, 49, pp. 239-247.

[21] Ficat, P., 1978, "The syndrome of lateral hyperpressure of the patella," Acta Orthopaedica Belgium, 44, pp. 65-76.

[22] Huberti, H. H., and Hayes, W. C., 1988, "Contact pressure in chondromalacia patellae and the effects of capsular reconstructive procedures," Journal of Orthopaedic Research, 6, pp. 499-508.

[23] Konrath, G. A., Hamel, A. J., Sharkey, N. A., Bay, B., and Olson, S. A., 1998a, "Biomechanical evaluation of a low anterior wall fracture: correlation with the CT subchondral arc.," Journal of Orthopaedic Trauma, 12, pp. 152-158.

[24] Konrath, G. A., Hamel, A. J., Sharkey, N. A., Bay, B., and Olson, S. A., 1998b, "Biomechanical consequences of anterior column fracture of the acetabulum," Journal of Orthopaedic Trauma, 12(547-552).

[25] Drewniak, E. I., Crisco, J. J., Spenciner, D. B., and Fleming, B. C., 2007, "Accuracy of circular contact area measurements with thin-film pressure sensors," Journal of Biomechanics, 40, pp. 2569-2572.

[26] Martinelli, L., Hurschler, C., and Rosenbaum, D., 2006, "Comparison of capacitive versus resistive joint contact stress sensors," Clinical Orthopaedics and Related Research, 447, pp. 214-220.

[27] Bachus, K. N., DeMarco, A. L., Judd, K. T., Horwitz, D. S., and Brodke, D. S., 2006, "Measuring contact area, force, and pressure for bioengineering applications: Using Fuji Film and TekScan systems," Medical Engineering and Physics, 28, pp. 483-488.

[28] Orr, J. F., and Shelton, J. C., 1997, Optical measurement methods in biomechanics, Chapman and Hall.

[29] Zou, D., Mueller, M. J., and Lott, D. J., 2007, "Effect of peak pressure and pressure gradient on subsurface shear stresses in the neuropathic foot," Journal of Biomechanics, 40.

[30] McKinley, T. O., Rudert, J. M., Koos, D. C., Pederson, D. R., Baer, T. E., Tochigi, Y., and Brown, T. D., 2006, "Contact stress transients during functional loading of ankle stepoff incongruities," Journal of Biomechanics, 39, pp. 617-626.

[31] Cottrell, J. M., Scholten, P., Wanich, T., Warren, R. F., Wright, T. M., and Maher, S. A., 2008, "A new technique to measure the dynamic contact pressures on the tibial plateau," Journal of Biomechanics, 41, pp. 2324-2329.

[32] Wilson, D. R., Apreleva, M. V., Eichler, M. J., and Harrold, F. R., 2003, "Accuracy and repeatability of a pressure measurement system in the patellofemoral joint," Journal of Biomechanics, 36, pp. 1909-1915.

[33] Wilson, D. C., Niosi, C. A., Zhu, Q. A., Oxland, T. R., and Wilson, D. R., 2006, "Accuracy and repeatability of a new method for measuring facet loads in the lumbar spine," Journal of Biomechanics, 39, pp. 348-353.

[34] Eisenhart-Rothe, R. v., Witte, H., Steinlechner, M., Muller-Gerbl, M., Putz, R., and Eckstein, F., 1999, "Quantitative bestimmung der druckverteilung im huftgelenk wahrend des gangzyklus," Unfallchirurg, 102, pp. 625-631.

[35] Levine, R. G., Renard, R., Behrens, F. F., and III, P. T., 2002, "Biomechanical consequences of secondary congruence after both-column acetabular fracture," Journal of Orthopaedic Trauma, 16(2), pp. 87-91.

[36] Greaves, L. L., Gilbart, M. K., Yung, A., Kozlowski, P., and Wilson, D. R., 2009, "Deformation and recovery of cartilage in the intact hip under physiological loads using 7T MRI," Journal of Biomechanics, 42, pp. 349-354.

[37] Wu, J. Z., Herzog, W., and Epstein, M., 1998, "Effects of inserting a pressensor film into articular joints on the actual contact mechanics," Journal of Biomechanical Engineering, 120(5), pp. 655-659.

[38] Brimacombe, J., Wilson, D., Hodgson, A., Ho, K., and Anglin, C., 2009, "Effect of calibration method on Tekscan sensor accuracy " ASME Journal of Biomechanical Engineering, 131(3).

[39] Ferguson, S., Bryant, J., Ganz, R., and Ito, K., 2000, "The influence of the acetabular labrum on hip joint cartilage consolidation: a poroelastic finite element model," Journal of Biomechanics, 33(8), pp. 953-960.

[40] Measures, R. M., 2001, Structural Health Monitoring with Fiber Optic Technology, Academic Press.

[41] Marcuse, D., 1982, Light Transmission Optics, Van Nostrand Reinhold Company Inc., New York, N.Y.

[42] Udd, E., 1991, Fibre Optic Sensors, An Introduction for Engineers and Scientists, Wiley InterScience.

[43] 2001, "Corning SMF-28 optical fibre: Product Information," Corning Incorporated, Midland MI, www.corning.com/opticalfibre.

[44] Hill, K. O., Fujii, Y., Johnson, D. C., and Kawasaki, B. S., 1978, "Photosensitivity in optical fiber waveguides: Application to reflection filter fabrication," Applied Physics Letters, 32(10), pp. 647-649.

[45] Huang, S., LeBlanc, M., Ohn, M. M., and Measures, R. M., 1995, "Bragg intragrating structural sensing," Applied Optics, 34(22), pp. 5003-5009.

[46] Barlow, A. J., and Payne, D., 1983, "The stress-optic effect in optical fibers," IEEE Journal of Quantum Electronics, QE-19(5), pp. 834-839.

[47] Urbanczyk, W., Martynkien, T., and Bock, W. J., 2001, "Dispersion effects in elliptical-core highly birefringent fibers," Applied Optics, 40(12), pp. 1911-1920.

[48] Noda, J., Okamoto, K., and Sasaki, Y., 1986, "Polarization maintaining fibers and their applications," Journal of Lightwave TEchnology, 4(8), pp. 1071-1089.

[49] Abe, I., Frazao, O., Schiller, M. W., Noqueira, R. N., Kalinowski, H. J., and Pinto, J. L., 2006, "Bragg gratings in normal and reduced diameter high birefringence fibre optics," Measurement Science and Technology, 17, pp. 1477-1484.

[50] Alemohammad, H., Toyserkani, E., and Pinkerton, A. J., 2008, "Femtosecond laser micromachining of fibre Bragg gratings for simultaneous measurement of temperature and concentration of liquids," Journal of Physics D: Applied Physics, 41(185101 (9pp)).

[51] Smith, K. H., Selfridge, R. H., Schultz, S. M., Markoz, D. J., and Ipson, B. L., 2004, "Analysis of replacing an optical fiber core with polymer," Optics Express, 12(3), pp. 354-360.

[52] Udd, E., Nelson, D., and Lawrence, C., 1996, "Three Axis Strain and Temperature Fiber Optic Grating Sensor," Proceedings of SPIE, 2718, pp. 104-109.

[53] Wierzba, P., and Kosmowski, B. B., 2003, "Application of polarisation-maintaining side-hole fibres to direct force measurement," Opto-Electronics Review, 11(4), pp. 305-312.

[54] Chehura, E., Ye, C.-C., Staines, S. E., James, S. W., and Tatam, R. P., 2004, "Characterization of the response of fibre Bragg gratings fabricated in stress and

geometrically induced high birefringence fibres to temperature and transverse load," Smart Materials and Structures, 13, pp. 888-895.

[55] Croucher, J. A., Gomez-Rojas, L., Kanellopoulos, S., and Handerek, V. A., 1998, "Approach to highly sensitive pressure measurements using side hole fibre," Electronics Letters, 34(2), pp. 208-209.

[56] Lawrence, C. M., Nelson, D. V., and Udd, E., 1996, "Multi-Parameter Sensing with Fiber Bragg Gratings," Proceedings of SPIE, 2872, pp. 24-31.

[57] Nelson, D., Makino, A., Lawrence, C., Seim, J., Schulz, W., and Udd, E., 1998, "Determination of the K-Matrix for Multi-parameter Fiber Grating Sensor in AD072 Fibercore Fiber," Proceedings of SPIE, 3489, pp. 79-85.

[58] Udd, E., Lawrence, C., and Nelson, D., 1997, "Development of a Three Axis Strain and Temperature Fiber Optic Grating Sensor," Proceedings of SPIE, 3042, pp. 229-236.

[59] Ngoi, B. K. A., Paul, J., Zhao, L. P., and Fang, Z. P., 2004, "Enhanced lateral pressure tuning of fiber Bragg gratings by polymer packaging," Optics Communications, 242, pp. 425-430.

[60] Shao, L.-Y., Jiang, Q., and Albert, J., 2010, "Fiber optic pressure sensing with conforming elastomers," Applied Optics, 49(35), pp. 6784-6788.

[61] Ciavarella, M., and Decuzzi, P., 2001, "The state of stress induced by plane frictionless cylindrical contact. II. The general case (elastic dissimilarity)," International Journal of Solids and Structures, 38, pp. 4525-4533.

[62] Hondros, G., 1959, "The evaluation of Poisson's ratio and the modulus of materials of a low tensile resistance by the Brazilian (indirect tensile) test with particular reference to concrete," Australian Journal of Applied Science, 10, pp. 243-268.

[63] Carrara, S. L. A., Kim, B. Y., and Shaw, H. J., 1986, "Elasto-optic alignment of birefringent axes in polarization-holding fiber," Optics Letters, 11(7), pp. 470-472.

[64] Dennison, C. R., and Wild, P. M., 2010, "Sensitivity of Bragg gratings in birefringent optical fibre to transverse compression between conforming materials," Applied Optics, 49(12), pp. 2250-2261.

[65] Mohanty, L., Tjin, S. C., Lie, D. T. T., Panganiban, S. E. C., and Chow, P. K. H., 2007, "Fiber grating sensor for pressure mapping during total knee arthroplasty," Sensors and Actuators A, 135, pp. 323-328.

[66] Dennison, C. R., Wild, P. M., Dvorak, M. F., Wilson, D. R., and Cripton, P. A., 2008, "Validation of a novel minimally invasive intervertebral disc pressure sensor utilizing in-fiber Bragg gratings in a porcine model: an ex vivo study," Spine, 33(17), pp. E589-E594.

[67] Dennison, C. R., and Wild, P. M., 2010, "Sensitivity of Bragg gratings in birefringent optical fiber to tranvserse compression between conforming materials," Applied Optics, 49(12), pp. 2250-2261.

[68] Ganz, R., Parvizi, J., Beck, M., Leunig, M., Notzli, H., and Siebenrock, K., 2003, "Femoroacetabular impingement: a cause for osteoarthirtis of the hip," Clinical Orthopaedics, pp. 112-120.

Appendix A: Sensitivity of Bragg gratings in birefringent optical fibre to transverse compression between conforming materials

(2010, Applied Optics, volume 49, issue 12)

Sensitivity of Bragg gratings in birefringent optical fibre to transverse compression between conforming materials

Christopher R. Dennison[*] and Peter M. Wild

Department of Mechanical Engineering, University of Victoria,

P.O. Box 3055, Victoria, British Columbia, Canada, V8W 3P6

[*]*Corresponding author: dennison@uvic.ca*

OCIS codes: 060.2370, 260.1440, 120.4880, 060.3735

Abstract

A theoretical and experimental investigation of the transverse load sensitivity of Bragg gratings in birefringent fibres to *conforming* contact is presented. A plane elasticity model is used to predict the contact dimensions between a conforming material and optical fibre and the principal stresses, indicating birefringence, created as a result of this contact. The transverse load sensitivity of commercially available birefringent fibre is experimentally measured for two cases of conforming contact. Theoretical and experimental results show that birefringent optical fibre can be used to make modulus-independent measurements of contact load. Therefore, Bragg gratings could be applied to conforming contact load measurements while avoiding some of the complications associated with existing contact sensors; specifically, the necessity to pre-calibrate using materials with identical mechanical properties to those found *in situ*.

1. Introduction

In-fibre Bragg gratings (FBGs) inscribed in birefringent fibre exhibit sensitivity to many parameters including transverse strain, or load [1]. The physical mechanism causing sensitivity to transverse load is stress-induced birefringence [2]. Transverse loads induce stresses, the principal directions of which are uniform in the region of the fibre core. However, the magnitudes of the principal stresses are a function of the magnitude of the transverse load [1]. Therefore, when the applied load varies, a predictable change in the principal stress magnitudes and, therefore, birefringence is induced. These load-induced changes in birefringence cause predictable changes in the spectrum reflected by the Bragg grating, including shifts in the Bragg spectra corresponding to the fast and slow axes of the fibre.

Birefringent fibres possess higher sensitivity to transverse loads than non-birefringent fibres because they are typically constructed with stress concentrating features that increase load-induced changes in birefringence [3]. These features are generally referred to as stress-applying parts. Each commercially available birefringent fibre possesses unique stress-applying parts. Therefore, the transverse load sensitivity of each type of birefringent fibre is unique. Transverse load sensitivity is also a function of the orientation of the stress-applying parts relative to the direction of load [1].

A number of researchers have studied the relationship between transverse load and birefringence for several types of birefringent fibres. Udd *et al.* (1996) [4] applied Bragg gratings in 3M, Fujikura and Corning birefringent fibres to simultaneously measure temperature and load-induced axial and transverse strain. Wierzba and Kosmowski (2003) [5] applied Side-Hole birefringent fibre to direct force measurements.

Chehura *et al.* (2004) [1] investigated the transverse load sensitivity of D-clad, Elliptical core, TruePhase, Panda, Bow Tie and Elliptical clad birefringent fibres. More recently, Abe *et al.* (2006) [6] measured transverse load using chemically-etched Bow Tie and Elliptical clad birefringent fibres to understand the influence that reduction in fibre diameter has on fibre birefringence and load sensitivity.

All of these studies deal with Hertzian contact [7] between the birefringent fibre and a material (*e.g.* glass [1]) with Young's modulus and Poisson ratio comparable to that of the fibre. In Hertzian contact, contacting materials experience extremely small deformations in the contact zone, resulting in contact regions that are small compared to the overall dimensions of the contacting bodies [7]. In Hertzian contact, the load-induced birefringence is a linear function of the applied transverse load [1, 2].

There are many applications in which contact is *conforming* rather than Hertzian. In conforming contact the modulii of the contacting materials are orders of magnitude lower than that of the optical fibre.

For example, investigators have studied the ergonomics of wheel chair seats [8] by mapping pressure distributions during sitting. In sporting applications, grip forces during golf-swings have been studied by measuring grip pressures [9]. In industrial applications, contact pressures associated with metal-gasket contact have also been mapped to understand degradation in gasket performance [10]. There are also several medical and biomechanics applications where conforming contact is measured. For example, pressure mapping of soft tissues has been correlated to the pathology of prostatectomy specimens in an effort to detect cancer [11]. In biomechanics applications, contact-load measurements are desired in anatomies exhibiting conforming contact

between tissues. One example is load (or contact pressure) measurements between cartilage surfaces in articular joints such as the knee, hip and shoulder. The Young's modulus of cartilage varies but has been measured and found to range from approximately 0.5 MPa [12] to 20 MPa [13], which is extremely low when compared to that of silica glass comprising optical fibre (*e.g.* approximately 70 GPa).

For the applications discussed above, existing sensing technologies are pressure sensitive films. However, experimental evidence shows the accuracy of these sensors is a function of the modulus of the contacting material [14]. As a consequence, these sensors must be pre-calibrated using materials with similar modulus to those found *in situ* or sample materials of identical modulus which, in the case of biological tissues, are rarely available *a priori*. To our knowledge, there have been no investigations of transverse load-induced variations in optical fibre birefringence as a result of non-Hertzian conforming contact.

The objective of this work was to study the sensitivity of birefringent optical fibre to transverse compression between materials in conforming contact. This study was comprised of three stages. First, a theoretical model [15, 16] was applied to calculate the dimensions of the contact zone between the surface of the fibre and the conforming material. These calculations were performed using typical material properties for optical fibre and a range of Young's modulus values bracketing those found in cartilage. Second, the Young's modulus dependent variations in the stresses, within the region of the optical fibre core and for a given contact load, were calculated using a plane elasticity model [17]. These stress calculations were used to estimate the extent to which Young's modulus variation affects induced birefringence in the fibre core. Finally, the insights

gained from stages 1 and 2 were experimentally verified by subjecting a birefringent fibre containing an FBG to conforming compression.

2. Materials and Methods

A. Principles of Bragg gratings and birefringence

FBGs are formed in optical fibres by creating a periodic variation in the refractive index of the fibre core [3, 18]. The length of the FBG and the magnitude and period of the variation in the refractive index determine the optical spectrum that is reflected by the FBG [3, 19]. When light spanning a broad range of wavelengths travels along the fibre core and encounters a Bragg grating, a single-peaked spectrum of wavelengths is reflected. This spectrum is centered at the Bragg wavelength, λ_B, which is given by:

$$\lambda_B = 2\Lambda n_0 \tag{A-1}$$

where Λ is the spatial-period of the variation in the refractive index and, n_0, is the effective refractive index of the fibre core [3].

When non-birefringent optical fibre is subjected to stress, the refractive indices of the fibre core along the directions of principal stress change according to the stress-optic law [2, 20]. The difference between the refractive indices is the birefringence B, given by:

$$B = n_x - n_y = (n_{xo} - n_{yo}) + C(\sigma_x - \sigma_y) \tag{A-2}$$

where the difference between the refractive indices (n_x and n_y), given by the first term, represents the geometric contribution to birefringence due to a non-circular core [20]. The second term represents the stress-induced contribution, where C is the stress-optic

coefficient and σ_x and σ_y are the principal stresses. For a birefringent fibre, the first term is the intrinsic birefringence and the second term is the load-induced birefringence. A Bragg grating inscribed in a birefringent fibre reflects two single-peaked spectra at two Bragg wavelengths corresponding to the fast, f, and slow, s, axes of the fibre [21]:

$$\begin{aligned} \lambda_f &= 2n_f\Lambda \\ \lambda_s &= 2n_s\Lambda \end{aligned} \tag{A-3}$$

where the fast axis is the axis with the smaller refractive index and, therefore, Bragg wavelength.

Birefringent fibre maintains the state of polarization. For example, linearly birefringent fibre is used to maintain the polarization of linearly polarized light and circularly birefringent fibre is used to maintain the polarization of circularly polarized light [22]. However, in the case of low birefringence fibres, loading or bending can alter the state of polarization through changes in birefringence that are comparable in magnitude to the fibre's intrinsic birefringence. In contrast, high birefringence fibres are capable of maintaining their state of polarization in the presence of loading or bending.

For typical, non-birefringent, optical fibre with a circular core the load-induced birefringence, for Hertzian contact, is given by Equation A-4 [1]:

$$B = 2k_o n_o^3 (p_{11} - p_{12})(1+\nu)\frac{F}{\pi r E} \tag{A-4}$$

where k_o is the free-space propagation constant, p_{11} and p_{12} are photo-elastic constants [3], ν is the Poisson ratio of the silica core, E is the Young's modulus of the core, r is the fibre radius and F is the applied transverse load per unit of length of fibre. Other relationships exist for the total birefringence (*i.e.* intrinsic plus load-induced) of

birefringent fibres [23], and these relationships show that total birefringence is a function of the transverse load.

B. Contact and stress models

Previous investigations of transverse load sensitivity have considered only Hertzian contact where principal stresses and birefringence are a function of the transverse load alone (Equation A-4). An underlying assumption of Hertzian contact theory is that contact lengths between bodies remain small, relative to the sizes of the contacting bodies. In conforming contact, contact lengths are large and, therefore, Hertzian theory does not apply.

In this work, a conforming contact model [15, 16] is used to determine contact length, as a function of transverse load and modulus, between an optical fibre and a low modulus polymer. A plane elasticity model [17] is then used to determine the principal stresses in the fibre core, from which birefringence is determined. This model was previously developed to estimate plane stresses in a diametrically compressed circular cross section where the compressive forces are distributed over finite lengths of the circumference. Unlike relations developed for diametric point loading of a disc [7] , the equations developed by Hondros (1959) [17] model stress induced by diametrically opposed distributed loads over finite regions of the disc circumference, as shown in Figure A-1.

Because the principal directions of stress coincide with the axes Ox and Oy , we are concerned only with the stresses along these axes, in particular the stresses in the region of the fibre core. The stresses along Oy (Figure A-1, element A) are given by:

$$\sigma_x = \frac{2P}{\pi}\left[\frac{(1-r^2/R^2)\sin 2\theta}{(1-2r^2/R^2\cos 2\theta + r^4/R^4)} - \left(\tan^{-1}\frac{1+r^2/R^2}{1-r^2/R^2}\right)\tan\theta\right]$$
$$\sigma_y = -\frac{2P}{\pi}\left[\frac{(1-r^2/R^2)\sin 2\theta}{(1-2r^2/R^2\cos 2\theta + r^4/R^4)} + \left(\tan^{-1}\frac{1+r^2/R^2}{1-r^2/R^2}\right)\tan\theta\right] \quad \text{(A-5)}$$

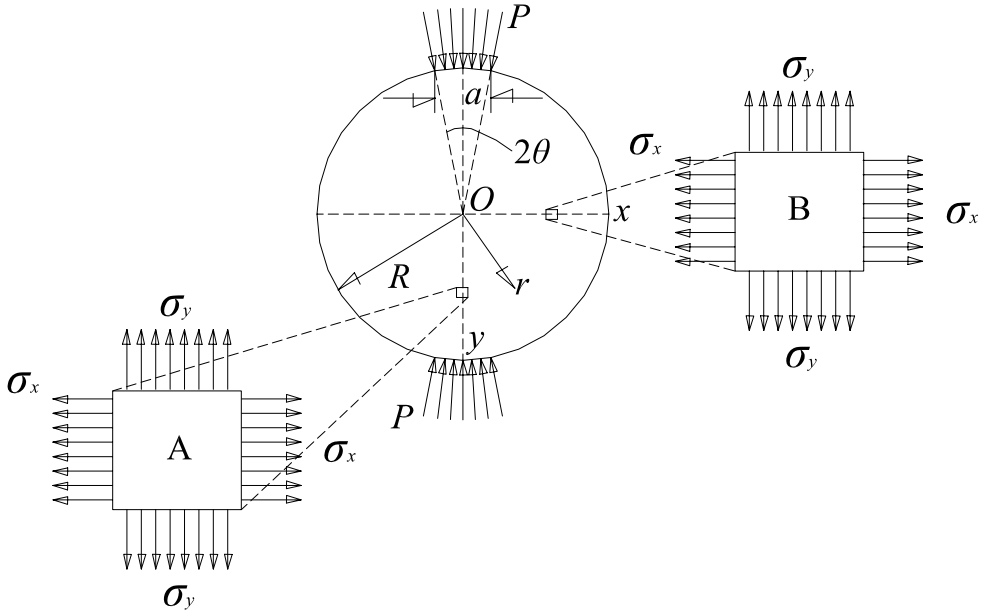

Figure A-1: schematic showing uniform pressure P, distributed over the contact length a, or contact angle 2θ, of the optical fibre (disc of radius R). Coordinate axes also shown. Arbitrary radius r, originates from disc centre O. Square elements labeled A and B show principal stress directions along Oy and Ox axes, respectively.

where the parameters in the equations are defined in Figure 1. The stresses along Ox (Figure A-1, element B) are given by:

$$\sigma_y = -\frac{2P}{\pi}\left[\frac{(1-r^2/R^2)\sin 2\theta}{(1+2r^2/R^2\cos 2\theta + r^4/R^4)} + \left(\tan^{-1}\frac{1-r^2/R^2}{1+r^2/R^2}\right)\tan\theta\right]$$
$$\sigma_x = \frac{2P}{\pi}\left[\frac{(1-r^2/R^2)\sin 2\theta}{(1+2r^2/R^2\cos 2\theta + r^4/R^4)} - \left(\tan^{-1}\frac{1-r^2/R^2}{1+r^2/R^2}\right)\tan\theta\right] \quad \text{(A-6)}$$

For small contact lengths of approximately $a \le R/5$, Equations A-5 and A-6 simplify to Equations A-7 [17]. Considering the stresses in the core of the fibre, where r is small

relative to R, σ_x and σ_y along Ox and Oy are equal, as would be expected for equilibrium.

$$
\begin{aligned}
&Oy: \\
&\sigma_x = \frac{2P\theta}{\pi} \\
&\sigma_y = \frac{2P\theta}{\pi}\left[1 - \frac{4}{(1-r^2/R^2)^2}\right] \\
&Ox: \\
&\sigma_y = \frac{2P\theta}{\pi}\left[1 - \frac{4}{(1+r^2/R^2)^2}\right] \\
&\sigma_x = \frac{2P\theta}{\pi}\left[1 - \frac{4r^2/R^2}{(1+r^2/R^2)^2}\right]
\end{aligned}
\qquad \text{(A-7)}
$$

Equations A-5 through A-7 assume a uniform applied pressure. However, when contact occurs between the optical fibre and a conforming material, non-uniform contact pressure occurs over the contact length, a [7]. When the contact length is small, approximating the contact pressure as uniform results in stresses that are approximately equal to those determined with non-uniform contact pressure [24]. Therefore, application of Equations A-5 through A-7 requires that the contact length, a, be small (*i.e.* $a \le R/5$). Moreover, when $a \le R/5$ one can substitute $P\theta = F/(2Rl)$, where l denotes the fibre length supporting the load, into Equations A-7 to obtain the stress as a function of the load F [17]. To apply Equations A-5 through A-7, the contact angle 2θ must be determined.

Figure A-2 is a schematic showing contact between an optical fibre (Body 1) and a conforming material (Body 2). The relationship between the contact angle, θ, and contact load per unit length, F, is given by Equation A-8 [16].

$$\frac{E_1^* \Delta R}{F} = \frac{(\alpha - 1)(\log[b^2 + 1] + 2b^4) + 2}{\pi(1+\alpha)(b^2+1)b^2} - \frac{4\beta}{\pi(1+\alpha)} \tag{A-8}$$

E_1^* is the plane strain Young's modulus of Body 1, $\Delta R = R_2 - R_1$, and α and β are material constants that are functions of the Young's modulii and Poisson ratios of Body 1 and Body 2. The parameter b gives the magnitude of the contact angle through Equation A-9.

$$b = \tan(\theta / 2) \tag{A-9}$$

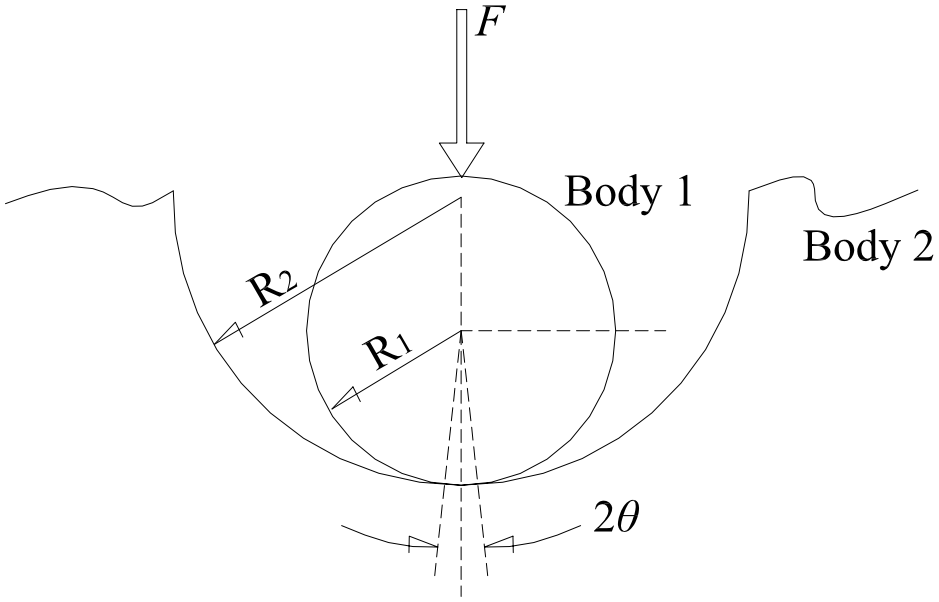

Figure A-2: schematic showing geometry of contact between optical fibre (Body 1) and conforming material (Body 2). Applied force F, is expressed per unit of fibre length supporting the contact load and can be located anywhere along the line of action shown. Contact angle θ, is the half angle of contact as measured from the vertical axis of symmetry. Body 1 (Body 2) has Young's modulus E_1 (E_2) and Poisson ratio ν_1 (ν_2).

To calculate α and β, the ratios η and ς are needed:

$$\begin{aligned} \eta &= E_1^* / E_2^* \\ \varsigma &= (1 - \nu_1^*) - \eta(1 - \nu_2^*) \end{aligned} \tag{A-10}$$

where ν_1^* and ν_2^* are the plane strain Poisson ratios. Equations A-11 can then be used to calculate α and β as:

$$\alpha = \frac{1-\eta}{1+\eta}$$
$$\beta = \frac{1}{2}\frac{\varsigma}{1+\eta} \tag{A-11}$$

Finally, by substituting suitable material properties into Equations A-10 and A-11, and specifying F and ΔR, the contact angle can be found by solving Equation A-8 for b.

C. Model implementation

Contact angles between the optical fibre (Body 1) and conforming material (Body 2) were determined using Equation A-8 for a range of Young's modulii of Body 2 and transverse loads. Contact lengths were calculated from the contact angles and fibre radius as, $a = 2R\theta$. The principal stresses were then determined using Equations A-5 through A-7.

The modulus of Body 2 was varied from 0.5 MPa to 20 MPa, a range of values that brackets those measured for cartilage. The Poisson ratio of Body 2 was also chosen to match that of cartilage and was specified at 0.106 [25]. Transverse loads of 0 N/mm to 3.0 N/mm were modeled. An estimate of the pressure, applied to the fibre, can be obtained by dividing these loads by the fibre diameter (*i.e.* 125 μm). Based on this estimation, applied pressures ranged over 0 MPa to 24 MPa; this range of values brackets those measured in articular joints in biomechanics applications. ΔR was specified at 0.999 m, to approximate an optical fibre contacting a flat plane. The Young's modulus, Poisson ratio and radius of the optical fibre were specified at 70 GPa, 0.17 and 62.5 μm, respectively [3].

D. Experiments

Highly birefringent Bow Tie (HB-1500, Fibercore Ltd., UK) optical fibres with 10 mm Bragg gratings (each peak with approximately 0.2 nm FWHM, Blue Road Research, Gresham OR.) were used in the transverse load experiments. All fibres were chemically stripped of their protective polyimide coatings, thereby preventing errors attributed to non-uniform polyimide thickness. Figure A-3a shows relevant features of the transverse loading apparatus.

The Bow Tie fibre (hereafter test fibre) and a support fibre of identical size (Corning SMF-28, Midland MI), were subjected to transverse load between two metrology gauge blocks (Class 0, 24.1 mm by 24.1 mm, steel, Mitutoyo Can., Toronto ON). The bottom gauge block supported the optical fibres and the top block applied transverse load to each fibre. Both gauge blocks were constrained by guide blocks (Figure A-3a) allowing motion only in the direction of load application. This prevented relative motions that can cause fibre twisting and non-repeatable results [1]. Transverse loads were applied by compressing a calibrated spring (Figure A-3a) with a manual screw-follower (not shown). These loads were then transmitted through a pre-calibrated load cell (445 N capacity, ± 0.1 %FS non-repeatability, Futek Inc., Irvine CA) connected to a data-acquisition system implemented in LabView™ (version 8, National Instruments Inc., Austin TX). The load was transmitted through the top gauge block, through the optical fibres and finally to the bottom gauge block. Load-dependent wavelength shifts were measured using an optical spectrum analyzer (ANDO AQ6331, Tokyo JP) as described below.

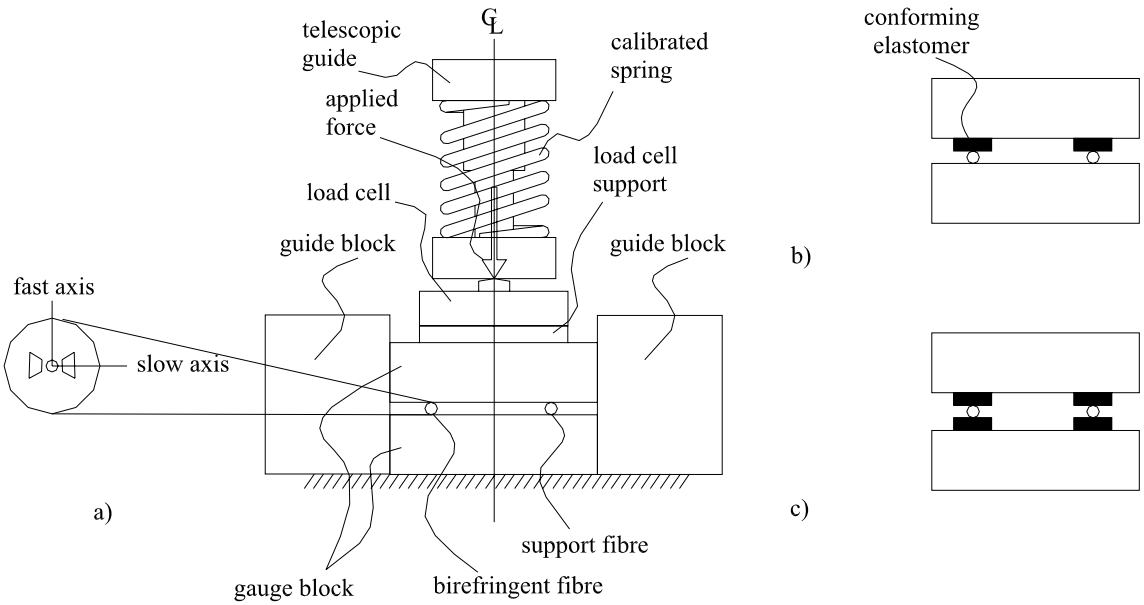

Figure A-3: schematic showing relevant features of transverse loading apparatus. Transverse loads are created by manually compressing a calibrated spring. Load is then transmitted through the load cell, to the top gauge block, through the fibres and then to the bottom block. Both gauge blocks are constrained to allow only vertical motion by guide blocks. Optical fibres are shown between steel gauge blocks. Bow Tie fibre fast and slow axes also shown.

Bragg wavelength variations were demodulated by directing light from a broad C-band light source (AFC-BBS1550, Milpitas, CA) into a linear polarizer (PR 2000, JDS Uniphase, Milpitas CA) and then into one of the input channels of a 3 dB optical coupler (Blue Road Research). The light was then directed *via* the coupler to the FBG in the test fibre, and the reflected spectrum was directed back through the optical coupler and into the optical spectrum analyzer. The polarization of the light was adjusted to illuminate either the fast of the slow axis of the fibre using the tuning facilities of the linear polarizer.

Three loading protocols were used in this work. The objective of the first protocol was to validate the performance of the transverse load apparatus and fibre-loading methods by comparing results obtained in this work to results published by previous

investigators for Bow Tie fibre. Static transverse loads were applied, ranging from 0 N to 40 N at 5 N increments (0 N/mm to 1.7 N/mm at 0.2 N/mm increments when normalized to fibre length), to the test fibre by compressing it between the two gauge blocks as shown in Figure A-3a. The contact in this protocol was Hertzian. The test fibre was subjected to load first along its fast and then along its slow axis (axis orientations of fibre noted in Figure A-3a) and this process was repeated three times while the Bragg wavelengths of both the fast and slow axis were recorded. The sensitivity to load, for both the fast and slow axes, was calculated using linear-regression as the slope in the recorded data, in terms of wavelength shift versus applied transverse load. Sensitivity was also calculated based on the spectral separation of the fast and slow axes (*i.e.* the difference between the slow and fast axis wavelengths) because this is a direct indicator of the induced birefringence in the fibre. The calculated sensitivities were then compared to those published in previous literature that considered Bow Tie fibre.

The objective of the second protocol was to test the predictions of sensitivity dependence on modulus obtained from the contact and stress calculations. The fibre was subjected to contact between a conforming elastomer with Young's modulus in the range of values of cartilage (Viton®, durometer 75A, Young's modulus 5.0 MPa [26]) and a calibrated gauge block, with the fast axis aligned with the contact load. Two elastomer strips (nominally 2.5 mm wide, 24 mm long and 2 mm thick) were positioned between the fibres and top gauge block (Figure A-3b). Static loads were applied ranging from 0 N to 80 N at 5 N increments and wavelength and load data were obtained in an identical manner to that described for the first protocol. The sensitivities to transverse load, for

both fast and slow axes and based on spectral separation, were also calculated as described above.

The objective of the third and final protocol was also to test the predictions of sensitivity dependence on modulus obtained from the contact and stress calculations. The fibre was subjected to contact between two layers of the conforming elastomer. In this protocol elastomer strips, of identical nominal dimensions to those above, were positioned between the fibres and both the top and bottom gauge blocks (Figure A-3c). Applied static loads were applied ranging from 0 N to 30 N at 5 N increments and wavelength and load data were obtained in an identical manner to that described for the first scenario. The sensitivities to transverse load, for both fast and slow axes and based on spectral separation, were also calculated as described above.

3. Results

A. Theory

Figure 4a shows the values of the contact angle θ, determined using Equations A-8 and A-9, for applied transverse loads F ranging from 0 N/mm to 3 N/mm. Each curve shown corresponds to a single value of the conforming body (Body 2) Young's modulus. As shown, for a given value of the Young's modulus, the magnitude of the contact angle monotonically increases from zero (*i.e.* point contact) with increasing transverse load to a maximum value, θ_{MAX} at 3 N/mm. The minimum value of θ_{MAX} (Figure A-4b) is 0.80˚ for a Young's modulus of 20 MPa and the maximum value is 5.0˚ for a Young's modulus of 0.5 MPa. The maximum contact length coincides with the maximum contact angle (*i.e.* 5.0˚) and was found to be 10.9 μm. Therefore, the restriction on the contact length a (*i.e.*

$a \leq R/5 =$ 12.5 μm) was satisfied, thereby validating the use of Equations A-5 through A-7 to estimate the principal stresses resulting from fibre/elastomer contact.

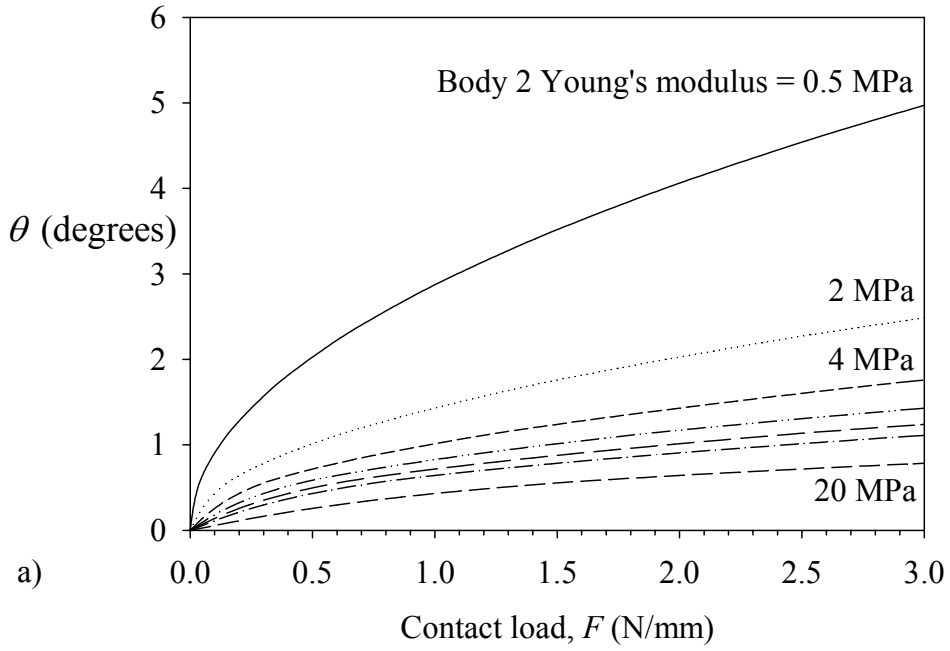

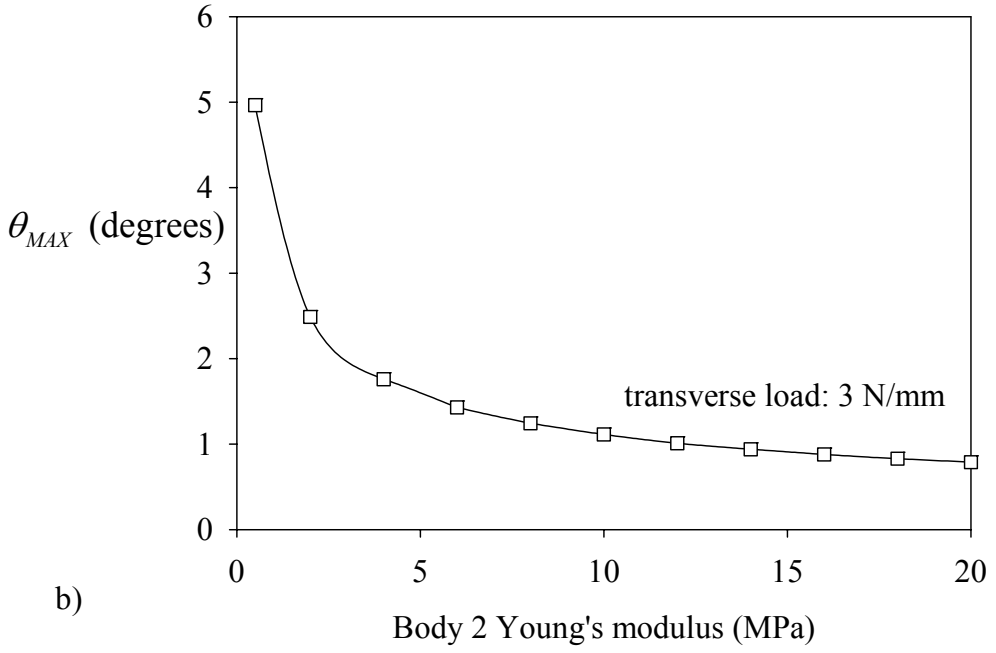

Figure A-4: a) contact model-predicted values of the contact angle θ between the fibre and conforming body, for various values of the conforming body Young's modulus, versus applied transverse load F. Numeric values shown near curves represent the

Young's modulus specific to that curve. To preserve clarity, modulus values for 6 MPa ($-\cdots-$), 8 MPa ($--$) and 10 MPa ($-\cdot-$) are not shown. b) model-predicted variation of maximum contact angle θ_{MAX}, at 3 N/mm, versus Young's modulus of conforming body over range of values found in cartilage.

Figures A-5 and A-6 show the principal stresses in the fibre, calculated using the range of contact angles plotted in Figure A-4b, along the Oy and Ox axes, respectively. Principal stresses aligned with the X-axis (σ_x) are plotted relative to the left-vertical axes (Figures A-5 and A-6). Principal stresses aligned with the Y-axis (σ_y) are plotted relative to the right-vertical axes (Figures A-5 and A-6). The arrows leading from E = 20 MPa to E = 0.5 MPa, within the plot area of both Figure A-5 and A-6, indicate that the curves plotted are for different values of Young's modulus range (*i.e.* 0.5 MPa to 20 MPa). In both Figure A-5 and A-6, the horizontal axis scale denotes the radial distance from the core along the Oy (Figure 5) and Ox (Figure 6) axes, respectively. All stress magnitudes have been normalized relative to the principal stress magnitude at the fibre core for E = 20 MPa (*i.e.* σ_x^* and σ_y^*). As shown, the stresses are greatest in magnitude at the fibre core and the magnitudes decrease as the radius increases.

In the region of the fibre core (*i.e.* radius from 0 μm to 4 μm) principal stress magnitudes are approximately constant, as shown in Figures A-5 and A-6 (outside radius of core denoted) and in Table A-1. Moreover, the difference in stress magnitude (Table A-1) between the case of E = 0.5 MPa and the case of E = 20 MPa, for both axes *Ox* and *Oy*, is modest. Therefore, the variation in Young's modulus of Body 2 has a negligible effect on the stresses created within the core as a result of the transverse load.

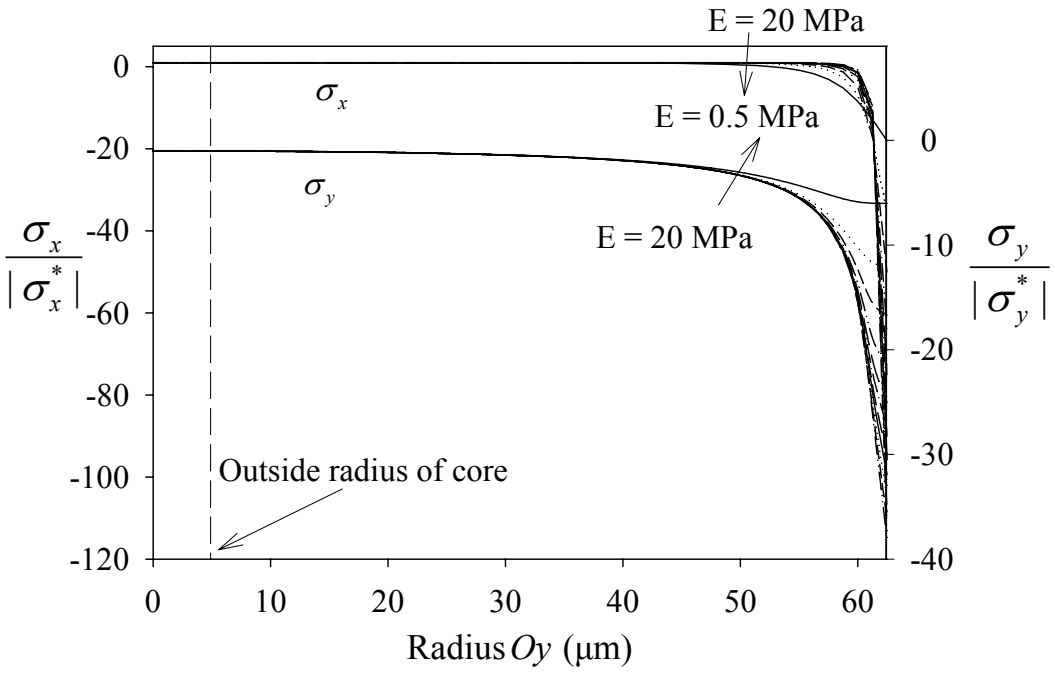

Figure A-5: principal stresses along the Oy axis of the fibre. Each line corresponds to a different contact angle (Young's modulus of Body 2). Outside radius of fibre core is also noted. Asterisk (*) indicates that stress magnitudes are normalized to the stresses found for the case of E = 20 MPa.

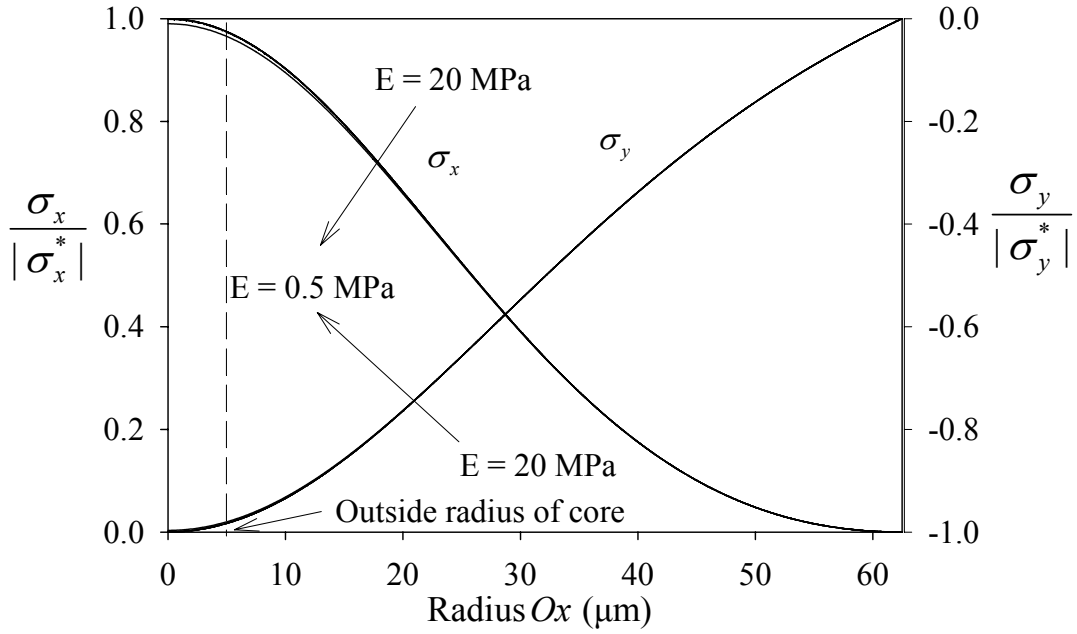

Figure A-6: principal stresses along the Ox axis of the fibre. Each line corresponds to a different contact angle (Young's modulus of Body 2). Asterisk (*) indicates that stress magnitudes are normalized to the stresses found for the case of E = 20 MPa.

Table A-1: normalized principal stress magnitudes for lowest (0.5 MPa) and highest (20 MPa) values of Body 2 modulus at the fibre centre and outside diameter of the fibre core. Stress magnitudes given for both the *Ox* and *Oy* axis.

		Ox axis			
		E = 0.5 MPa		E = 20 MPa	
Location	radius (μm)	$\sigma_x / \lvert\sigma_x^*\rvert$	$\sigma_y / \lvert\sigma_y^*\rvert$	$\sigma_x / \lvert\sigma_x^*\rvert$	$\sigma_y / \lvert\sigma_y^*\rvert$
fibre centre	0	0.990	-0.997	1.00	-1.00
outside diameter of fibre core	4	0.976	-0.987	0.986	-0.991

		Oy axis			
		E = 0.5 MPa		E = 20 MPa	
Location	radius (μm)	$\sigma_x / \lvert\sigma_x^*\rvert$	$\sigma_y / \lvert\sigma_y^*\rvert$	$\sigma_x / \lvert\sigma_x^*\rvert$	$\sigma_y / \lvert\sigma_y^*\rvert$
fibre centre	0	0.990	-0.997	1.00	-1.00
outside diameter of fibre core	4	0.990	-1.00	1.00	-1.005

B. Experiments

Example data from protocol 1, conducted to verify the performance and methods associated with the loading apparatus, is shown in Figure A-7. When the transverse load was applied to the fast axis, the means of the regression-calculated sensitivities of the fast and slow axes are 0.0267 ± 6.1E^{-4} nm/(N/mm) (mean ± standard deviation) and 0.121 ± 5.8E^{-4} nm/(N/mm), respectively. When the transverse load was applied to the slow axis, the mean sensitivities of the fast and slow axes are 0.0674 ± 5.9E^{-4} nm/(N/mm) and -0.0210 ± 1.7E^{-3} nm/(N/mm), respectively. In all experiments, the variation in Bragg wavelength with applied load exhibited linearity (Table A-2). The minimum correlation coefficient (r-squared) is 0.989. The sensitivity results for protocol 1 are also in

agreement with those presented by previous investigators of Bow Tie fibre (Table A-2) [27]. The mean relative difference in the sensitivities calculated in this work compared to reference values presented by Ye *et.al.* (2002) is 15.9 % and ranges from -3.2 % to 25.0 %.

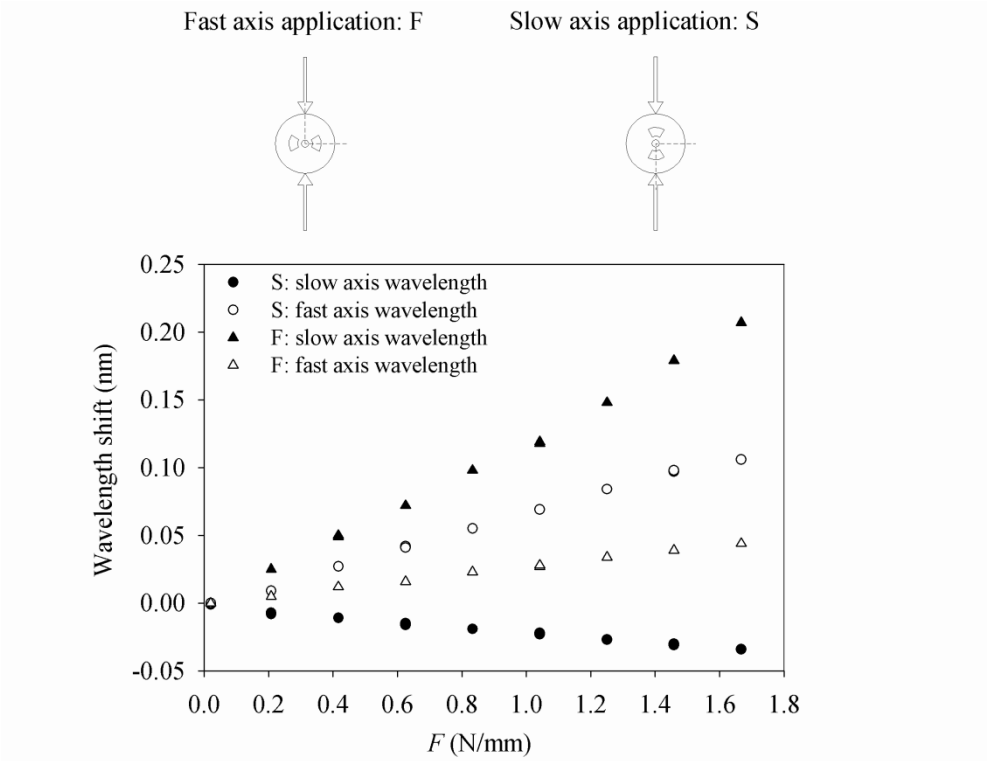

Figure A-7: Example wavelength shift versus transverse load data obtained from protocol 1. Data is shown for transverse loading of both fast axis (F:) and slow axis (S:). Horizontal error bars (± 0.0185 N/mm) are not clearly visible at this scale but are based on published non-repeatability of load cell. Vertical error bars (± 0.005 nm), also not shown, correspond to published reproducibility of optical spectrum analyzer.

Table A-2: Linear regression-calculated sensitivities obtained from Bragg wavelength versus load data for protocol 1 and for load applied along both the fast and slow axis. Sensitivity also expressed in terms of spectral separation (sep.). For comparison, apparent sensitivities from previous investigators also noted.

		Sensitivity (nm/N/mm)			Correlation coefficient	
Load application axis	trial	Slow axis	Fast axis	Spectral sep.	Slow axis	Fast axis
fast axis	1	0.121	0.0271	0.0939	0.997	0.998
	2	0.121	0.0260	0.0950	0.998	0.996
	3	0.122	0.0270	0.0950	0.997	0.995
	mean	0.121	0.0267	0.0946	0.997	0.996
Apparent sensitivity estimated from Ye *et.al.* (2002)		0.125	0.0220			
slow axis	1	-0.0219	0.0681	-0.0900	0.989	0.997
	2	-0.0191	0.0670	-0.0861	0.995	0.995
	3	-0.0221	0.0672	-0.0893	0.996	0.996
	mean	-0.0210	0.0674	-0.0885	0.993	0.996
Apparent sensitivity estimated from Ye *et.al.* (2002)		-0.0280	0.0560			

When the transverse load sensitivity is expressed in terms of spectral separation, as defined in the Methods, the mean sensitivities to load are 0.0946 nm/(N/mm) (*i.e.* 0.121 – 0.0267 nm/(N/mm)) and -0.0885 nm/(N/mm) when the load was applied along the fast and slow axis, respectively (Table A-2).

Typical data obtained from protocol 2 is shown in Figures A-8, A-9a and A-9b. As shown in Figure A-8 and A-9a, the wavelength shifts increase linearly with absolute load Q until the load exceeds Q^*. Beyond Q^*, the wavelength shifts continue to increase linearly with absolute load; however, the slope of the data is less than the slope of the data below Q^*. The load Q^* was estimated from the intersection of the linear-regression calculated best-fit lines of the data before (line A in Figure A-8) and after (line B) the

reduction in slope. The mean magnitude of Q^* is 10.80 ± 1.8 N considering all data collected for protocol 2 (Table A-3).

The reduction in slope described above is a result of contact between the opposed elastomer-steel surfaces adjacent to the fibre (Figure A-10a). This contact coincided with the load Q^* which is illustrated in Figure A-8. The reduction in slope indicates a reduction in load transmission through the fibre due to load transmission through the elastomer to the gauge block. At higher loads, the actual load transmitted to the fibre is represented by:

$$F = (Q_i - Q^*)\frac{D}{wl} + \frac{Q^*}{l} \qquad \text{(A-12)}$$

where Q_i is the absolute load; Q^* is the absolute load at which the reduction in slope occurs (Figure A-8); D is the linear dimension over which the elastomer-steel or elastomer-elastomer contact is prevented by the fibre (Figure A-10a and A-10b); w is the width of the elastomer strip, and; l is the total length of each elastomer strip along the axis of the fibre. The ratio D/wl gives the proportion of the load transmitted to the fibre per unit of fibre length. The dimension D was determined optically, by observing the contact through a microscope objective, and was found to be equal to approximately twice the fibre diameter for both protocols 2 and 3 over the wide range of loads exceeding Q^*.

Figure A-9b shows wavelength shifts for both the fast and slow axes for increasing transverse load F (N/mm). In Figure A-9b, transverse loads are expressed per unit of fibre length and, starting at Q^*, were calculated using Equation A-12. The mean transverse load sensitivity calculated using data from the three trials in protocol 2, based

on spectral separation, is 0.0900 ± 5.1E^{-3} nm/(N/mm) (Table 3). This sensitivity is 4.3 % lower than the average sensitivity found in protocol 1 for spectral separation when loading along the fast axis. The mean correlation coefficient for the spectral separation data is 0.956 (Table A-3).

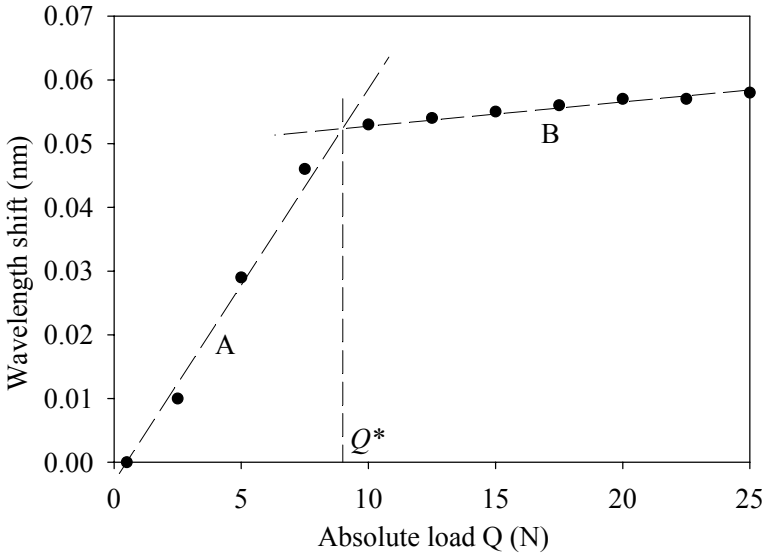

Figure A-8: typical Bragg wavelength shift versus load data measured for the slow axis in protocol 2. Lines A and B through data points were obtained through linear-regression calculations. Q^* was estimated by calculating the intersection of lines A and B, which have differing slopes due to the elastomer-steel contact described previously.

Typical data obtained from protocol 3 is shown in Figures A-11a and A-11b. For protocol 3, the average magnitude of Q^*, over three trials, is less than 1 N. Because of the low magnitude of Q^*, data below 1 N is not reported here. The wavelength shifts of both the fast and slow axis Bragg spectrums monotonically increase with increasing load. The sensitivities, based on fast and slow axis wavelength shifts and on spectral separation, are approximated as linear, using the same regression techniques used in protocols 1 and 2.

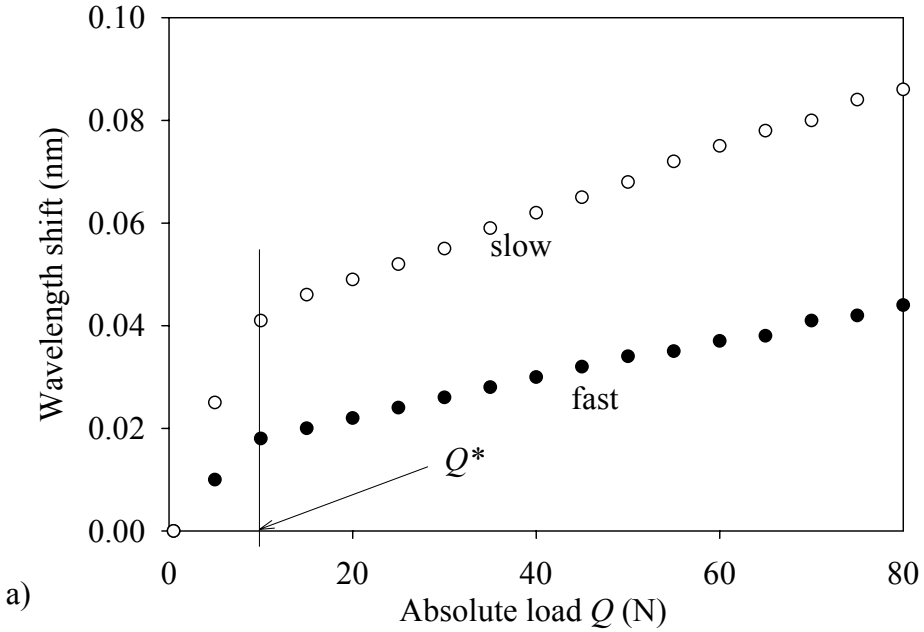

a)

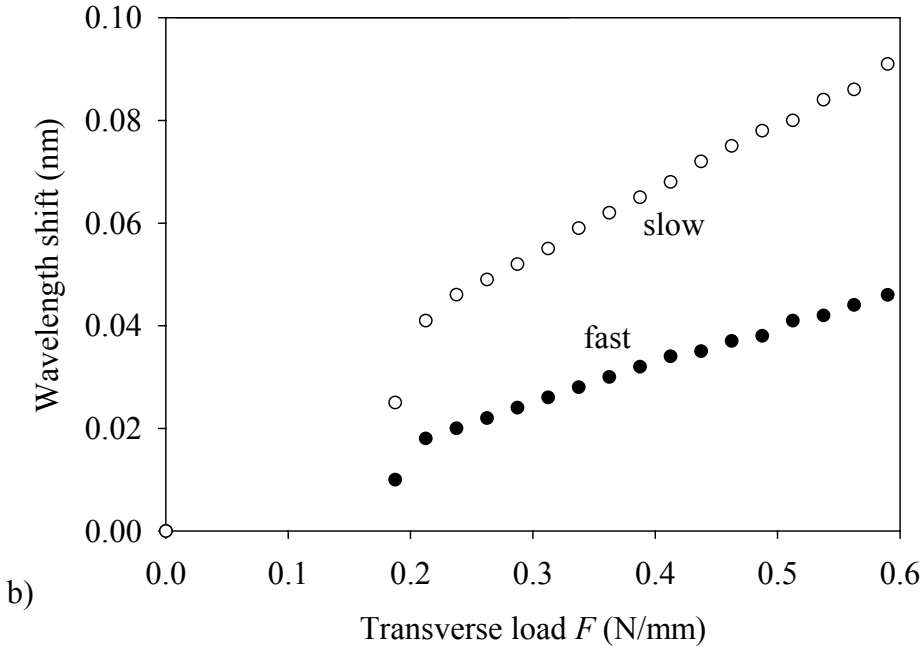

b)

Figure A-9: a) wavelength shift for increasing absolute load data obtained from protocol 2, trial 2. Load was applied along the fast axis of the fibre. Horizontal error bars (± 0.45 N) were not clearly visible at given scale and are not shown. b) typical wavelength shift for increasing transverse load, expressed per unit of fibre length, data. Slow and fast notations in plot area indicate that data corresponds to either the slow axis or fast axis Bragg wavelength, respectively.

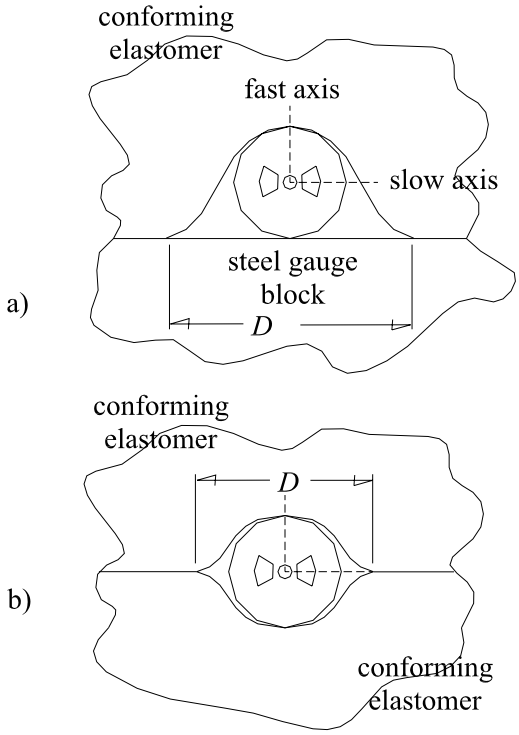

Figure A-10: a) close-up view (scaled for clarity) showing optical fibre compressed between conforming elastomer and gauge block. Fibre fast and slow axes noted. *D* is the distance between points of elastomer contact on gauge block. b) close-up view showing fibre compressed between two layers of conforming elastomer.

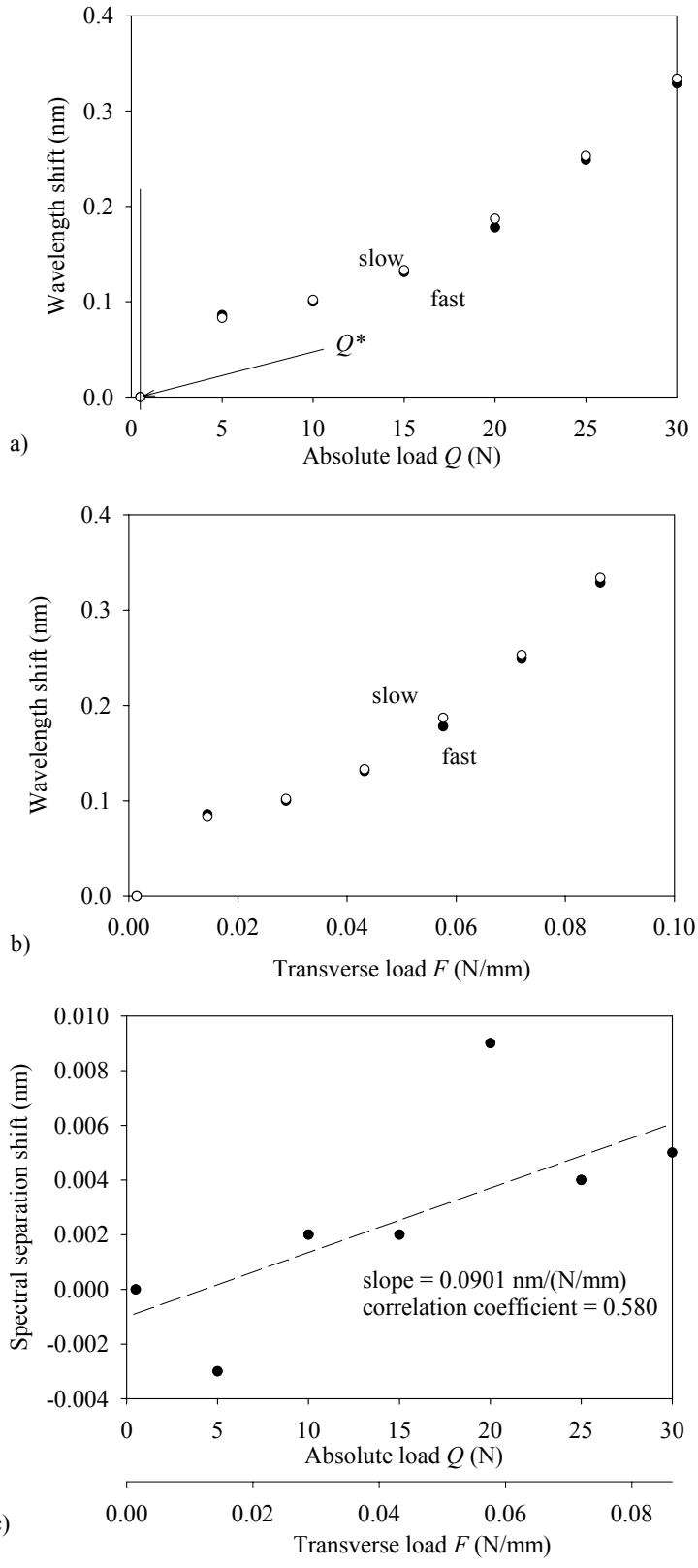

Figure A-11: a) wavelength shift for increasing absolute load data obtained from protocol 3, trial 1. Load was applied along the fast axis of the fibre. b) wavelength shift for

increasing transverse load, expressed per unit of fibre length, data. c) spectral separation calculated from fast and slow axis data. Dashed line represents linear-regression fit for plotted data. Slow and fast notations in plot area indicate that data corresponds to either the slow axis or fast axis Bragg wavelength, respectively.

Table A-3: Linear regression-calculated sensitivities, based on spectral separation, obtained from Bragg wavelength versus load data for protocol 2 and 3.

Protocol	trial	Q^* (N)	Spectral separation sensitivity (nm/N/mm)	Correlation coefficient
2	1	12.8	0.0912	0.925
	2	9.54	0.0942	0.976
	3	10.0	0.0845	0.967
	mean	10.8	0.0900	0.956
3	1	< 1	0.0901	0.580
	2	< 1	0.0939	0.221
	3	< 1	0.0921	0.595
	mean		0.0920	0.465

The wavelength shifts measured in protocol 3 are greater than the wavelength shifts for protocol 1 and 2, for reasons that will be discussed subsequently. The average transverse load sensitivity calculated using data from the three trials in protocol 3 (Table A-3), based on spectral separation, is 0.0920 ± $2.0E^{-3}$ nm/(N/mm). This sensitivity value is 2.1% lower than the average sensitivity value found in protocol 1 for spectral separation when loading along the fast axis of the fibre. The mean correlation coefficient for the spectral separation data is 0.465.

4. Discussion

The results of the theoretical calculations of contact length and stress, show that the principal stresses in the fibre core due to transverse load are relatively independent of the Young's modulii of the contacting materials (Table A-1). The principal reason for this result is that the contact length between the optical fibre (Body 1 in Figure A-2) and conforming material (Body 2) remains small (1.75 μm to 10.9 μm) relative to the

diameter of the optical fibre (*i.e.* 125 μm) over the range of modeled Young's modulii for Body 2 (*i.e.* 0.5 MPa to 20 MPa). As birefringence is a function of the principal stresses in the fibre core (Equations A-2 and A-4), these results indicate that load-induced birefringence is also insensitive to modulus. Therefore, the sensitivity of the birefringent fibre to transverse loads caused by conforming contact is expected to be modulus-independent.

Stresses arising from Hertzian contact can be readily calculated. For an optical fibre in Hertzian contact, these stresses are within 1% of the values calculated here for conforming contact (Table A-1). Because the stresses for conforming contact are nearly identical to those for Hertzian contact, the experimentally measured sensitivity of birefringence (expressed by spectral separation) to transverse load for protocol 1 (Hertzian contact, Table A-2) is expected to be nearly identical to that measured in protocols 2 and 3 (conforming contact, Table A-3).

The sensitivity of fibre birefringence to transverse load for protocols 2 and 3 (conforming contact with low modulus elastomer) are within of 4.9 % and 2.7 %, respectively, of the sensitivities measured in protocol 1 (Hertzian contact). These results demonstrate the modulus independence predicted by the plane elasticity model.

In the context of contact load measurements between conforming materials, the magnitude of Q^* coincides with a change in the slope of the wavelength shift versus contact load data (Figure A-9a and Figure A-11a). At loads below Q^*, the contact load between the fibre and elastomer is Q. However, beyond Q^* there is contact between the fibre and elastomer as well as between the elastomer and steel (protocol 2), or the opposed elastomer strips (protocol 3), and the contact load is given by Equation A-12.

The change in slope cannot be detected *in situ* because the contact loads are not known; they are the measured parameter. However, beyond Q^* the sensitivity to transverse load F is linear, in the case of protocol 2, or approximately linear, in the case of protocol 3 and, when considering the data for spectral separation, is nearly identical between protocols 1, 2 and 3.

Depending on the application, errors attributed to neglecting Q^* may be insignificant relative to the contact loads considered. In articular joints, contact between opposed cartilage (*i.e.* conforming) surfaces can result in pressures ranging up to 18 MPa [28] and higher. In this work, contact between conforming surfaces was measured in protocol 3. In protocol 3, Q^* was less than 1 N corresponding to a contact load of less than 0.01 N/mm (Figure A-11b) or pressure of 0.08 MPa (based on the fibre diameter). The pressure at Q^* is only 0.4% of peak joint contact pressure (18MPa). Therefore, errors associated with neglecting Q^* are insignificant compared to the full-scale contact pressures in this application.

In bolted joints containing gaskets, contact pressures between conforming gasket materials and non-conforming metals can range up to 100 MPa [29] or higher. In this work, contact between a conforming elastomer and metal surface was measured in protocol 2. In protocol 2, Q^* was approximately 10 N corresponding to a contact load of approximately 0.2 N/mm (Figure A-9b) or pressure of 1.6 MPa. The pressure at Q^* is only 1.6% of peak gasket contact pressure (100 MPa). As above, the errors associated with neglecting Q^* are insignificant compared to the full-scale contact pressures in this application.

As shown in Table A-3, the correlation coefficients for the spectral separation data of protocol 3 (mean: 0.465) are low, relative to those of protocol 2 (mean: 0.956) due to scatter in the spectral separation data for protocol 3 (Figure A-11c). Under load, non-uniform compression of the elastomer strips above and below the birefringent fibre perturbed the fibre orientation relative to the direction of the applied transverse load. These changes in fibre orientation, contributed to the scatter in spectral separation data (Figure A-11c). In protocol 2, this problem did not arise because the bottom gauge block ensured uniform compression of the upper elastomer strip.

Another factor that contributed to scatter in the protocol 3 data was the low magnitude of the applied loads. Transverse loads in protocol 3 were lower than those of protocol 2 (range: 0 N/mm to 0.6 N/mm) and, therefore, caused less spectral separation (Figure A-11c) than in protocol 2 (Figure A-9b). The spectral separations in protocol 3 (Figure A-11c) are comparable to the highest resolution achievable with the optical spectrum analyzer (*i.e.* $\leq \pm 0.0025$ nm[30]). Therefore, measurement errors associated with the optical spectrum analyzer also contributed to scatter of spectral separation data.

The large wavelength shifts of protocol 3, relative to those of protocol 2, exhibit non-linearity which is due to the non-linear relationship between Poisson dilation of the elastomer strips and load. However, the linear regressions of wavelength shift and spectral separation data provide spectral separation sensitivities matching those found in protocols 1 and 2. Further development of the loading apparatus will focus on minimizing the experimental effects leading to non-linearity and scatter.

The theoretical and experimental results show that birefringent fibre can be used to make modulus-independent measurements of transverse contact loads beyond Q^*.

Because the fibre is capable of modulus-independent load measurement, pre-calibration of fibre-based sensors is not necessary. This is a distinct advantage over other, film-based, contact sensors that have been shown to have modulus dependent accuracy [14].

5. Conclusions

A theoretical and experimental investigation of the effect on transverse load sensitivity of Bragg gratings in birefringent fibres to conforming contact between elastically dissimilar materials was conducted. The theoretical investigation included applying a plane elasticity model to predict the contact dimensions between conforming materials and also a plane elasticity model to predict the principal stresses created as a result of this contact. The experimental investigation was structured to verify the theoretical predictions and involved measuring the sensitivity to transverse load of Bragg gratings in birefringent fibre when subjected to conforming contact. Both the theoretical and experimental results showed that birefringent optical fibre can be used to make modulus-independent measurements of contact load. Therefore, Bragg gratings could be applied to conforming contact load measurements while avoiding some of the complications associated with existing contact sensors; specifically, the necessity to pre-calibrate using materials with identical mechanical properties to those found *in situ*.

6. Acknowledgements

The authors thank the Natural Sciences and Engineering Research Council (Canada) for financial support.

References

[1] Chehura, E., Ye, C.-C., Staines, S. E., James, S. W., and Tatam, R. P., 2004, "Characterization of the response of fibre Bragg gratings fabricated in stress and geometrically induced high birefringence fibres to temperature and transverse load," Smart Materials and Structures, 13, pp. 888-895.

[2] Okamoto, K., Hosaka, T., and Edahiro, T., 1981, "Stress analysis of optical fibers by a finite element method," IEEE Journal of Quantum Electronics, QE-17(10), pp. 2123-2129.

[3] Measures, R. M., 2001, Structural Health Monitoring with Fiber Optic Technology, Academic Press.

[4] Udd, E., Nelson, D., and Lawrence, C., 1996, "Three Axis Strain and Temperature Fiber Optic Grating Sensor," Proceedings of SPIE, 2718, pp. 104-109.

[5] Wierzba, P., and Kosmowski, B. B., 2003, "Application of polarisation-maintaining side-hole fibres to direct force measurement," Opto-Electronics Review, 11(4), pp. 305-312.

[6] Abe, I., Frazao, O., Schiller, M. W., Noqueira, R. N., Kalinowski, H. J., and Pinto, J. L., 2006, "Bragg gratings in normal and reduced diameter high birefringence fibre optics," Measurement Science and Technology, 17, pp. 1477-1484.

[7] Johnson, K. L., 1987, Contact mechanics, Cambridge University Press.

[8] Ferguson-Pell, M., and Cardi, M., 1993, "Prototype development and comparative evaluation of wheelchair pressure mapping system," Assistive Technology, 5(2), pp. 78-91.

[9] Komi, E. R., Roberts, J. R., and Rothberg, S. J., 2008, "Measurement and analysis of grip force during a golf shot," Proceedings of the IMechE vol.222 Part P: Journal of Sports Engineering and Technology.

[10] Yokoyama, K., Okazaki, M., and Komito, T., 1998, "Effect of contact pressure and thermal degradation on the sealibility of O-ring," JSAE Review, 19, pp. 123-128.

[11] Niemczyk, P., Cummings, K., Sarvazyan, A., Bancila, E., Ward, W., and Weiss, R., 1998, "Correlation of mechanical imaging and histopathology of radical prostatectomy specimens: A pilot stufy for detecting prostate cancer," The Journal of Urology, 160, pp. 797-801.

[12] Ferguson, S., Bryant, J., Ganz, R., and Ito, K., 2000, "The acetabular labrum seal: a poroelastic finite element model," Clinical Biomechanics, 15(6), pp. 463-468.

[13] Barker, M. K., and Seedhom, B. B., 2001, "The relationship of the compressive modulus of articular cartilage: does cartilage optimize its modulus so as to minimize the strains arising in it due to the prevalent loading regime?," Rheumatology, 40, pp. 274-284.

[14] Wu, J. Z., Herzog, W., and Epstein, M., 1998, "Effects of inserting a pressensor film into articular joints on the actual contact mechanics," Journal of Biomechanical Engineering, 120(5), pp. 655-659.

[15] Ciavarella, M., and Decuzzi, P., 2001, "The state of stress induced by the plane frictionless cylindrical contact. I. The case of elastic similarity," International Journal of Solids and Structures, 38, pp. 4507-4523.

[16] Ciavarella, M., and Decuzzi, P., 2001, "The state of stress induced by plane frictionless cylindrical contact. II. The general case (elastic dissimilarity)," International Journal of Solids and Structures, 38, pp. 4525-4533.

[17] Hondros, G., 1959, "The evaluation of Poisson's ratio and the modulus of materials of a low tensile resistance by the Brazilian (indirect tensile) test with particular reference to concrete," Australian Journal of Applied Science, 10, pp. 243-268.

[18] Hill, K. O., Fujii, Y., Johnson, D. C., and Kawasaki, B. S., 1978, "Photosensitivity in optical fiber waveguides: Application to reflection filter fabrication," Applied Physics Letters, 32(10), pp. 647-649.

[19] Huang, S., LeBlanc, M., Ohn, M. M., and Measures, R. M., 1995, "Bragg intragrating structural sensing," Applied Optics, 34(22), pp. 5003-5009.

[20] Barlow, A. J., and Payne, D., 1983, "The stress-optic effect in optical fibers," IEEE Journal of Quantum Electronics, QE-19(5), pp. 834-839.

[21] Chen, G., Liu, L., Jia, H., Yu, J., Xu, L., and Wang, W., 2004, "Simultaneous strain and temperature measurements with fiber Bragg grating written in novel hi-bi optical fibre," IEEE Photonics Technology Letters, 16(1), pp. 221-223.

[22] 1992, Fundamentals of fibre optics in telecommunication and sensor systems, John Wiley & Sons Inc., New Delhi, India.

[23] Carrara, S. L. A., Kim, B. Y., and Shaw, H. J., 1986, "Elasto-optic alignment of birefringent axes in polarization-holding fiber," Optics Letters, 11(7), pp. 470-472.

[24] Bingjun, F., Wang, S., and Zhonkui, L., 2001, Frontiers of rock mechanics and sustainable development in the 21st century, Swets and Zeitlinger B.V.

[25] Han, S.-K., Federico, S., Epstein, M., and Herzog, W., 2005, "An articular cartilage contact model based on real surface geometry," Journal of Biomechanics, 38, pp. 179-184.

[26] Elastomers, D. P., 2003, "Viton(R) fluoroelastomer: technical information,"U.S.A.

[27] Ye, C.-C., Staines, S. E., James, S. W., and Tatum, R. P., 2002, "A polarization-maintaining fibre Bragg grating interrogation system for multi-axis strain sensing," Measurement Science and Technology, 13, pp. 1446-1449.

[28] Hodge, W. A., Fuan, R. S., Carlson, K. L., Burgess, R. G., Harris, W. H., and Mann, R. W., 1986, "Contact pressures in the human hip joint measured in vivo," Proceedings of the National Academy of Sciences USA, 83, pp. 2789-2883.

[29] Krishna, M. M., Shunmugam, M. S., and Prasad, N. S., 2007, "A study on the sealing performance of bolted flange joints with gaskets using finite element analysis," International Journal of Pressure Vessels and Piping, 84, pp. 349-357.

[30] Canal, C. E., Hung, C. T., and Ateshan, G. A., 2008, "Two-dimensional strain fields on the cross-section of the bovine humeral head under contact loading," Journal of Biomechanics, 41, pp. 3145-3151.

Appendix B: An in-fibre Bragg grating sensor for contact force and stress measurements in articular joints

(2010, Measurement Science and Technology, volume 21 (115803))

An in-fibre Bragg grating sensor for contact force and stress measurements in articular joints

Christopher R. Dennison[1], Peter M. Wild[1], David R. Wilson[2], and Michael K. Gilbart[2]

[1]*Department of Mechanical Engineering, University of Victoria, British Columbia, Canada*

[2]*Department of Orthopaedics and Centre for Hip Health and Mobility, University of British Columbia, Canada*

Abstract

We present an in-fibre Bragg grating based sensor (240 μm diameter) for contact force/stress measurements in articular joints. The contact force sensor, and another Bragg grating based pressure sensor (400 μm diameter), are used to conduct the first simultaneous measurements of contact force/stress and fluid pressure in intact cadaveric human hips. The contact force/stress sensor addresses limitations associated with stress sensitive films, the current standard tools for contact measurements in joints, including cartilage modulus dependent sensitivity of films and the necessity to remove biomechanically relevant anatomy to implant the films. Because stress sensitive films require removal of anatomy, it has been impossible to validate the mechanical rationale underlying preventive or corrective surgeries, which repair these anatomies, by conducting simultaneous stress and pressure measurements in intact hips. Methods are presented to insert the Bragg grating based sensors into the joint, while relevant anatomy is left largely intact. Sensor performance is predicted using numerical models, and the predicted sensitivity is verified through experimental calibrations. Contact force/stress and pressure measurements in cadaveric joints exhibited repeatability. With further validation, the Bragg grating based sensors could be used to study the currently unknown relationships between contact forces and pressures in both healthy and degenerated joints.

1. Introduction

Knowledge of *in vivo* forces and stresses in articular joints, such as the knee, hip, ankle and shoulder, is of great value to clinicians, researchers and prosthetic implant designers [1]. Understanding these stresses is thought to be central in understanding etiology and progression of degenerative joint diseases such as osteoarthritis [1, 2] as well as the effects of clinical interventions that are meant to halt or slow the progression of degeneration [1, 3] in natural and prosthetic joints [1, 3-8]. In the hip, excessive duration and magnitude of force and stress on the conforming cartilage surfaces of the pelvis and femur can predict the onset of osteoarthritis [2, 9]. It is also widely believed that clinical symptoms, such as pain and cartilage degeneration, are related to how stress is distributed across the joint [10, 11].

Ex vivo measurements of mechanical quantities, such as forces and stresses, in cadaver joints are the basis of the rationale for many conservative and surgical treatments for joint disorders. These measurements have been done in the knee [12] and in the hip [13, 14]. In these studies, cadaveric specimens are loaded in test rigs to simulate the physiological loads applied during standing, weight-bearing or activity. Measurements of contact area and force and stress distribution have been made between the conforming cartilage surfaces of the joint using commercially available stress sensitive films (e.g. [15-17]).

The most widely-used tools for measuring joint contact stress, Prescale Film (Fuji Photo Film Co., Japan) and I-Scan (Tekscan Inc., Boston, MA) [9, 18], have substantial limitations. Both are stress sensitive films that are inserted between the contacting surfaces of the joint. I-Scan provides continuous measurements but Prescale measures

only peak stress. Experimental evidence shows that the accuracy of I-Scan and Prescale is a function of the elastic modulus of the contacting material [19]. As a consequence, these sensors must be pre-calibrated using materials with similar modulus to those found *in situ* which, in the case of biological tissues (*e.g.* cartilage), are rarely available *a priori*. These sensors have also been shown to alter the natural mechanics of the joint. The degree to which these sensors affect joint mechanics is a function of film thickness and elastic modulus, film curvature and cartilage elastic modulus [19-21]. The linear-elastic modulus of cartilage throughout the human body can range from, nominally, 0.5 MPa [22] to 20 MPa [23].

Stress sensitive films have been used in the hip, but their application is severely limited by the amount of dissection required to use them in this joint. To apply these sensors, the hip must first be dissected to allow access to the femoral head. Dissection can include large incisions in, or complete removal of, biomechanically relevant accessory structures such as the joint capsule. These accessory structures play a crucial role in hip mechanics and preserving synovial fluid pressurization and lubrication [22, 24, 25]. After dissection is complete, access to the femoral head is gained by removing the femoral head from the acetabulum. This process is referred to as disarticulation and has been shown to negatively impact natural hip mechanics by disrupting synovial fluid pressurization and lubrication which are both thought to be closely coupled to contact stress [22, 24, 25]. Because stress sensitive films require removal of accessory structures, it has been impossible to validate the mechanical rationale underlying preventive or corrective surgeries, that repair these structures, by conducting simultaneous stress and

pressure measurements in intact hips (*i.e.* cadaveric or living hips with all accessory structures in place) [2].

A fibre optic technology, originally developed for telecommunications, has the potential to address some of the limitations associated with stress sensitive films. *In-fibre Bragg gratings* (FBGs) are formed in standard, communications grade, single-mode optical fibres and can be used to sense several mechanical parameters: temperature [26], strain [27], pressure [28] and contact force [29] among others. They also possess key characteristics which are attractive for application to the hip: small size – diameters of 125 μm or smaller and sensing lengths as small as 1 mm, mechanical compliance and biocompatibility. Because of their small size, FBGs have the potential to be inserted into joint spaces using insertion techniques that could not be used with stress sensitive films (*e.g.* arthroscopically) and that do not require removal of biomechanically relevant accessory structures. More specifically, FBG-based sensors could potentially be applied in intact hips to measure local forces and stresses on the cartilage surfaces, while avoiding limitations of stress sensitive films.

Despite their potential utility, application of FBGs in articular joints has been limited. Mohanty *et. al.* (2007) describe the only reported application of an FBG-based sensor in an articular joint: the knee. In this application, the FBG sensor was a rectangular array of Bragg gratings inside a tibial spacer, that was used to measure changes in contact stresses caused by joint misalignments [30]. However, insertion of the sensor between the joint condyles requires removal of significant portions of the joint capsule. This insertion approach is too interventional for studies of the natural hip [2].

The objective of the work reported here was to develop an FBG-based contact force/stress sensor for the hip that addresses the key limitations associated with stress sensitive films, namely, modulus dependent measurements and the necessity to dissect joints prior to sensor application, and that requires minimal dissection of the hip.

2. Contact stress and load measurements in hips

The hip is a ball-and-socket joint [31] that allows relative motion between the pelvis and femur (Figure B-1a). The relative motion is defined for three rotational degrees of freedom: flexion/extension anteriorly to posteriorly; abduction/adduction laterally to medially; and internal rotation about the superior-to-inferior axis. Articulation is between the acetabulum of the pelvis and the femoral head (Figure B-1b).

The articular surfaces are comprised of hyaline cartilage which has a low coefficient of friction (Figure B-1b). This cartilage is comprised of a collagenous solid matrix with interconnected pores that contain joint lubricating synovial fluid [22]. As mentioned previously, the elastic mechanical properties of cartilage can vary over a considerable range. For example, in studies where cartilage strains are assumed infinitesimal, linear elastic modulus values have been estimated to range, nominally, from 0.5 MPa [22] to 20 MPa [23]. However, in studies where strain magnitudes are finite (or large relative to infinitesimal strains), non-linear elastic models based on strain energy density are used [32]. Among the many non-linear models, the two-parameter Mooney-Rivlin formulation has been shown to closely approximate the non-linear elastic behavior of cartilage [33-35]. Like the linear-elastic modulus of cartilage, the Mooney-Rivlin parameters, that have the same units as modulus, can also vary over a considerable range from, nominally, 0.3 MPa to 4 MPa.

Between the cartilage surfaces of the acetabulum and femoral head is a central synovial fluid space (Figure B-1b). The synovial fluid in the porous matrix of the cartilage and central space are in fluid contact. Synovial fluid is retained in the central space by the labrum, a fibrocartilagenous lip that is attached the acetabulum. The labrum spans the superior rim of the acetabulum and inferiorly transitions smoothly into the transverse ligament (Figure B-1b) [22]. There is also synovial fluid, outside of the central space, in contact with the regions of the femoral head and femoral neck not covered the labrum. This fluid occupies a peripheral space between the femoral head/neck and interior surface of the fibrous capsule (Figure B-1b). The fibrous capsule encapsulates the entire joint, both superiorly and inferiorly.

Physiologic loads transmitted through the pelvis to the femur can be carried by either hydrostatic pressure of the synovial fluid in the porous matrix and the central space, or, when cartilage contact between the femoral head and acetabulum occurs, by solid stresses within the porous matrix itself [22]. The relative proportion of loads carried by each mechanism depends on a wide range of factors, including the load magnitude, the integrity of joint structures such as the labrum, and the integrity of the cartilage [22]. Experimental investigations of hip mechanics have measured either synovial fluid pressure [25] or contact force/stress [9]. However, to our knowledge, there have been no studies in which simultaneous *ex vivo* measurements of both contact force/stress and hydrostatic pressure have been made in an intact hip. Synovial fluid pressure is measured with pressure sensors in fluid contact with the synovial fluid spaces [25, 36]. However, recently an alternative approach has been presented. Ferguson *et al.* (2003) inserted a pressure sensor though the transverse ligament and into the fossa

(Figure B-1b) and measured hydrostatic pressures within the fat of the fossa. This pressure is believed to be equal to synovial fluid pressure [25]. Encapsulating the pressure sensor within the fossa has the benefit of preventing solid contact between the sensor and cartilage of the femoral head or acetabulum. Because of this benefit, the methods of Ferguson *et al.* (2003) were adopted for the current study.

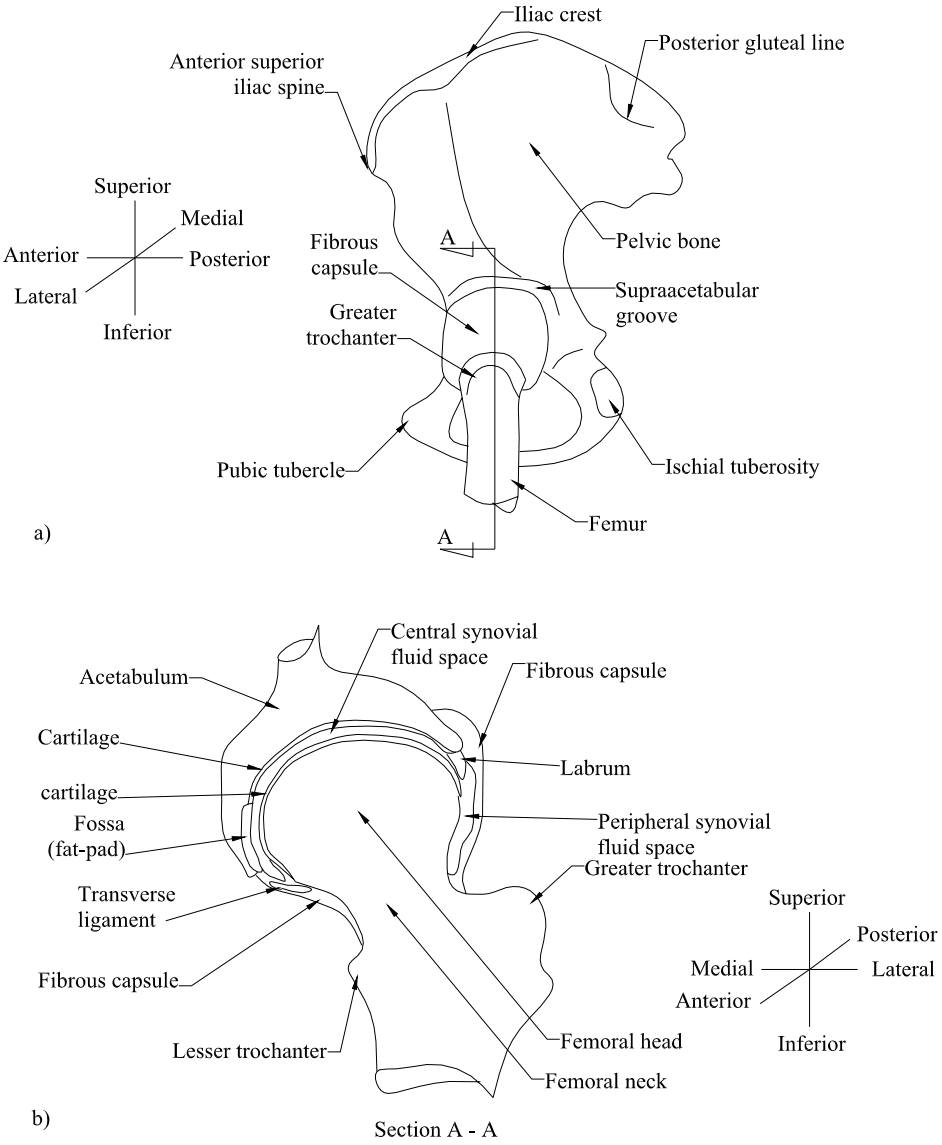

Figure B-1: a) schematic showing left side view (lateral to medial) of the pelvic bone, femur and joint capsule. Section line A-A defines the articular region of the hip joint. b) section-view of hip joint showing relevant anatomy.

3. Materials and methods

3.1 Principles of FBGs

FBGs are a permanent periodic variation in the refractive index of an optical fibre core [37, 38]. The periodic variation is formed by exposing the core of photosensitive optical fibres [39] to ultraviolet light that has a periodic pattern corresponding to the desired period of variation in the refractive index. The magnitude of this variation is influenced by the material properties of the fibre, the duration of exposure to ultraviolet light and the degree and method of fibre photosensitization [38]. The length of the FBG and the magnitude and spatial period of the variation in the refractive index determine the optical spectrum that is reflected from the FBG [38, 40].

When light spanning a broad range of wavelengths propagates in the core of a conventional single-mode fibre [41] and encounters the Bragg grating, a spectrum of wavelengths is reflected. This spectrum is centered at the Bragg wavelength which is given by

$$\lambda_B = 2\Lambda n_0 \tag{B-1}$$

where Λ is the spatial-period of the variation in the refractive index and n_0 is the refractive index of the fibre core (1.458 [38]). Changes in the Bragg wavelength, denoted by $\Delta\lambda_B$, are caused by load-induced strains, $\varepsilon_z, \varepsilon_x, \varepsilon_y$, and can be calculated as [38, 42, 43]:

$$\frac{\Delta\lambda_B}{\lambda_B} = \varepsilon_z - \frac{n_0^2}{2}\left[\varepsilon_z p_{12} + \frac{1}{2}\left(p_{11} + p_{12}\right)\left(\varepsilon_x + \varepsilon_y\right)\right] \tag{B-2}$$

where p_{11} and p_{12} are photo-elastic constants with dimensionless magnitudes of 0.113 and 0.252, respectively; and the coordinate system (*i.e.* x,y,z) to which the strains are

referred is right-handed Cartesian with the z-direction aligned with the fibre axis. These strains can be created by forces, including contact forces that result from compression between elastic materials, applied to the clad of the fibre. Changes in the Bragg wavelength can also be caused by temperature changes at the grating through both a thermo-optic effect [26] and thermal expansion of the optical fibre. Figure B-2 is a schematic showing the orientation of contact forces relative to the fibre axis.

Typically, Bragg gratings in *birefringent* fibre are used for contact force measurements because they have both increased sensitivity to contact forces [29] and small diameter (*i.e.* 125 μm). Gratings in conventional fibre possess poor sensitivity to contact force/stress [29] and are, therefore, not typically used for contact force measurements. The key difference between birefringent fibre and conventional fibre is that birefringent fibre has different refractive indices along directions aligned with the x and y axes. The difference in refractive index between the x and y directions of the fibre core causes the grating to reflect two Bragg spectra, each given by Equation B-1, with n_0 replaced with either n_x or n_y [44]. The physical mechanism causing sensitivity to contact force is stress-induced birefringence [45]. Contact forces induce stresses, the principal directions of which are uniform in the region of the fibre core. However, the magnitudes of the principal stresses are a function of the magnitude of the contact force [29]. Therefore, when the contact force changes, there is predictable change in the principal stress magnitudes and birefringence. These force-induced changes in birefringence cause predictable changes in the spectrum reflected by the Bragg grating, including shifts in the Bragg spectra corresponding to the x and y axes of the fibre.

Birefringent fibres possess higher sensitivity to contact force than non-birefringent fibres because they are typically constructed with stress concentrating features that increase force-induced changes in birefringence [38]. The contact force sensitivity of each type of birefringent fibre is unique. Force sensitivity is also a function of the angular orientation of the stress-applying parts relative to the direction of contact force [29]. The orientation dependence of sensitivity is a key limitation of gratings in birefringent fibre for contact force/stress measurements in the human hip. After insertion into the joint space, fibre orientation relative to the cartilage surfaces, which apply contact forces to the fibre, is difficult to measure or control.

Recently, progress has been made toward increasing the contact force sensitivity of gratings in conventional fibre by packaging the optical fibre, which contains the grating, in compliant polymers. For example, Ngoi *et al.* (2004) report a sensor with increased lateral stress, or contact stress, sensitivity using a grating in a conventional fibre that is coated in a 4 mm diameter coaxial polymer jacket [46]. Contact forces applied to the polymer jacket cause large axial Poisson strains along the axis of the fibre. These large axial strains cause Bragg wavelength shifts that are large compared to those of an un-jacketed fibre subjected to contact forces. For the 4 mm jacketed grating, an increase in contact stress sensitivity of 7 times was reported [46] and further increases can be realized by increasing the jacket diameter [47]. However, in the context of the intact hip where the space between cartilage surfaces is 0.6 mm or smaller, this sensor is too large.

The limitations described above for the polymer jacketed and birefringent sensors are addressed with the sensor described in this work.

3.2 FBG contact force/stress sensor

The prototype sensor is comprised of four main components: a photosensitive optical fibre (*e.g.* SMF-28), a Bragg grating, an incompressible and mechanically compliant polymer annulus, and a Polyimide™ sheath (Figure B-2a). The core of the optical fibre is aligned with the z-axis (Figure B-2a) and contains a 1 mm long Bragg grating. Between the outside diameter of the fibre, D_f, and the inside diameter of the Polyimide™ sheath is the polymer (Dow Corning® 3-1753, Midland MI) annulus which has radial thickness, t_A. The Polyimide™ sheath is coaxial with the fibre and contains both the fibre and polymer annulus, and has an outside diameter, D. Both the Polyimide™ sheath and polymer annulus have length, L, at the midpoint of which is the Bragg grating.

Contact forces, F, applied to the Polyimide™ sheath and aligned with the y-axis (Figure B-2b) are transmitted through the Polyimide™ causing compressive strains in the polymer annulus that are aligned with the y-axis. Because the polymer annulus is approximately incompressible, the volume of the polymer annulus is preserved by tensile strains aligned with the x- and z-axes. These strains are transmitted to the fibre which contains the grating. These transmitted strains cause changes in the Bragg wavelength reflected by the FBG. Because the deformations, and therefore strains, are directly proportional to the contact force, Bragg wavelength changes are proportional to contact force. Over the range of forces considered in this work, Bragg wavelength changes are linearly proportional to contact forces.

The design presented here is similar to that described by Ngoi *et al.* (2004) because it utilizes a coaxial polymer jacket. However, as the results will show, the Polyimide™ sheath of the current design sheath is an important feature that enhances

sensor sensitivity, relative to larger diameter un-sheathed sensors [46]. The presence of the sheath also contributes to reduced *modulus dependence* of sensor sensitivity.

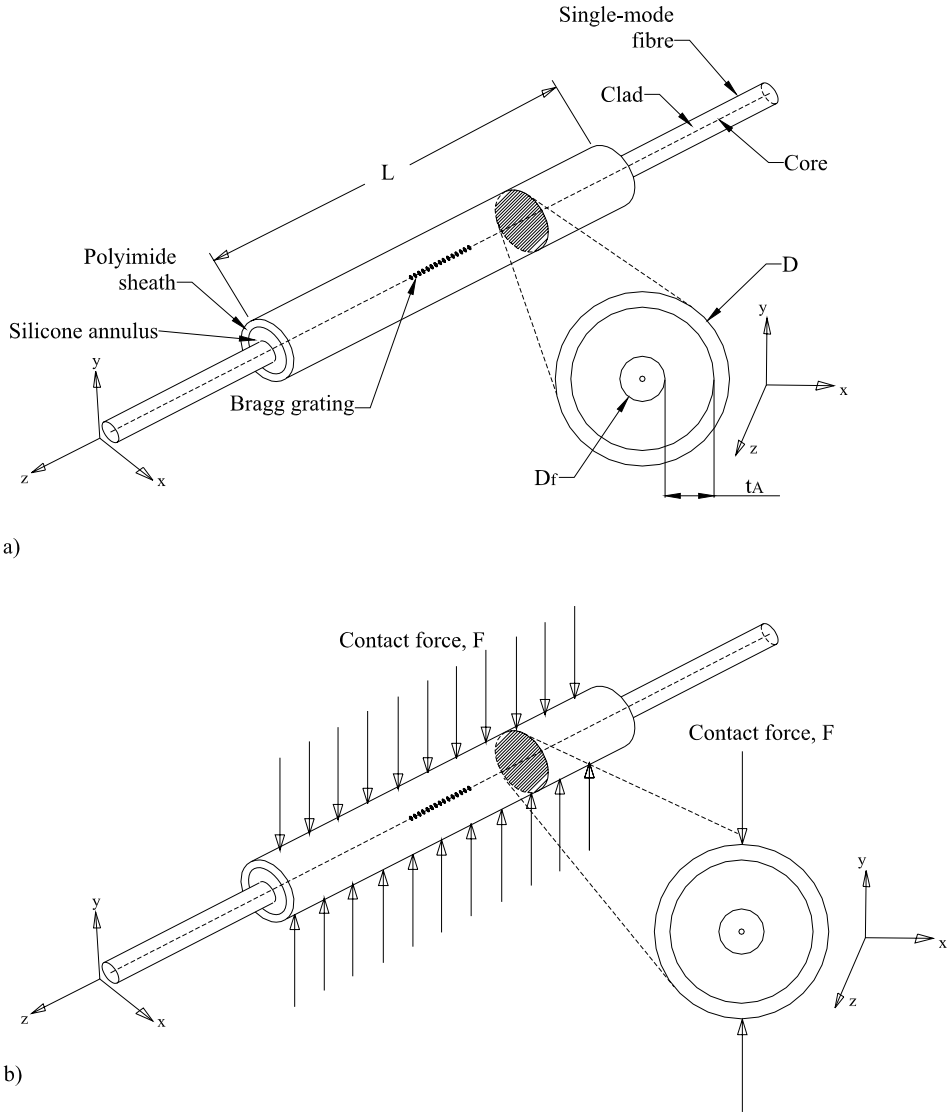

Figure B-2: a) schematic showing relevant features of contact force/stress sensor. The inset cross section shows relevant cross sectional details. b) schematic showing contact force sensor subjected to a uniformly distributed contact force, F.

Two prototype contact force sensors were constructed in this work (last column of Table B-1, prototypes A and E). Both prototypes were constructed with 1 mm long Bragg gratings (Micron Optics, Atlanta GA, nominal full-width at half maximum 1.2 nm, nominal peak reflectivity 56%) photo-inscribed in a conventional single-mode fibre (D_f =

125 μm). The dimensions of prototype A and E are summarized in Table B-1. Fibre diameter was reduced using hydrofluoric acid wet-etching techniques developed for previous work [48]. The length, L, of both prototypes is 15 mm. The rationale underlying the choices of prototype dimensions will be expanded upon in the results and discussion.

Table B-1: Fibre diameter, D_f; annulus thickness, t_A; and sheath inside diameter and outside diameter, D for finite element models (design references A through L) and prototype sensors (prototype references A and E).

				Sheath dimensions		
Design reference	Varied dimension	Fibre diameter, D_f	Annulus thickness, t_A	Inside diameter	Outside diameter, D	Prototype reference
A		125	37.5	200	240	Prototype A
B		100	50	200	240	n/a
C		90	55	200	240	n/a
D	D_f	80	60	200	240	n/a
E		70	65	200	240	Prototype E
F		60	70	200	240	n/a
G		40	80	200	240	n/a
H		125	67.5	260	300	n/a
I		125	47.5	220	260	n/a
J	t_A	125	27.5	180	220	n/a
K		125	17.5	160	200	n/a
L		125	7.5	140	180	n/a
M	n/a	125	57.5	n/a*	n/a*	n/a

All dimensions in μm
*Design M was modeled without the Polyimide™ sheath

3.3 Finite-element and strain-optic modeling

Structural finite-element and strain-optic modeling were used to calculate contact force-induced strains and contact force-induced Bragg wavelength shifts, respectively, to understand sensor performance and modulus dependence of sensitivity. Contact force-induced strains in the sensor were calculated using a commercially available finite element code (ANSYS® version 11, Canonsburg PA). The finite-element-predicted

strains at the fibre core were then used to predict contact force-induced Bragg wavelength shifts through Equation B-2.

The finite-element model consists of one quadrant of the sensor cross section (Figure B-3a). Contact forces, F, are applied by contacting bodies (*e.g.* steel in Figure B-3a, or cartilage) above and below the sensor. These contact forces cause the contacting material to displace and contact the sensor, as shown in Figure B-3b. Displacement boundary conditions are based on symmetry of the sensor cross section about the x- and y-axes, and are imposed on the contacting material and sensor, as shown in Figure B-4a. Z-displacements, Uz, are obtained from the two-dimensional model shown in Figure B-3 by prescribing *generalized plane strain* element behavior.

The Polyimide™ and silica glass are modeled using PLANE183 (tetrahedron) elements [49] and linear elastic isotropic material properties. The Young's modulus and Poisson ratio of the Polyimide™ and optical fibre are 3 GPa and 0.34 [50, 51]; and 70 GPa and 0.17 [38], respectively.

To model the non-linear isotropic stress-strain behavior of the polymer annulus that results from finite deformations, non-linear hyper-elastic PLANE 183 elements are used with a two-point Mooney-Rivlin strain-energy function. The Mooney-Rivlin material constants [52] are estimated, based on prior sensor modeling work [53], to be C_{10} = 200 kPa and C_{01} = 100 kPa.

Both linear and non-linear elastic models of the contacting material were applied. In the linear model, the modulus ranged from 10 MPa (i.e., within the range of published linear elastic properties of cartilage) to 200 GPa (i.e. the modulus of steel). In the non-linear model, the Mooney-Rivlin parameters C_{10} and C_{01} ranged from 0.3 MPa to 4 MPa

and from 0.1 MPa to 1.33 MPa, respectively, while Poisson ratio remained constant at 0.106. This use of a linear model for relatively low strain cases and a non-linear model for high strain cases is, as discussed in Section 2, consistent with the methods of previous studies.

The target surface of the contacting material (Figure B-3a) is meshed with TARGE169 elements, and the contact surface of the sensor is meshed with CONTA175 elements. To satisfy convergence and mesh-shape quality requirements [54] a nominal global element size of 1.5 μm is used (Figure B-3b). The effect, on strain magnitudes, of element shape was tested by replacing tetrahedron elements with triangular elements and found to be negligible. The contacting material has width (along the x-axis) of 120 μm and depth (along y-axis) of 80 μm.

Sensor modeling began by assessing the effect on sensitivity of encapsulating the polymer annulus with the Polyimide™ sheath. Strains were obtained from the finite-element model, for contact forcess ranging from 0 N/mm to 1.7 N/mm, for designs with and without the Polyimide™ sheath (design A and M, respectively). Throughout this work, contact force is expressed as force per unit of sensor length.

Next, the effects of changing values of the sensor dimensions D_f and t_A on contact force-induced strains in the fibre core were assessed. The ranges of sensor dimensions are summarized in Table B-1 (design references A through L). Strains were obtained for a single contact force, 0.17 N/mm, for all values of the sensor dimensions. The effect on sensor sensitivity was determined from the relative changes in contact-force-induced wavelength shift, obtained using the strains, as the sensor dimensions were varied.

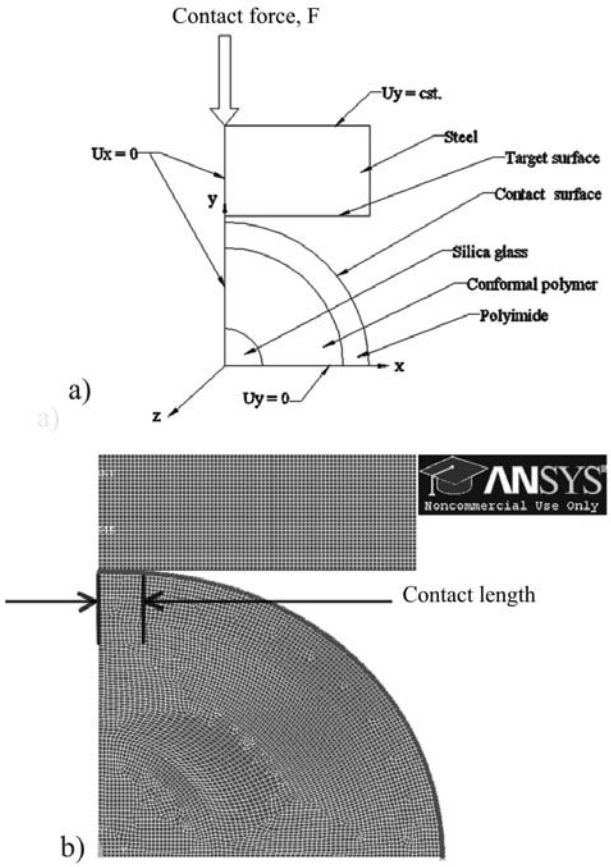

Figure B-3: a) schematic showing relevant features, boundary conditions, materials and forces of finite-element model. b) digital image showing contact between target and contact surface of meshed model, for 0.68 N/mm.

Finally, the dependence of sensor sensitivity on the elastic properties of the contacting material was modeled. This was accomplished by varying the linear Young's modulus over the range stated above. Strains in the fibre core were obtained for a single force (0.17 N/mm) while Young's modulus was varied. The strains were used to calculate Bragg wavelength shifts (Equation B-2). This process was completed for the following sensor designs: design M (without the Polyimide™ sheath); design A (with the sheath); and design E. The effect of Poisson ratio of the contacting material was also assessed by

completing this process for Poisson ratio of 0.3 (typical of metals) and 0.106 (typical of cartilage).

To study the dependence of sensor sensitivity on cartilage elastic properties that fall below the Young's modulus of 10 MPa, strains in the fibre core were obtained for the range of Mooney-Rivlin parameters, C_{10} and C_{01}, stated above. Strains were obtained for design E.

3.4 Sensor calibration

Sensor calibration experiments were comprised of three stages. In stage 1, the sensors were subjected to contact forces applied by steel metrology gauge blocks (Figure B-4a). The objective of stage 1 was to verify the finite-element model predictions of sensor sensitivity. In stage 2, the calibrations were repeated; however, contact forces were applied through a compliant material with Young's modulus in the range typical of cartilage (Figure B-4b). The objective of stage 2 was to test the finite-element predictions of dependence of sensitivity on modulus. In stage 3, the calibrations were repeated for various inclinations of the sensor x-axis, relative to gauge block surfaces, of the sensor (Figure B-4c). The objective of stage 3 was to assess the sensitivity of the sensor to orientation.

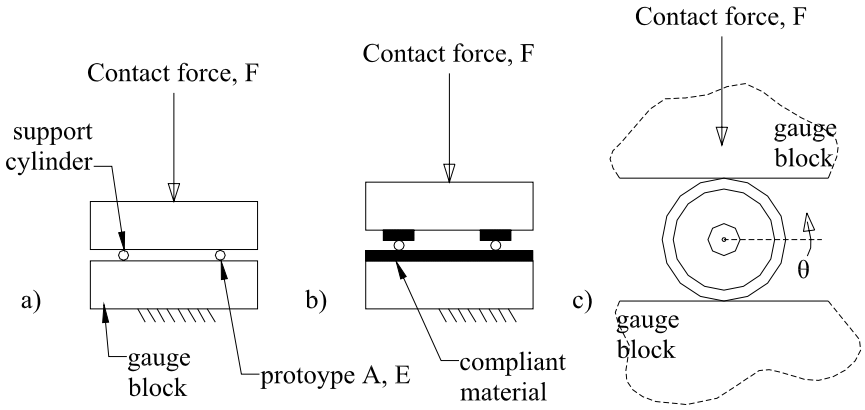

Figure B-4: a) schematic of loading configuration for stage 1. b) schematic of loading configuration for stage 2 where a compliant material contacted the sensor. c) schematic of sensor between gauge blocks showing inclination angle about fibre longitudinal axis.

The apparatus used for the three calibration stages was identical to that used in a previous study (*i.e.* Dennison *et al.* (2010) [55]). The key features and function of the calibration apparatus are summarized here. The prototype sensors and a support cylinder of identical construction (without a Bragg grating), were subjected to contact force between two metrology gauge blocks (Class 0, 24.1 mm by 24.1 mm, steel, Mitutoyo Can., Toronto ON). The bottom gauge block supported the optical fibres and the top block applied contact forces. Both gauge blocks were constrained by guide blocks allowing motion only in the direction of load application. This prevented relative motions that can cause fibre twisting and non-repeatable results [29].

Contact forces were applied by compressing a calibrated spring with a manual screw-follower (not shown). These forces were transmitted through a pre-calibrated load cell (445 N capacity, ± 0.1 %FS non-repeatability, Futek Inc., Irvine CA), fixed to the top gauge block, connected to a data-acquisition system implemented in LabView™ (version 8, National Instruments Inc., Austin TX). The force was transmitted through the top gauge block, through the sensor and support cylinder, and finally to the bottom gauge

block. The compliant material (Figure B-4b) has linear Young's modulus in the range of values typical of cartilage (Viton®, durometer 75A, Young's modulus range 5.0 – 10.0 MPa [56]). The nominal dimensions of the compliant material that applied forces are: 2.5 mm width, 24 mm length and 2 mm thickness. Angular orientation (Figure B-4c) of the sensor, $\theta = 0^{\circ}$, $45^{\circ}$and 135°, was manually controlled with a purpose-built fibre rotator. Applied contact forces in all calibrations ranged from 0 N/mm to, nominally, 1.0 N/mm. This range of forces was chosen because it brackets the range of forces experienced in the hip during walking [57]. Bragg wavelength shifts were measured using an optical spectrum analyzer (ANDO AQ6331, Tokyo JP) as described below. In stages 1, 2 and 3 the calibration experiments were repeated three, two and three times, respectively. Sensor sensitivity was determined as the slope of the best-fit straight line of the wavelength shift versus applied force data and was calculated using linear regression. Sensor calibrations were not performed using materials with modulus below that of Viton®, or with Mooney-Rivlin parameters in the range stated for cartilage.

Bragg wavelength variations were demodulated by directing un-polarized light from a broad C-band light source (AFC-BBS1550, Milpitas, CA) into one of the input channels of a 3 dB optical coupler (Blue Road Research, Gresham OR). The light was then directed *via* the coupler to the FBG in the sensor. The reflected spectrum was directed back through the optical coupler and into the optical spectrum analyzer. This demodulation method and experimental configuration has been presented in previous literature [43, 58].

3.5 Contact force and pressure measurements in cadaveric hips

Two cadaveric hip specimens were obtained (1: Female, 45 yrs., right hip, 2: Female, 73 yrs., left hip). Each specimen was dissected of all musculature, but the joint capsule was left intact (Figure B-5a). The femur was potted in dental cement to simulate single-leg stance (Figure B-5a) and the pelvis was cut at the level of the anterior inferior iliac spine to create a flat surface to which compressive loads were applied.

To allow simultaneous measurements of hydrostatic pressure and contact force, both prototype E and a Bragg grating based hydrostatic pressure sensor (400 μm diameter) [59] were implanted into the joint (Figure 5a and 5b). The pressure sensor was inserted through the joint capsule near the acetabular ligament and into the joint space such that its active sensing area was positioned in the fossa (Figure B-5b). The FBG pressure sensor was pre-calibrated over a range from 0 MPa to 1 MPa using methods and apparatii consistent with our previous work [48, 53]. As stated in Section 2, hydrostatic pressure measurements within the fossa have been used to measure synovial fluid pressure within the joint space [25].

The FBG contact sensor was inserted into the joint space and positioned between the cartilage surfaces of the acetabulum and femoral head (Figure B-5b). Access to the joint space was gained by first piercing the fibrous joint capsule (Figure B-5b) using a 0.4 mm diameter hypodermic needle. The needle was then withdrawn, and the sensor was advanced into the capsule through the small hole left by the needle. To advance the sensor past the labrum (Figure B-5b) a gap was created between the femoral head and labrum by manually applying a force that separated the femoral head from the acetabulum. The sensor was advanced under the labrum and positioned into the joint

space as shown in Figure B-5b, in the region of the acetabular dome. The separating force was then removed, allowing the joint to return to its natural position.

For the *ex vivo* experiments in the hip, the contact force and hydrostatic pressure measurements were conducted using a high-speed Bragg grating interrogator (Micron Optics sm130). The high-speed interrogator was used because it has increased bandwidth (1 kHz) relative to the optical spectrum analyzer (1 Hz). Because different interrogation equipment was used, sensor calibrations were repeated prior to experiments in the hip. Bragg wavelength shifts of both FBG sensors were acquired at 10 Hz using the high-speed interrogator and hardware and software implemented in LabView (Version 8, Austin TX).

Compressive loads were applied to the hip specimens (Figure B-5a) using methods consistent with previous studies [25]. Each specimen was fixtured to a materials testing machine (Instron 8874, Norwood MA) to simulate single-leg standing. During the simultaneous pressure and contact force measurements, compressive loads were measured at 10 Hz using an integrated load cell (Sensor Data M211-113, Sterling Heights MI, Acc.: 0.05% FS-10 kN) using hardware and software implanted in LabView.

Specimens were pre-conditioned by applying compressive loads from 0 N to 300 N and back to 0 N at 10 N/s with the materials testing machine, three times. Following pre-conditioning, the simultaneous pressure and contact force measurement experiments were conducted. Compressive loads were applied ranging, nominally, from 0 N to 300 N, at 10 N/s (approximately 50 % of the donor bodyweight) while hydrostatic pressure and contact force were measured. This was repeated five times in each specimen. During all experiments, the FBG sensors were visually monitored to ensure that there were no

obvious displacements that would indicate motion of the sensing locations within the joint. The optical patch-chords of both sensors were secured to the Instron base, to limit extraneous loads that could cause motion of the FBG sensors.

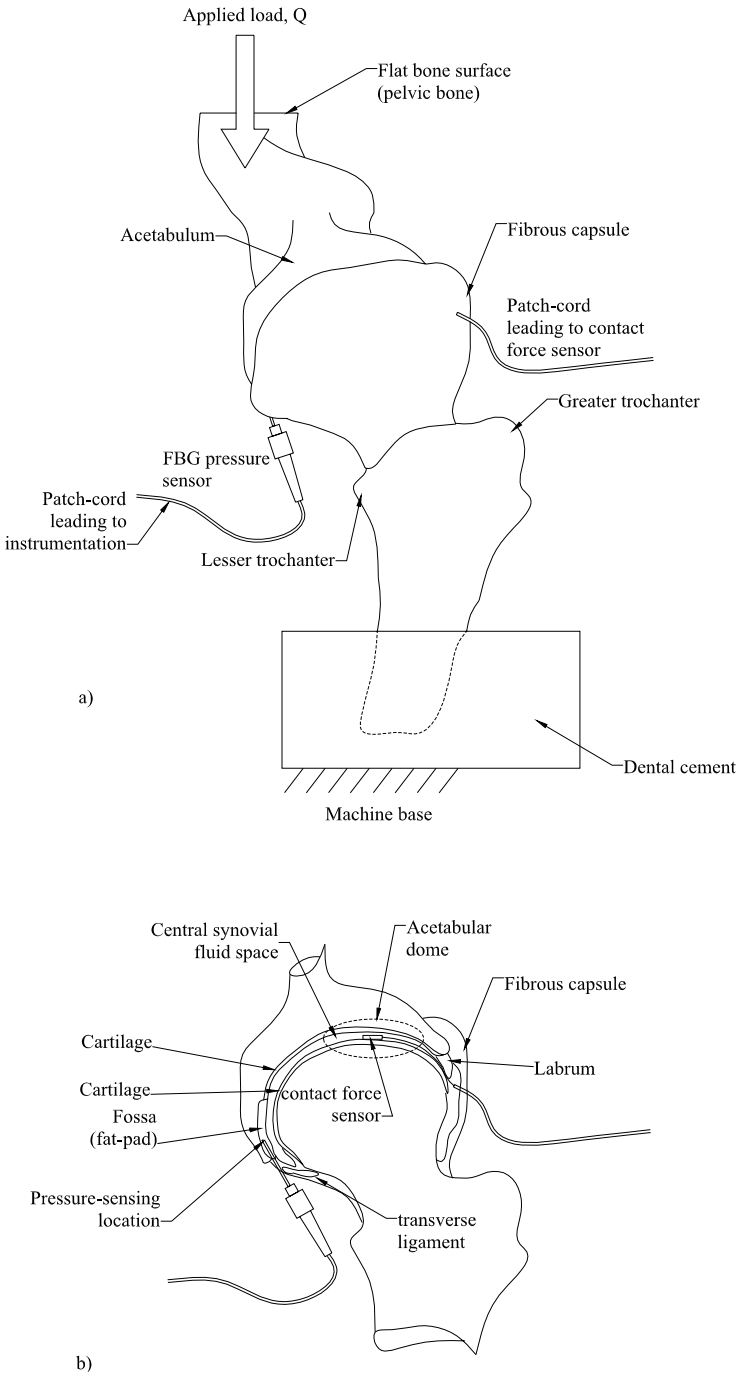

Figure B-5: a) schematic representation of hip joint with femur encapsulated in dental cement. Loads were applied with the joint positioned to simulate single-leg stance. FBG pressure and contact load sensor insertion locations are also shown. b) detailed cross-

sectional schematic (not to scale) of hip showing sensor insertion and locations of sensing locations.

4. Results

4.1 Finite-element and strain-optic modeling

Figure B-6 shows the model-predicted sensitivities of design A (with sheath) and design M (without the Polyimide™ sheath). As shown by the regression-calculated sensitivities (*i.e.* slopes of data), the Polyimide™ sheath increases sensitivity relative to an un-sheathed sensor of the same diameter. The sensitivity of design A is 47% higher than that of the un-sheathed sensor. The calculated wavelength shifts for increasing applied forces (Figure B-6) exhibit linearity over the range of modeled loads.

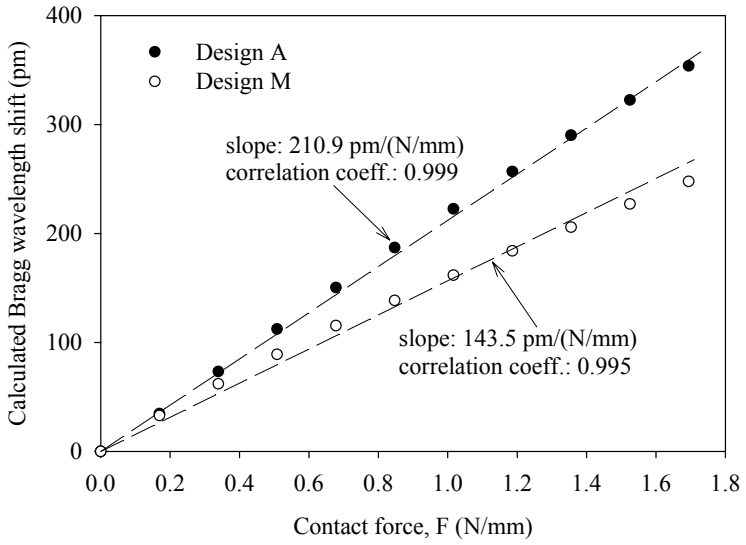

Figure B-6: model-predicted Bragg wavelength shifts plotted versus contact force, F, for design A and design M. Dashed lines are linear-regression calculated best fit lines with slopes as noted in the plot area.

Relative changes in model-predicted Bragg wavelength shifts associated with changes in D_f and t_A are plotted in Figure B-7. The wavelength shift changes are relative to design A, at a contact force of 0.17 N/mm.

The model predictions indicate that reduction of fibre diameter, D_f, causes large increases in Bragg wavelength shift, relative to changes in the size of the annulus

thickness, t_A. As shown, reducing D_f from 125 μm to 40 μm increases Bragg wavelength shifts by approximately 850%, relative to design A. Increasing t_A from 37.5 μm to 67.5 μm causes increases of approximately 64%. Decreasing t_A from 37.5 μm to 7.5 μm causes decreases of approximately 37%. Based on the model predictions, the sensitivity of design E (or prototype E) is expected to be approximately 274 % greater than that of design A (or prototype A).

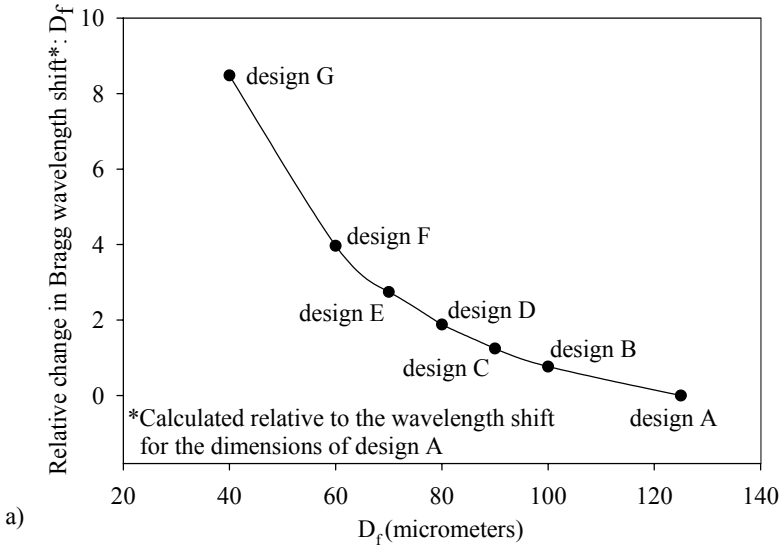

a)

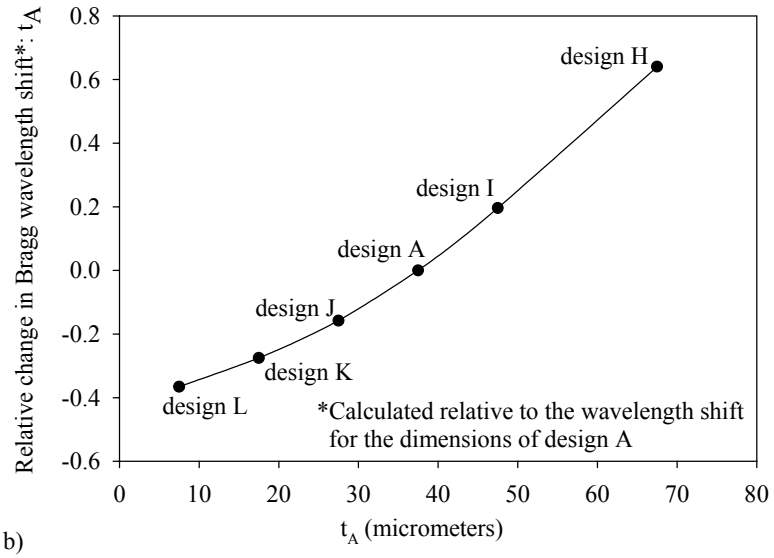

b)

Figure B-7: a) relative changes in Bragg wavelength shift versus D_f at a contact force of 0.17 N/mm. b) relative changes in Bragg wavelength shift versus t_A at a contact force of 0.17 N/mm.

Figure B-8 shows relative changes in Bragg wavelength shift, for a contact force of 0.17 N/mm, versus Young's modulus of the contacting material ranging from E = 10 MPa to E = 200 GPa. The changes in wavelength shift are calculated using the wavelength shift at E = 200 GPa as a reference value.

The modulus range modeled for design M was 50 MPa to 200 GPa. Relative changes in wavelength shift increase as modulus magnitude decreases. At 50 MPa, the maximum relative change in wavelength shift is 3.4 %.

The wavelength shift increases for all prototypes that have polyimide sheaths are lower than those of design M. For the range of linear modulus values of cartilage plotted in Figure B-8, the modulus dependent relative changes in wavelength shift are all less than 8 %. For all designs modeled, Bragg wavelength shifts, for the given contact load (*i.e.* 0.17 N/mm), increase as Young's modulus decreases (Figure 8). Maximum changes in wavelength shift for design A are 7% and 4% (at E = 10 MPa) for Poisson ratio (of the contacting material) of 0.3 and 0.106 (for the contacting material), respectively. Wavelength shifts for design E have the least change, considering all designs modeled, with maximum relative changes of 5% and 2% (at E = 10 MPa) for Poisson ratio of 0.3 and 0.106 (for the contacting material), respectively.

Figure B-9 shows relative changes in Bragg wavelength shift for Young's modulus below 10 MPa, obtained from the finite-element/strain-optic model with cartilage properties modeled using the Mooney-Rivlin formulation (as described in Section 3.3). The changes in wavelength shift are calculated using the wavelength shift at C_{10} = 4.0 MPa and C_{01} = 1.3 MPa, as a reference. As shown, relative wavelength shifts

monotonically increase as C_{10} and C_{01} decrease. The maximum relative change is 7 % at C_{10} = 0.30 MPa and C_{01} = 0.10 MPa.

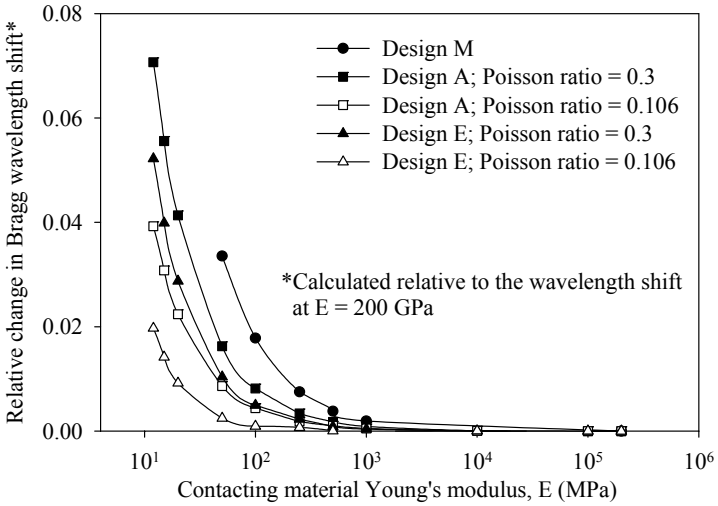

Figure B-8: relative changes in Bragg wavelength shift plotted versus the linear Young's modulus of the contacting material for 0.17 N/mm contact force.

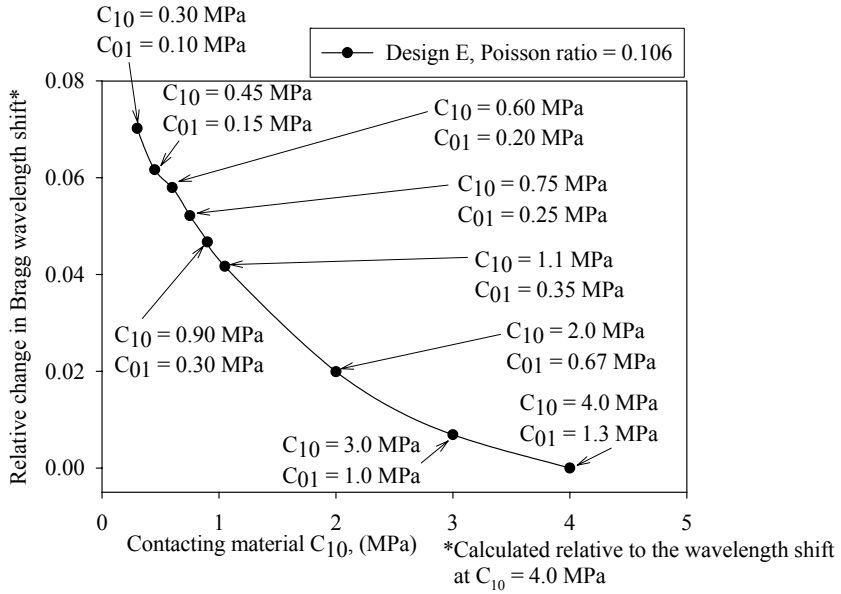

Figure B-9: relative changes in wavelength shift plotted versus Mooney-Rivlin parameters of the contacting material (cartilage) for 0.17 N/mm contact force.

4.2 Sensor calibrations

Results of calibrations of prototype A and E are summarized in Table A-2. Figure B-10 shows typical calibration data obtained for prototype A. The mean regression calculated sensitivity of prototype A, when calibrated using steel gauge blocks, is 209.1 pm/(N/mm), which is only 0.9 % lower than the finite-element/strain-optic model predicted sensitivity for design A (*i.e.* 210.9 pm/(N/mm)). The mean sensitivity of prototype A, when calibrated using Viton®, is 229.1 pm/(N/mm), which is only 9.5 % higher than the sensitivity found using steel gauge blocks (209.1 pm/(N/mm)). This 9.5 % increase in sensitivity is in close agreement with the finite-element/strain-optic model predicted increase in sensitivity for design A, for a material with modulus of Viton® (*i.e.* 7% in Figure B-8). The mean sensitivity for the three angular rotations of prototype A is 207.7 pm/(N/mm). All calibration data sets exhibited linearity (Figure B-10 and Table B-2); the minimum correlation coefficient for prototype A data is 0.990.

Figure B-11 shows typical calibration data obtained for prototype E. The mean sensitivity of prototype E, when calibrated using steel gauge blocks, is 557.5 pm/(N/mm), which is 265 % greater than the sensitivity of prototype A (*i.e.* 210.5 pm/(N/mm)). This 265 % increase in sensitivity is also in close agreement with the finite-element/strain-optic model predicted increase in sensitivity for design E, which was 274 % (Figure B-7).

The mean sensitivity of prototype E, when calibrated using Viton®, is 583.2 pm/(N/mm), which is only 4.6 % higher than the sensitivity found using steel gauge blocks (557.5 pm/(N/mm)). This 4.6 % increase in sensitivity is in close agreement with the finite-element/strain-optic model predicted increase in sensitivity for design E, for a material with modulus of Viton® (*i.e.* 5 % in Figure B-8). The mean sensitivity for the

three angular rotations of prototype E is 561.4 pm/(N/mm). All calibration data sets exhibited linearity (Figure B-11 and Table B-2); the minimum correlation coefficient for prototype E data is 0.983.

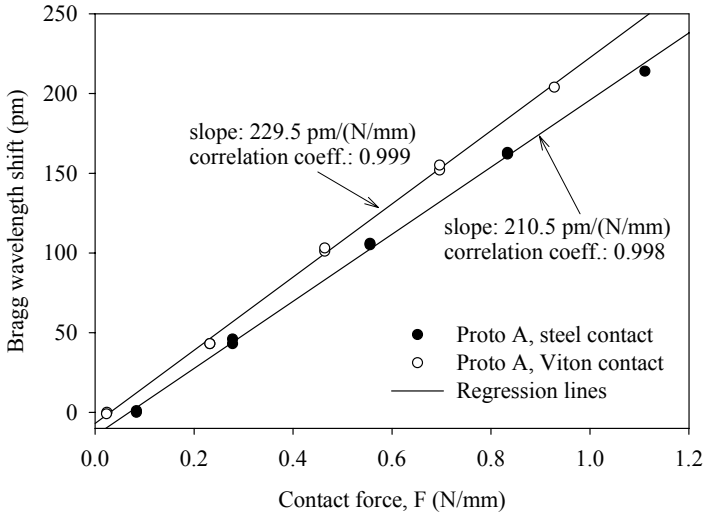

Figure B-10: calibration data for prototype A from stage 1, trial 1 and stage 2, trial 1. Solid lines represent regression-calculated slopes. Error bars (± 5 pm) not shown but are based on published reproducibility of the optical spectrum analyzer.

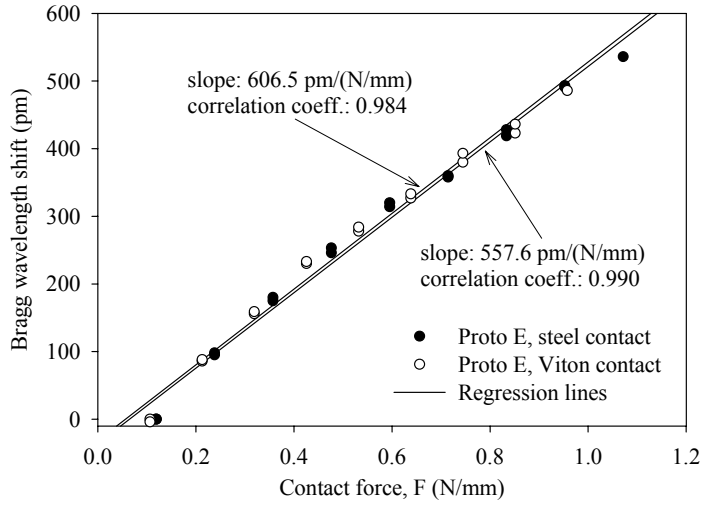

Figure B-11: calibration data for prototype E from stage 1, trial 2 and stage 2, trial 2. Solid lines represent regression-calculated slopes. Error bars (± 5 pm) not shown but are based on published reproducibility of the optical spectrum analyzer.

Table B-2: Regression-calculated sensor sensitivities and correlation coefficients of both prototypes A and E. Stage refers to calibration stages defined in section 3.4.

Prototype	Stage		Sensitivity (pm/(N/mm))	Correlation coeff. (r^2)
A	1	trial 1	210.5	0.998
		trial 2	207.8	0.997
		trial 3	209.1	0.998
		mean	209.1	0.998
	2	trial 1	229.5	0.999
		trial 2	228.7	0.997
		mean	229.1	0.998
	3	$\theta = 0^{\circ}$	210.5	0.998
		$\theta = 45^{\circ}$	201.3	0.990
		$\theta = 135^{\circ}$	211.4	0.982
		mean	207.7	0.990
E	1	trial 1	568.5	0.983
		trial 2	557.6	0.990
		trial 3	546.5	0.983
		mean	557.5	0.985
	2	trial 1	559.8	0.987
		trial 2	606.5	0.984
		mean	583.2	0.986
	3	$\theta = 0^{\circ}$	568.5	0.983
		$\theta = 45^{\circ}$	555.4	0.989
		$\theta = 135^{\circ}$	560.2	0.991
		mean	561.4	0.988

4.3 Contact force and pressure measurements in cadaveric hips

FBG sensor-based contact force and hydrostatic pressure measurements in the cadaveric hips are summarized in Table B-3. Figure B-12a shows a typical load versus time profile as measured by the load cell integrated with the materials testing machine. Figure B-12b, shows typical hydrostatic pressure and contact force versus time profiles. As applied loads increase (Figure B-12a), both pressure (left vertical axis, Figure B-12b) and contact force (right vertical axis) monotonically increase. As applied loads vary cyclically

(Figure B-12a, from 40 seconds to 120 seconds), both pressure and contact force also vary cyclically, with the same cyclic frequency as the applied load. As loads decrease (Figure B-12a, after 120s), both pressure and contact force monotonically decrease (Figure B-12b).

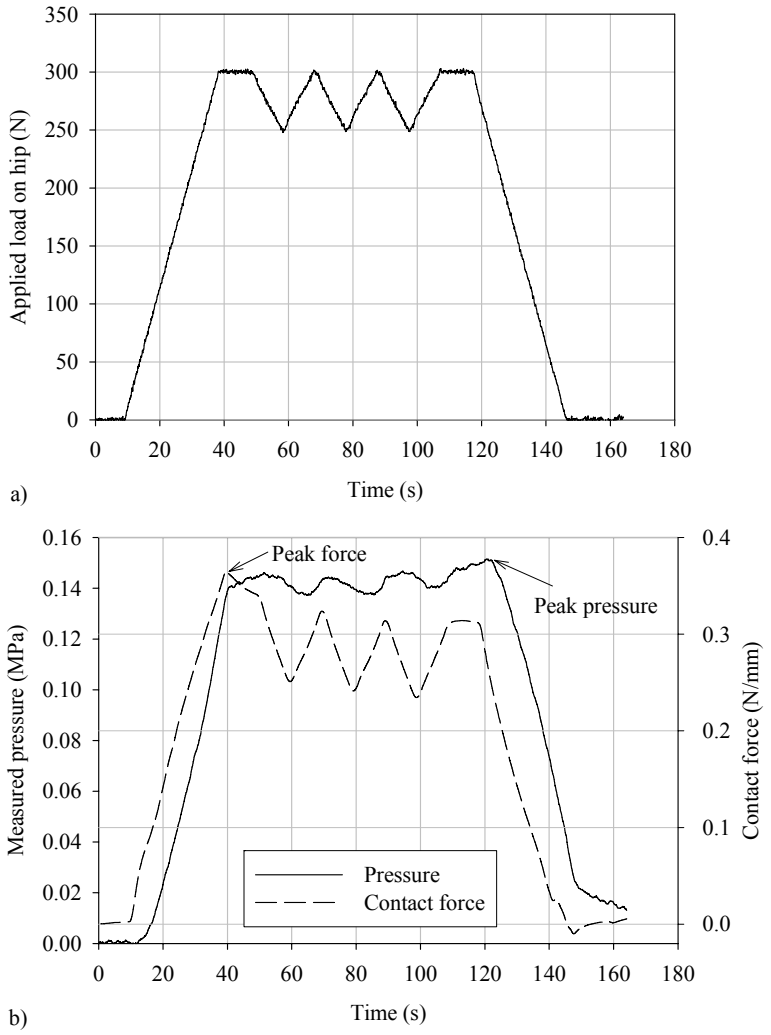

Figure B-12: a) applied load versus time profile as measured by load cell for specimen 2, trial 3. b) FBG-measured pressure and contact force versus time profiles measured during trial 3, for specimen 2. To preserve clarity, data points have been replaced with the line-plots shown, and error bars (± 5 N for applied load, ± 5 kPa for pressure and ± 0.002 N/mm for contact force) have also been omitted.

Peak pressures and contact forces (as shown in Figure B-12b), are listed in Table B-3, for all trials in both specimens. Peak contact stresses are also listed in Table B-3, and

were calculated by dividing the peak contact forces (N/mm) by the diameter of prototype E (*i.e.* 240 μm).

Table B-3: Peak pressures, contact forces and contact stresses measured in cadaveric hip specimens.

Specimen	Trial	Peak pressure† (MPa)	Peak force‡ (N/mm)	Peak stress* (MPa)
1 female, 45 yrs. right hip (weight uknown)	1	0.16	0.050	0.21
	2	0.15	0.042	0.18
	3	0.15	0.037	0.15
	4	0.14	0.032	0.14
	5	0.14	0.032	0.13
	mean	0.15	0.039	0.16
2 female, 73 yrs. left hip (63 kg. donor weight)	1	0.15	0.37	1.5
	2	0.16	0.37	1.6
	3	0.15	0.36	1.5
	4	0.13	0.34	1.4
	5	0.15	0.35	1.5
	mean	0.15	0.36	1.5

†measured with FBG pressure sensor
‡measured with prototype E contact force sensor
*calculated as peak force divided by prototype E sensor diameter (*i.e.* 240 μm)

5. Discussion

The finite-element/strain-optic modeling indicates two benefits to sensor sensitivity directly attributable to the presence of the Polyimide™ sheath: first, increased sensitivity relative to an un-sheathed sensor of the same diameter (Figure B-7); and second, lower modulus dependence of sensitivity, relative to an un-sheathed sensor (Figure B-9). Insights gained from the finite-element model can be used to elucidate the causes of these benefits.

The Polyimide™ sheath increases sensor sensitivity, relative to an un-sheathed sensor of the same diameter, because it encapsulates the incompressible polymer annulus (Figure B-2). Because the annulus is encapsulated, x-strains in the polymer are limited compared to those of the un-sheathed sensor. Because x-strains in the polymer are

limited, and the polymer is incompressible, z-strains increase to conserve the volume of the annulus. Increased z-strains in the polymer lead to increased z-strains in the optical fibre, which leads to increased sensor sensitivity (Equation 2).

Limiting x-strains also reduces dependence of sensitivity on Young's modulus of the contacting materials. The main cause of modulus dependent sensitivity is changes in the contact length (Figure B-3b) between the sensor and contacting material [47], which affect the strains induced in the fibre core, and therefore sensor sensitivity. Changes in contact length are related to the contact-induced strains and deformations of the contacting material and sensor. These strains and deformations depend on the modulii of the contacting materials. For example, contacts between metals, that have relatively high modulii, result in small strains and deformations in the region of contact and, therefore, small contact lengths. Conversely, if a metal contacts a low-modulus polymer, the strains and deformations in the polymer will be large, which lead to large contact lengths. Following this logic and applying it to the contact sensor, if strains in the contact region are limited, modulus dependence of sensitivity should also be limited.

Considering an un-sheathed sensor, x-strains are not limited and, therefore, result in large deflections in the polymer and large contact lengths. Conversely, the Polyimide™ sheath limits x-strains and, therefore, the circular shape of the sensor is more preserved, relative to the un-sheathed sensor. Therefore, the sheathed sensors experience less change in contact length because the sheath limits deflections in the polymer. Because the sheathed sensors experience less change in contact length, they experience less modulus dependence of sensitivity (Figure B-8 and B-9).

The finite-element model also predicts that the greatest increases in sensor sensitivity are achieved by reducing fibre diameter, D_f (Figure B-7). Because D_f is reduced and overall sensor diameter is maintained, the polymer annulus comprises a larger proportion of the sensor cross-sectional area. Because a larger area is comprised of the low-modulus polymer, the effective stiffness of the sensor cross section is reduced which, when contact forces are applied, leads to increased z-strains in the polymer. The increased z-strains are transmitted to the fibre, which increases sensor sensitivity. Conversely, increases in annulus thickness, t_A, do not result in significant increases in sensitivity (Figure B-7) principally because increases in annulus thickness cause increases in sensor diameter. With increased diameter, more material supports the contact force, which reduces strains in the polymer; thereby reducing the potential gain in sensitivity associated with increasing the proportion of sensor area comprised by polymer.

The experimental results confirm the importance of the Polyimide™ sheath and reductions in fibre diameter, D_f. The prototype E sensor has both increased sensitivity (557.5 pm/(N/mm)) and reduced modulus dependence of sensitivity, while maintaining small size (major diameter of only 240 μm). This is an improvement over polymer jacketed sensors presented in the literature that achieve sensitivities of approximately 300 pm/(N/mm) with extremely large diameters (4 mm) [46]. In the context of application to joints, 4 mm diameter sensors are too large to be implanted in joints spaces. The chosen dimensions of prototype E result in increased sensitivity and a major sensor diameter (240 μm) that fits between the cartilage surfaces of the hip.

The results of the sensor calibrations are in close agreement with the predictions of the finite-element/strain-optic model. One limitation of this work is that calibrations were

not performed for contacting materials with known Mooney-Rivlin constants corresponding to cartilage. Both prototypes demonstrated orientation independence of sensitivity (Table B-2).

The predictions of low modulus dependence of sensitivity are promising when compared to the results of studies of Fuji Prescale. Wu *et al.* (1998) conducted a numerical study of measurement errors of Prescale applied to simulated joints [19]. The key finding was that stress measurements from Prescale could contain errors ranging from 14 % to 28 %. These errors were a function of contact force magnitude, Prescale film thickness and stiffness, cartilage material properties and joint surface curvature. However, the study indicated that the Prescale film compressive modulus (100 MPa) and thickness (300 μm) were the primary causes of measurement errors. The study indicated cartilage modulus dependent stress measurement errors as high as 6 % for a cartilage modulus range from 0.3 MPa to 0.6 MPa. To mitigate these errors, Wu *et al.* (1998) suggest development of sensors with lower compressive modulus and thickness. Prototype E of the current work is only 240 μm in diameter, with potential to be smaller, and is comprised of a low modulus polymer. The finite element model-predicted change in sensitivity for prototype E is 7% for relatively large ranges in Mooney-Rivlin parameters, C_{10} and C_{01}, of 0.3 MPa to 4.0 MPa and 0.10 MPa to 1.3 MPa, respectively (Figure B-9). One limitation of the finite element modeling in this work is that changes in sensor sensitivity were not calculated as a function of joint surface curvature. Quantifying these changes, and modifying the sensor design to minimize them, is an important aspect of sensor development and validation that will be the focus of future work.

There were significant differences in the pressure results from this work and those of previous studies. For example, Ferguson *et al.* (2003) [25] measured peak pressures in the acetabular fossa in hips with both intact and excised (*i.e.* removed) labra. Pressures were approximately 0.55 MPa and 0.20 MPa for loads of 75 % of the donor body-weight, applied over 10 s, for intact and excised labra, respectively. In this work, peak pressures were 0.15 MPa for loads of 50 % of the donor body-weight, applied over 30 s, in specimens with visually intact labra. Factors contributing to differing pressure magnitudes could include differences in load application rate and differences in the labrum condition between the specimens used in this work and those used by Ferguson *et al.* (2003). Previous investigations have indicated that in a loaded hip, over time, both synovial fluid pressure and contact stress decrease in magnitude due to joint consolidation processes [24]. Moreover, experimental investigations have shown that peak synovial fluid pressures are lower in hips with excised (*i.e.* removed) labra [25].

The relative magnitudes of contact force/stress between specimen 1 and 2 were found to be qualitatively consistent with observations of previous researchers [60]. Maximum contact forces/stresses in specimen 1 were lower than those in specimen 2, which suggests increased contact in the region of the acetabular dome for specimen 2, which was from an older donor, than specimen 1. These initial results are promising and further validation of contact load sensor is ongoing.

The new insertion methods and FBG-based sensors allowed the first simultaneous measurements of pressure and contact load/stress within cadaveric hip joints.

6. Conclusions

In this work, the design of a new, FBG-based, contact force sensor is presented. This sensor has increased sensitivity to contact force, relative to other FBG-based contact force sensors presented in the literature, while maintaining extremely small size. The FBG sensor also addresses two limitations associated with *stress sensitive films* which are the current standard for stress measurements in articular joints. First, the FBG sensors can be implanted without dissection and disarticulation of biomechanically relevant structures that surround the joint, unlike film-based sensors. Second, the FBG sensors have low modulus dependence of sensitivity. Modulus dependence of sensitivity associated with stress sensitive films can lead to significant stress measurement errors because the modulus of cartilage can range from 0.5 MPa to 20 MPa.

To the authors' knowledge, the results of this study are the first simultaneous measurements of contact force/stress and pressure within cadaveric hips. After continued validation, these sensors could potentially be applied to study the, currently unknown, relationships between pressure and stress in joints.

References

[1] Komistek, R. D., Kane, T. R., Mahfouz, M., Ochoa, J. A., and Dennis, D. A., 2005, "Knee mechanics: a review of past and present techniques to determine in vivo loads," Journal of Biomechanics, 38, pp. 215-228.

[2] Wilson, D. R., McWalter, E. J., and Johnston, J. D., 2008, "The measurement of joint mechanics and their role in osteoarthritis genesis and progression," Rheumatic Disease Clinics of North America, 34, pp. 605-622.

[3] D'Lima, D. D., Steklov, N., Fregly, B. J., Banks, S. A., and Jr., C. W. C., 2008, "In vivo contact stresses during activities of daily living after knee arthroplasty," Journal of Orthopaedic Research, doi: 10.1002/jor.20670.

[4] Varadarajan, K. M., Moynihan, A. L., D'Lima, D., Colwell, C. W., and Li, G., 2008, "In vivo contact kinematics and contact forces of the knee after total knee arthroplasty during dynamics weight-bearing activities," Journal of Biomechanics, 41, pp. 2159-2168.

[5] Hartofilakidis, G., Georgiades, G., and Babis, G. C., 2009, "A comparison of the outcome of cemented all-polyethylene and cementless metal-backed acetabular sockets in primary total hip arthroplasty," The Journal of Arthroplasty, 24(2), pp. 217-225.

[6] Jonkers, I., Sauwen, N., Lenaerts, G., Mulier, M., Perre, G. V. d., and Jaecques, S., 2008, "Relation between subject-specific hip joint loading, stress distribution in the proximal femur and bone mineral density changes after total hip replacement," Journal of Biomechanics, 41, pp. 3405-3413.

[7] Muller, O., Parak, W. J., Wiedemann, M. G., and Martini, F., 2004, "Three-dimensional measurements of the pressure distribution in artificial joints with a capacitive sensor array," Journal of Biomechanics, 37, pp. 1623-1625.

[8] Ong, K. L., Day, J. S., Kurtz, S. M., Field, R. E., and Manley, M. T., 2008, "Role of surgical position on interface stress and initial bone remodeling stimulus around hip resurfacing arthroplasty," The Journal of Arthroplasty, doi:10.1016/j.arth.2008.08.005.

[9] Anderson, A. E., Ellis, B. J., Maas, S. A., Peters, C. L., and Weiss, J. A., 2008, "Validation of finite element predictions of cartilage contact pressure in the human hip joint," Journal of Biomechanical Engineering, 130, p. 10pp.

[10] Herzog, W., Clark, A., and Wu, J., 2003, "Resultant and local loading in models of joint disease," Arthritis and Rheumatology, 49, pp. 239-247.

[11] Ficat, P., 1978, "The syndrome of lateral hyperpressure of the patella," Acta Orthopaedica Belgium, 44, pp. 65-76.

[12] Huberti, H. H., and Hayes, W. C., 1988, "Contact pressure in chondromalacia patellae and the effects of capsular reconstructive procedures," Journal of Orthopaedic Research, 6, pp. 499-508.

[13] Konrath, G. A., Hamel, A. J., Sharkey, N. A., Bay, B., and Olson, S. A., 1998a, "Biomechanical evaluation of a low anterior wall fracture: correlation with the CT subchondral arc.," Journal of Orthopaedic Trauma, 12, pp. 152-158.

[14] Konrath, G. A., Hamel, A. J., Sharkey, N. A., Bay, B., and Olson, S. A., 1998b, "Biomechanical consequences of anterior column fracture of the acetabulum," Journal of Orthopaedic Trauma, 12(547-552).

[15] Drewniak, E. I., Crisco, J. J., Spenciner, D. B., and Fleming, B. C., 2007, "Accuracy of circular contact area measurements with thin-film pressure sensors," Journal of Biomechanics, 40, pp. 2569-2572.

[16] Martinelli, L., Hurschler, C., and Rosenbaum, D., 2006, "Comparison of capacitive versus resistive joint contact stress sensors," Clinical Orthopaedics and Related Research, 447, pp. 214-220.

[17] Bachus, K. N., DeMarco, A. L., Judd, K. T., Horwitz, D. S., and Brodke, D. S., 2006, "Measuring contact area, force, and pressure for bioengineering applications: Using Fuji Film and TekScan systems," Medical Engineering and Physics, 28, pp. 483-488.

[18] Cottrell, J. M., Scholten, P., Wanich, T., Warren, R. F., Wright, T. M., and Maher, S. A., 2008, "A new technique to measure the dynamic contact pressures on the tibial plateau," Journal of Biomechanics, 41, pp. 2324-2329.

[19] Wu, J. Z., Herzog, W., and Epstein, M., 1998, "Effects of inserting a pressensor film into articular joints on the actual contact mechanics," Journal of Biomechanical Engineering, 120(5), pp. 655-659.

[20] Wilson, D. R., Apreleva, M. V., Eichler, M. J., and Harrold, F. R., 2003, "Accuracy and repeatability of a pressure measurement system in the patellofemoral joint," Journal of Biomechanics, 36, pp. 1909-1915.

[21] Brimacombe, J., Wilson, D., Hodgson, A., Ho, K., and Anglin, C., 2009, "Effect of calibration method on Tekscan sensor accuracy " ASME Journal of Biomechanical Engineering, 131(3).

[22] Ferguson, S., Bryant, J., Ganz, R., and Ito, K., 2000, "The acetabular labrum seal: a poroelastic finite element model," Clinical Biomechanics, 15(6), pp. 463-468.

[23] Barker, M. K., and Seedhom, B. B., 2001, "The relationship of the compressive modulus of articular cartilage: does cartilage optimize its modulus so as to minimize the strains arising in it due to the prevalent loading regime?," Rheumatology, 40, pp. 274-284.

[24] Ferguson, S., Bryant, J., Ganz, R., and Ito, K., 2000, "The influence of the acetabular labrum on hip joint cartilage consolidation: a poroelastic finite element model," Journal of Biomechanics, 33(8), pp. 953-960.

[25] Ferguson, S. J., Bryant, J. T., Ganz, R., and Ito, K., 2003, "An in vitro investigation of the acetabular labral seal in hip joint mechanics," Journal of Biomechanics, 36, pp. 171-178.

[26] Geoffrey, A. C., 1998, "Temperature sensor based on a single Bragg grating," C. Brian, and D. C. J. Julian, eds., SPIE, pp. 296-300.

[27] Nelson, D., Makino, A., Lawrence, C., Seim, J., Schulz, W., and Udd, E., 1998, "Determination of the K-Matrix for Multi-parameter Fiber Grating Sensor in AD072 Fibercore Fiber," Proceedings of SPIE, 3489, pp. 79-85.

[28] Chuan, S. T., Jianzhong, H., and Rahul, M., 1998, "Fiber optic pressure sensor using a fiber Bragg grating," E. F. Robert, M. G. Lawrence, E. H. Alson, M. Malachy, and J. S. Warren, eds., SPIE, pp. 123-130.

[29] Chehura, E., Ye, C.-C., Staines, S. E., James, S. W., and Tatam, R. P., 2004, "Characterization of the response of fibre Bragg gratings fabricated in stress and geometrically induced high birefringence fibres to temperature and transverse load," Smart Materials and Structures, 13, pp. 888-895.

[30] Mohanty, L., Tjin, S. C., Lie, D. T. T., Panganiban, S. E. C., and Chow, P. K. H., 2007, "Fiber grating sensor for pressure mapping during total knee arthroplasty," Sensors and Actuators A, 135, pp. 323-328.

[31] Sariali, E., Veysi, V., and Stewart, T., 2008, "Mini-Symposium: Essential biomechanics of hip replacement (i): Biomechanics of the human hip-consequences for total hip replacement " Current Orthopaedics, 22, pp. 371-375.

[32] Kim, J.-E., Zuoping, L., Ito, Y., Huber, C. D., Shih, A. M., Eberhardt, A. W., Yang, K. H., King, A. I., and Soni, B. K., 2009, "Finite element model development of a

child pelvis with optimization-based material identification," Journal of Biomechanics, 42, pp. 2191-2195.

[33] Brown, C., Nguyen, T., Moody, H., Crawford, R., and Oloyede, A., 2009, "Assessment of common hyperelastic constitutive equations for describing normal and osteoarthritic articular cartilage," Proceedings of IMechE Part H: Journal of Engineering in Medicine, 223, pp. 643-652.

[34] Moody, H., 2006, "Benchmarking of the biomechanical characteristics of normal and degraded articular cartilage to facilitate mathematical modeling," Queensland University of Technology, Brisbane.

[35] Zuoping, L., Alonso, J. E., Kim, J.-E., Davidson, J. S., Etheridge, B. S., and Eberhardt, A. W., 2006, "Three-dimensional finite element models of the human pubic symphysis with viscohyperelatic soft tissues," Annals of Biomedical Engineering, 34(9), pp. 1452-1462.

[36] Takechi, H., Nagashima, H., and Ito, S., 1982, "Intra-articular pressure of the hip joint outside and inside the limbus," Journal of Japanese Orthopaedic Association, 56, pp. 529-536.

[37] Hill, K. O., Fujii, Y., Johnson, D. C., and Kawasaki, B. S., 1978, "Photosensitivity in optical fiber waveguides: Application to reflection filter fabrication," Applied Physics Letters, 32(10), pp. 647-649.

[38] Measures, R. M., 2001, Structural Health Monitoring with Fiber Optic Technology, Academic Press.

[39] Meltz, G., Morey, W. W., and Glenn, W. H., 1989, "Formation of Bragg gratings in optical fibers by a transverse holographic method," Optics Letters, 14(15), pp. 823-825.

[40] Huang, S., LeBlanc, M., Ohn, M. M., and Measures, R. M., 1995, "Bragg intragrating structural sensing," Applied Optics, 34(22), pp. 5003-5009.

[41] 2001, "Corning SMF-28 optical fibre: Product Information," Corning Incorporated, Midland MI, www.corning.com/opticalfibre.

[42] Xu, M. G., Geiger, H., and Dakin, J. P., 1996, "Fibre grating pressure sensor with enhanced sensitivity using a glass-bubble housing," Electronics Letters, 32, pp. 128-129.

[43] Xu, M. G., Reekie, L., Chow, Y. T., and Dakin, J. P., 1993, "Optical in-fibre grating high pressure sensor," Electronics Letters, 29, pp. 398-399.

[44] Chen, G., Liu, L., Jia, H., Yu, J., Xu, L., and Wang, W., 2004, "Simultaneous strain and temperature measurements with fiber Bragg grating written in novel hi-bi optical fibre," IEEE Photonics Technology Letters, 16(1), pp. 221-223.

[45] Okamoto, K., Hosaka, T., and Edahiro, T., 1981, "Stress analysis of optical fibers by a finite element method," IEEE Journal of Quantum Electronics, QE-17(10), pp. 2123-2129.

[46] Ngoi, B. K. A., Paul, J., Zhao, L. P., and Fang, Z. P., 2004, "Enhanced lateral pressure tuning of fiber Bragg gratings by polymer packaging," Optics Communications, 242, pp. 425-430.

[47] Paul, J., Ngoi, B. K. A., and Zhao, L. P., 2005, "Enhanced wavelength tuning of laterally loaded FBG strain sensors through optimization of the pressure transmitting system," Sensors and Actuators, A 120, pp. 416-423.

[48] Dennison, C. R., and Wild, P. M., 2008, "Enhanced sensitivity of an in-fibre Bragg grating pressure sensor achieved through fibre diameter reduction," Measurement Science and Technology, 19(125301), p. 11pp.

[49] Ansys Incorporated, , "Ansys structural analysis guide: Release 11, Chapter 1."

[50] Chang, W.-Y., Fang, T.-H., and Liu, Y.-C., 2008, "Physical characteristics of polyimide films for flexible sensors," Applied Physics A, 92, pp. 693-701.

[51] Valavala, P. K., Clancy, T. C., Odegard, G. M., gates, T. S., and Aifantis, E. C., 2009, "Multiscale modeling of polymer materials using a statistics-based micromechanics approach," Acta Materialia, 57, pp. 525-532.

[52] Ansys Incorporated, "Theory and reference for Ansys and Ansys workbench: Release 11."

[53] Dennison, C. R., Wild, P. M., Wilson, D. R., and Cripton, P. A., 2008, "A minimally invasive in-fibre Bragg grating sensor for intervertebral disc pressure measurements," Measurement Science and Technology, 085201, p. 12.

[54] Ansys Incorporated, "ANSYS User's Manual: Chapter 13 - Element Tools," ANSYS Release 10.0, http://www1.ansys.com/customer/content/documentation/80/ansys/thy_et7.html.

[55] Dennison, C. R., and Wild, P. M., 2010, "Sensitivity of Bragg gratings in birefringent optical fibre to transverse compression between conforming materials," Applied Optics, 49(12), pp. 2250-2261.

[56] DuPont Performance Elastomers, 2003, "Viton(R) fluoroelastomer: technical information,"U.S.A.

[57] Hodge, W. A., Fuan, R. S., Carlson, K. L., Burgess, R. G., Harris, W. H., and Mann, R. W., 1986, "Contact pressures in the human hip joint measured in vivo," Proceedings of the National Academy of Sciences USA, 83, pp. 2789-2883.

[58] F M Araujo, L. A. F., J L Santos and F Farahi, 2001, "Temperature and strain insensitive bending measurements with D-type fibre Bragg gratings," Measurement Science and Technology, 12, pp. 829-833.

[59] Dennison, C. R., Wild, P. M., Dvorak, M. F., Wilson, D. R., and Cripton, P. A., 2008, "Validation of a novel minimally invasive intervertebral disc pressure sensor utilizing in-fiber Bragg gratings in a porcine model: an ex vivo study," Spine, 33(17), pp. E589-E594.

[60] Bullough, P., Goodfellow, J., and O'Connor, J., 1973, "The relationship between degenerative changes and load-bearing in the human hip," Journal of Bone and Joint Surgery, 55B(4), pp. 746-758.

Appendix C: A super-structured fibre-optic contact force sensor with minimal co-sensitivity to temperature and axial strain

(Manuscript in preparation)

A super-structured fibre-optic contact force sensor with minimal co-sensitivity to temperature and axial strain

Christopher R. Dennison and Peter M. Wild

Department of Mechanical Engineering, University of Victoria, British Columbia, Canada

Abstract

In this work a new super-structured, FBG-based, contact force sensor is presented that is based on birefringent D-shape optical fibre. The sensor superstructure comprises a polyimide sheath and an alignment feature that repeatably orients the sensor with respect to contact forces. A combination of plane elasticity and strain-optic models are used to predict sensor performance in terms of sensitivity to contact force and axial strain. Model predictions are validated through experimental calibration and indicate contact force, axial strain and temperature sensitivities of 169.6 pm/(N/mm), 0.01 pm/(microstrain) and -1.12 pm/(degree Celsius), in terms of spectral separation. The sensor addresses limitations of existing fibre-based contact force sensors that are based on FBGs in birefringent fibre, FBGs in conventional optical fibre and tilted FBGs. Relative to other birefringent fibre sensors, the sensor has contact force sensitivity comparable to the highest sensitivity of commercially available birefringent fibres and, unlike other birefringent fibre sensors, is self aligning with respect to contact forces. Unlike sensors

based on Bragg gratings in conventional fibre and tilted Bragg gratings, the sensor has negligible co-sensitivity to both axial strain and changes in temperature.

1. Introduction

In-fibre Bragg gratings (FBGs) can be configured as sensors for various parameters including displacement [1], strain [2], temperature [3], pressure [3], contact force [4], humidity [5], and radiation dose [6] among others. FBGs are an attractive alternative to piezoelectric, resistive or other solid-state sensing technologies because they are: small (125 μm diameter and smaller), biocompatible, mechanically compliant, chemically inert, resistant to corrosive environments, immune to electromagnetic interference, and are capable of simultaneous multi-parameter sensing when suitably configured [1, 7-11]. Moreover, multiple FBG sensors can be multiplexed along a single optical fibre thereby allowing spatially distributed measurements [12]. FBG-based contact force sensors typically comprise Bragg gratings in birefringent, polarization-maintaining, optical fibre [4].

Polarization maintaining birefringent fibre (hereafter birefringent fibre) has different refractive indices along two orthogonal, or principal, directions that are commonly referred to as the slow (higher index) and fast (relatively lower index) axes. The difference in the refractive indices along the slow and fast axis is termed the birefringence. A Bragg grating in a birefringent fibre reflects two spectra, one polarized along the fast axis and one along the slow axis, with centre wavelength of each spectrum given by the Bragg condition for reflection [12]. The centre wavelength of each spectrum is a function of, among other parameters, the refractive indices of the fast and slow axes.

In FBG-based contact force sensors, the physical mechanism causing sensitivity to contact force is stress-induced changes in birefringence [13], or, alternatively, refractive index changes of the slow and fast axis, that are governed by the stress-optic effect [14]. Contact forces on the fibre induce stresses (or strains), the principal directions of which are uniform in the region of the fibre core. However, the magnitudes of the principal stresses are a function of the magnitude of the contact force [4]. Therefore, when the contact force magnitude changes, a predictable change in the principal stress magnitudes and, therefore, birefringence is induced. These force-induced changes in birefringence cause predictable changes in the spectrum reflected by the Bragg grating, including shifts in the Bragg spectra corresponding to the fast and slow axes of the fibre. Conversely, applied axial forces/strains and changes in fibre temperature cause relatively lower, in the case of certain fibres insignificant, changes in fibre birefringence [12]. Therefore, FBG sensors in birefringent fibres are less confounded by changes in axial strain and temperature. More specifically, D-shape optical fibre has been shown to experience virtually no change in fibre birefringence with changes in fibre temperature [4] nor changes in axial strain that can result from, among other influences, fibre bending [15].

FBGs in birefringent fibres possess higher sensitivity to contact force than gratings in non-birefringent fibres because they are typically constructed with stress concentrating features embedded in the fibre clad or clad geometries that increase force-induced changes in birefringence [12]. These features are generally referred to as stress-applying parts. Each commercially available birefringent fibre possesses unique stress-applying parts or clad geometry. Therefore, the contact force sensitivity of each type of

birefringent fibre is unique. Contact force sensitivity is also a function of the orientation of the stress-applying parts relative to the direction of load [4]. Therefore, a limitation of birefringence-based contact force sensors is the necessity to control fibre orientation with respect to the contacting surface applying the force.

A number of researchers have studied the relationship between contact force and birefringence for several types of birefringent fibres. Udd *et al.* (1996) [16] used FBGs in 3M, Fujikura and Corning birefringent fibres to simultaneously measure temperature and force-induced axial and transverse strain. Wierzba and Kosmowski (2003) [17] applied Side-Hole birefringent fibre to contact force measurements. Chehura *et al.* (2004) [4] investigated the contact force sensitivity of D-shape, Elliptical core, TruePhase, Panda, Bow Tie and Elliptical clad birefringent fibres as a function of fibre orientation. More recently, Abe *et al.* (2006) [18] measured contact force using chemically-etched Bow Tie and Elliptical clad birefringent fibres to understand the influence that reduction in fibre diameter has on fibre birefringence and contact force sensitivity.

In all of the studies outlined above, fibre orientation relative to the contact force was controlled. However, there are applications for FBG-based contact force measurements where fibre orientation is difficult or impossible to control. One example application from the authors' previous work is contact force measurements between the articulating surfaces of cartilage within intact human joints such as the hip [19]. Contact force measurements over the cartilage surfaces of the hip, and other articular joints, can indicate the mechanics of the joint, which is closely linked to the etiology of joint degeneration and osteoarthritis [20]. In an intact human hip, the contoured cartilage surfaces of the femoral head and acetabulum are covered by a synovial fluid layer and

sealed by a fibrous joint capsule. The presence of synovial fluid within the joint prevents permanent fixation of sensors to cartilage surfaces with conventional adhesives or mechanical fixation. Because fixation is impossible, the orientation of fibre-based sensors with respect to the cartilage surfaces cannot be controlled. Moreover, because the joint capsule surrounds the entire joint and prevents optical access, it is impossible to orient sensors relative to cartilage surfaces using the techniques applied in the above applications of birefringent fibre.

To avoid the challenge of controlling sensor orientation, a non-birefringent FBG contact force sensor, with orientation-independent contact force sensitivity, was developed and applied *ex vivo* to intact cadaveric hips [19]. This sensor addresses limitations of the current standard film-based sensors [21, 22] for contact force measurements in joints because it can be implanted while leaving the joint capsule and synovial fluid layers intact.

This sensor exhibits orientation independence of sensitivity because of its axisymmetric configuration. However, like other sensors based on FBGs written in non-birefringent fibre, this sensor is also sensitive to both applied axial strain and temperature changes, which are two mechanical parameters that can confound force measurements on the contoured surfaces of articular joints. More recently, contact force sensors based on tilted FBGs have been proposed that also exhibit orientation independence of sensitivity [23]. However, these approaches are also susceptible to confounding errors associated with axial strain, bending and temperature.

The objective of the work reported here is to develop a birefringent FBG-based contact force sensor that addresses limitations of non-birefringent FBG sensors, namely

co-sensitivity to axial strain and temperature, and one limitation of FBG sensors in birefringent fibres: the necessity to control sensor orientation.

2. Materials and methods

2.1 Principles of FBGs, birefringence and D-shape optical fibre

FBGs are formed in optical fibres by creating a periodic variation in the refractive index of the fibre core [12, 24]. The length of the FBG and the magnitude and period of the variation in the refractive index determine the optical spectrum that is reflected by the FBG [12, 25]. When light spanning a broad range of wavelengths travels along the core of a non-birefringent fibre and encounters a Bragg grating (Figure C-1a), a single-peaked spectrum of wavelengths is reflected. This spectrum is centered at the Bragg wavelength, λ_B, which is given by:

$$\lambda_B = 2\Lambda n_0 \tag{C-1}$$

where, as shown in Figure C-1a, Λ is the spatial-period of the variation in the refractive index and, n_0, is the effective refractive index of the fibre core [12]. However, when light travels along the core of a birefringent optical fibre and encounters a grating, two single peaked spectra are reflected. One spectrum corresponds to light polarized along the slow axis (*s*) and the other corresponds to light polarized along the fast axis (*f*) (Figure C-1b):

$$\begin{aligned} \lambda_s &= 2\Lambda n_s \\ \lambda_f &= 2\Lambda n_f \end{aligned} \tag{C-2}$$

where the subscripts *s* and *f* denote the slow and fast axis, respectively. In general, because n_s and n_f differ in a birefringent fibre, the slow and fast axis Bragg wavelengths will be different, and the magnitude of the difference is termed the spectral separation.

The spectral separation between the slow and fast axis Bragg wavelengths, $\lambda_s - \lambda_f$ is given by:

$$\lambda_s - \lambda_f = 2\Lambda(n_s - n_f) = 2\Lambda B \tag{C-3}$$

where the refractive index difference between the slow and fast axis is referred to as the birefringence, B.

For any optical fibre, the birefringence in the fibre core can be expressed as the sum of three contributions [26]:

$$B = n_s - n_f = B_G + B_{IS} + B_E \tag{C-4}$$

where B_G is the geometric contribution that, typically, is found only in optical fibres with asymmetric or elliptical cores; B_{IS} is the internal stress contribution that, typically, is found in optical fibres with internal stress applying parts; and B_E is the external contribution to fibre birefringence that is typically caused by externally applied contact forces. There are two main classes of birefringent fibre that are distinguished by the predominant birefringence contribution that exists in the fibre core: either internal stress-induced birefringence or geometric birefringence.

In fibres with internal stress-induced birefringence, the difference in refractive index is created primarily by thermal residual stresses that are created within the fibre when the optical fibre cools from its drawing temperature to ambient temperature. Typically, there is no geometric contribution to birefringence. The thermal residual stresses are created by different thermal expansion coefficients the fibre core, clad and stress applying parts which are embedded in the clad. When the fibre, which initially has uniform temperature throughout its cross section, cools from its drawing temperature to

ambient temperature, thermal residual stresses evolve because the clad, stress applying parts and core undergo differing volume contractions. The configuration of the stress applying parts causes a uniform principal stress field in the region of the core which, through the stress-optic effect [14], results in a uniform difference in refractive index, or, alternatively, uniform B_{IS} throughout the core. In the context of contact force sensing, applied contact forces cause changes in the birefringence contribution B_E and, therefore, the Bragg wavelengths associated with the fast and slow axes of the fibre. The mechanisms underlying changes in Bragg wavelengths will be detailed after the principles of D-shape fibre are discussed. Examples of fibres with stress-induced birefringence include Side-hole, PANDA, and Bow Tie.

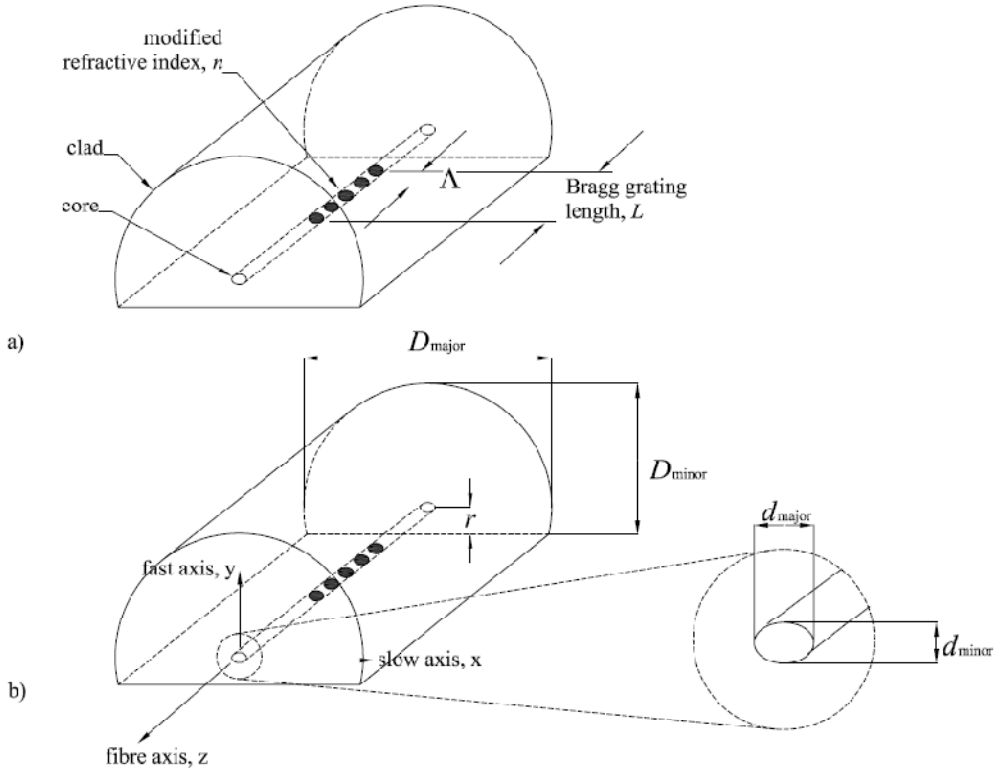

Figure C-1: a) schematic of D-shape fibre showing the clad, core and Bragg grating comprising regions of modified refractive index, *n* spaced with period, Λ. b) schematic of D-shape fibre showing variable names assigned to nominal major and minor outside diameters of fibre (D_{major} and D_{minor}) and minimum core offset from clad, *r*; major and

minor diameters of the elliptical core (d_{major} and d_{minor}); and the directions of the fibre axis, slow axis and fast axis.

D-shape optical fibre (Figure C-1a and C-1b) is one example of the second class of birefringent fibre that is based on geometric birefringence. While the physics and mathematics behind geometric birefringence is beyond the scope of this work, a qualitative discussion of birefringence in D-shape fibres with elliptical cores will be included.

The majority of birefringence in D-shape fibres is caused by the geometry of the fibre clad and elliptical core [27]. More specifically, the geometric birefringence of an optical fibre with an elliptical core is a function of the core location relative to the fibre surface, r (Figure C-1b); the major and minor diameters of the elliptical core, d_{major} and d_{minor}, respectively (Figure C-1b); the wavelength of the light propagating through the core; and the refractive indices of the clad, core and of the medium surrounding the fibre [28]. The internal stress contribution to birefringence is negligible at the wavelengths used for Bragg grating sensing applications [29]. When the major axis of the fibre core is aligned as shown in Figure 1b, the fast and slow axis of the fibre are normal and parallel to the flat-side of the D-shape clad (Figure C-1b), respectively. In the context of force sensing, applied forces cause changes in the birefringence contribution, B_E and, therefore, the Bragg wavelengths of the fast and slow axes.

There are two mathematical formulations that can be used to calculate changes in the Bragg wavelengths of the fast and slow axes as a function of applied contact forces. The first, or stress-optic, formulation relates changes in contact force-induced principal

stresses to changes in fibre birefringence. The changes in birefringence can then be used to calculate spectral separation (Equation C-3).

The second, or strain-optic, formulation can calculate *both* spectral separation and the magnitudes of the Bragg wavelengths for the fast and slow axes. This formulation relates changes in force-induced strains to changes in the Bragg wavelength of the fast axis and slow axis, which can then be used to calculate spectral separation. Because experimental data for the D-shape sensor will comprise fast axis, slow axis and spectral separation data, we will apply the strain-optic formulation because it can be used to calculate Bragg wavelengths for the fast and slow axes *and* spectral separation.

2.2 Strain-optic principles

As mentioned above, the Bragg wavelength of a FBG changes as a function of the mechanical strains in the core of the optical fibre. In the case of birefringent optical fibre, the changes in the Bragg wavelength of the light polarized along the slow axis (x-axis) and fast axis (y-axis) are given by:

$$\begin{aligned} \Delta\lambda_s &= \lambda_s \left[\varepsilon_z - \frac{n_s^2}{2}\left(p_{xz}\varepsilon_z + p_{xx}\varepsilon_x + p_{xy}\varepsilon_y \right) \right] \\ \Delta\lambda_f &= \lambda_f \left[\varepsilon_z - \frac{n_f^2}{2}\left(p_{yz}\varepsilon_z + p_{yx}\varepsilon_x + p_{yy}\varepsilon_y \right) \right] \end{aligned} \qquad \text{(C-5)}$$

where $\Delta\lambda$ denotes a change in Bragg wavelength; ε denotes mechanical strain with the subscripts referencing the fibre coordinate system shown in Figure C-1b; and $p_{xz} = p_{xy} = p_{yx} = p_{yz} = 0.252$ and $p_{xx} = p_{yy} = 0.113$ are strain-optic constants for typical Germanium-doped silica of the fibre core [12]. Note that the subscripts on the photoelastic constants are referred to the fibre coordinate system. To calculate the Bragg wavelength of the fast and slow axis for any state of strain the changes in Bragg

wavelength (Equations C-5) are added to the initial Bragg wavelengths (i.e. the Bragg wavelengths when the fibre is unstrained).

To predict the contact force-induced changes in Bragg wavelength for the sensor presented in this work the equations relating contact force and mechanical strain must be established. To establish the equations, the sensor geometry and orientation to contact force is presented.

2.3 Super-structured D-shape fibre sensor and force/strain models

As shown in Figure C-2, the contact force sensor consists of a D-shape birefringent fibre around which there is a super-structure that *both* transmits contact forces to the fibre *and* maintains the orientation of the sensor with respect to the contact force (Figure C-2a, C-2b and C-2d). As shown in Figure C-2c, the super-structured D-shape fibre sensor, hereafter referred to as *the sensor*, comprises an outside Polyimide© sheath (SmallParts Inc., Miami FL, Ds = 165 micron, t_W = 18 micron nominally) that contains a Nitinol© wire (Dynalloy Inc., Costa Mesa CA, Dw = 51 micron nominally) and a D-shape birefringent fibre (KVH Industries Inc., Middletown RI, D_{major} = 125 micron, D_{minor} = 76 micron, r = 14 micron, d_{major} = 8 micron, d_{minor} = 5 micron) with a 5 mm Bragg grating photo-inscribed in the fibre core (TechnicaSA, Beijing China, >50% reflectivity, <0.5 nm full width half maximum). The length, along the fibre axis (Figure C-1b), of the Polyimide© sheath and Nitinol© wire is 12 mm at the center of which is the 5 mm Bragg. The clearance space (Figure C-2d) between the sheath, wire and fibre is filled with a compliant adhesive (Dow Corning®, Midland MI, silicone 3-1753) that serves to maintain the alignment of the features comprising the super-structure. A Polyimide© alignment feature (Figure C-2a and C-2d) is affixed to the outside of the Polyimide©

sheath by submerging the sheath in a heat curable Polyimide© solution (HD MicroSystems™, Parlin NJ, solution PI-2525) and curing it into the geometry shown. The length of the alignment feature is nominally the same as the length of the sheath (i.e. 12 mm). The width of the alignment feature shown in Figure C-2a is 700 μm.

Contact forces, *F*, are applied to the outside of the sheath and are aligned with the internal features (e.g. wire and fibre) as shown in Figure C-2d (alignment feature omitted for clarity). The upper force is transmitted through the sheath, wire, and onto the fibre at contact 1. The lower force is transmitted through the sheath and onto the fibre at contact 2.

The key difference between the sensor shown in Figure C-2 and force sensors based on bare (i.e. not superstructured) D-shape fibre [4] is that the contact force transmitted to the flat side of the D-shape fibre of the super-structured sensor (Figure C-2d) is concentrated by the wire. Conversely, force sensors using bare D-shape fibre distribute forces over the entire flat side of the D-shape clad (Figure C-1). As will be shown, concentrating the contact force onto the fibre through the wire results in increased force sensitivity of the super-structured D-shape sensor relative to force sensors based on bare D-shape fibre. This increase in force sensitivity is predicted by the equations, developed below, relating contact force to strain in the fibre core.

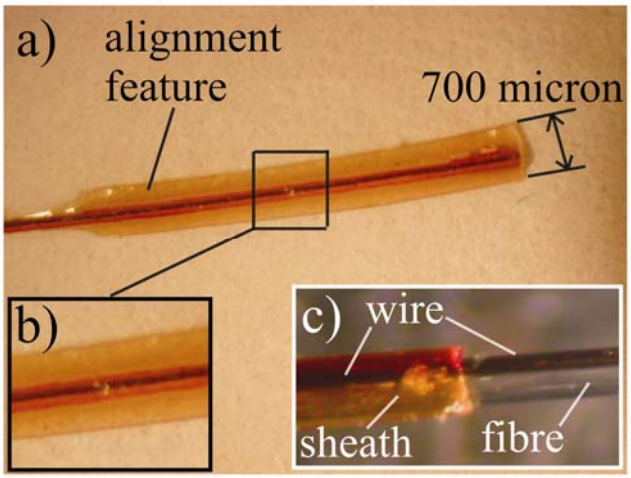

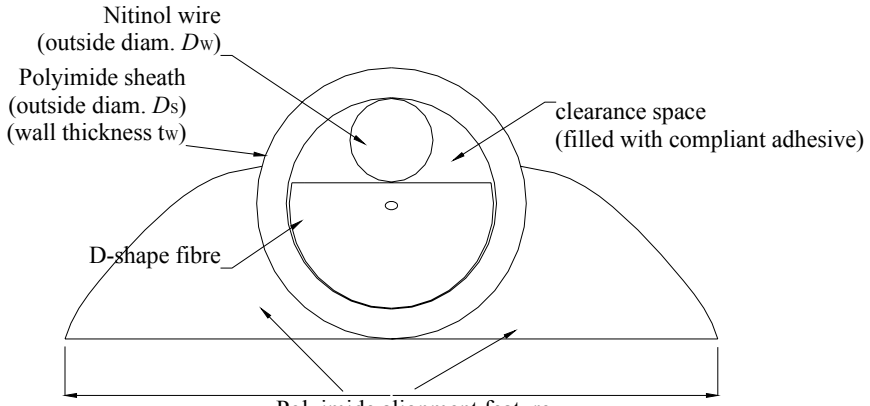

d)

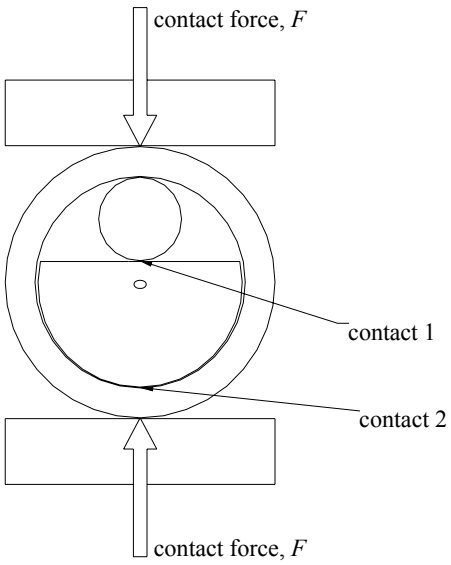

e)

Figure C-2: a) photograph showing the overall construction of the super-structured D-shape sensor. b) close-up view of a short segment of sensor length. c) photograph

showing Nitinol© wire, and fibre emerging from Polyimide© sheath. d) schematic cross section of super-structured D-shape sensor cross section showing Polyimide© sheath, Nitinol© wire, D-shape fibre and Polyimide© alignment feature. e) contact forces, *F* are applied to the outside of the sheath and are aligned with the internal features of the sensor as shown. The upper contact force is transmitted through the sheath, to the wire and to the fibre at contact 1. The lower force is transmitted through the sheath to the fibre at contact 2.

A plane elasticity model is used to calculate the stresses and strains created in the D-shape fibre core as a result of applied contact forces. To calculate the stresses and strains, the D-shape fibre is approximated as an elastic half-space [30] subjected to contact forces of magnitude *F* (N/mm, normalized to sensor length along the fibre axis).

One of the key assumptions associated with elastic half-space theory is that stresses and strains vanish at distances infinitely far from the point of force application. In the case of D-shape fibre, which is finite in size, this assumption cannot be satisfied. To address this difference between the boundary conditions of half space theory and the D-shape fibre sensor, a *composite half space model* is proposed that accounts for the shape and boundary conditions of the super-structured D-shape fibre sensor.

As shown in Figure C-3a, elastic half-space formulations of contact consist of a contact force applied at the origin of a large elastic continuum [30]. To satisfy boundary conditions, when x and y are large, all stresses and strains vanish and static equilibrium is achieved by internal stresses that balance the external force. The stresses at any location in the elastic continuum are:

$$\begin{aligned}
\sigma_x &= -\frac{2F}{\pi}\frac{x^2 y}{(x^2+y^2)^2} \quad ; \quad \sigma_{x'} = -\frac{2F}{\pi}\frac{x'^2 y'}{(x'^2+y'^2)^2} \\
\sigma_y &= -\frac{2F}{\pi}\frac{y^3}{(x^2+y^2)^2} \quad ; \quad \sigma_{y'} = -\frac{2F}{\pi}\frac{y'^3}{(x'^2+y'^2)^2} \\
\tau_{xy} &= -\frac{2F}{\pi}\frac{xy^2}{(x^2+y^2)^2} \quad ; \quad \tau_{x'y'} = -\frac{2F}{\pi}\frac{xy^2}{(x'^2+y'^2)^2}
\end{aligned} \tag{C-6}$$

where σ_x, σ_y, τ_{xy} are the normal stresses aligned with the x and y directions and the shear stress the xy plane, respectively [30]. The equations for stress referred to the x', y' coordinate system are also shown.

To address the difference in boundary conditions between the elastic half space (Figure C-3a) and the D-shape fibre sensor (Figure C-3b) we use superposition of Equations C-6 to obtain the total state of stress in the super-structured sensor, as described below.

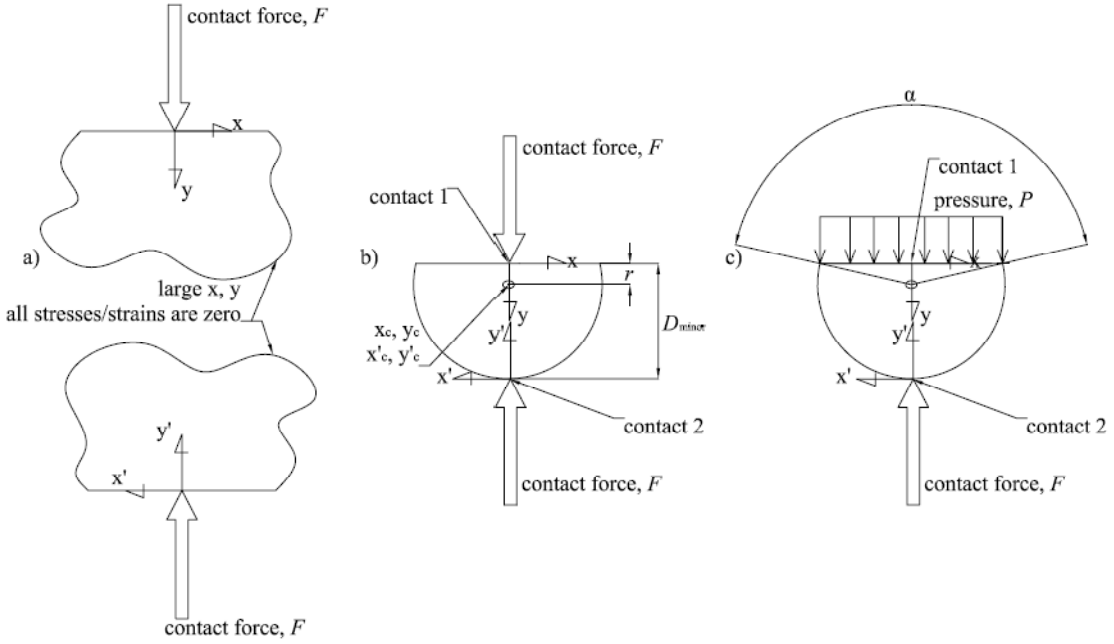

Figure C-3: a) schematic showing contact force, *F* applied to elastic half space with zero stress boundary condition at regions far from co-ordinate system origin. b) schematic showing D-shape fibre cross section as a composite elastic half space. The core of the fibre is located relative to two co-ordinate systems with origins at contact 1 and contact 2. The co-ordinate of the core relative to contact 1 and contact 2 is x_1, y_1 and x'_2, y'_2, respectively. c) schematic representation of half space model for a bare D-shape fibre subjected to distributed contact force over the flat side of the clad (pressure, *P*) and concentrated contact force on the round side of the clad.

Contact forces applied to the sensor (Figure C-2) are approximated using the boundary conditions shown in Figure C-3b. We assume that the contact forces applied to the top

and bottom of the sheath (Figure C-2b) are transmitted to the D-shape fibre at contact 1 and contact 2, respectively (Figure C-3b). To calculate the stresses at any location in the D-shape fibre, we add the stress Equations C-6 for the elastic continuum with the x, y coordinate system to the stress Equations C-6 for the elastic continuum with the x', y' coordinate system (Figure C-3a). Because we assume linear elasticity, this process of stress superposition results in the state of stress shown as Equations C-7:

$$\begin{aligned}
\sigma_x &= -\frac{2F}{\pi}\left[\frac{x_1^2 y_1}{(x_1^2+y_1^2)^2}+\frac{x'^2_2 y'_2}{(x'^2_2+y'^2_2)^2}\right] \\
\sigma_y &= -\frac{2F}{\pi}\left[\frac{y_1^3}{(x_1^2+y_1^2)^2}+\frac{y'^3_2}{(x'^2_2+y'^2_2)^2}\right] \\
\tau_{xy} &= -\frac{2F}{\pi}\left[\frac{x_1 y_1^2}{(x_1^2+y_1^2)^2}+\frac{x'_2 y'^2_2}{(x'^2_2+y'^2_2)^2}\right]
\end{aligned} \qquad \text{(C-7)}$$

where $y' = D_{minor} - y$ and $x' = -x$. Note that Equations C-7 give the total stresses referred to the x, y coordinate system in terms of x, y and x', y'. In the region of the centre of the fibre core, where the majority of light is transmitted, the dimensions x, x' are small relative to the dimensions y, y' and Equations C-7 can be simplified as:

$$\begin{aligned}
\sigma_x &= 0 \\
\sigma_y &= -\frac{2F}{\pi}\left[\frac{1}{y_c}+\frac{1}{y'_c}\right] \\
\tau_{xy} &= 0
\end{aligned} \qquad \text{(C-8)}$$

where $y_c = r$ and $y'_c = D_{minor} - r$ (Figure C-3b). Based on Equations C-8, in the region of the centre of the fibre core there is negligible shear and there is one non-zero principal stress. The state of stress can be used with Hooke's Law for plane strain [30] to obtain strains:

$$\varepsilon_x = \frac{1}{E}\left((1-\nu^2)\sigma_x - \nu(1+\nu)\sigma_y\right) = \frac{-\nu(1+\nu)\sigma_y}{E}$$
$$\varepsilon_y = \frac{1}{E}\left((1-\nu^2)\sigma_y - \nu(1+\nu)\sigma_x\right) = \frac{(1-\nu^2)\sigma_y}{E} \qquad \text{(C-9)}$$
$$\gamma_{xy} = \frac{2(1+\nu)}{E}\tau_{xy} = 0$$

where E and ν are the Young's modulus and Poisson ratio of the silica glass of the fibre, and were assumed to be 77 GPa and 0.17, respectively [29]. When Equations C-7 are substituted into Equations C-9, the resulting expressions for strain are functions of contact force, *F*, and the co-ordinates of the core relative to contact 1 and contact 2. For the sensor presented in Figure C-2, y_c and y'_c are constant: 14 microns and 62 microns, respectively.

For the purpose of comparison of the contact force sensor presented in this work and contact force sensors based on bare D-shape fibre, we have also developed a half-space model to estimate the stresses and strains in a bare D-shape fibre (Figure C-3c). In this model, contact force on the flat side of the clad is distributed, shown as contact pressure, *P*, while contact force on the opposite side of the fibre remains concentrated. We apply similar reasoning as that described for Figure C-3b to obtain the stresses in the region of the fibre core as:

$$\sigma_x = \frac{-P}{\pi}(\alpha - \sin\alpha)$$
$$\sigma_y = \frac{-P}{\pi}(\alpha + \sin\alpha) - \frac{2F}{\pi}\left[\frac{1}{y'_c}\right]$$
$$\tau_{xy} = 0 \qquad \text{(C-10)}$$

where P is the applied pressure (N/mm^2) and α is the included angle (i.e. 2.73 radians for D-shape fibre) that is subtended by the pressure [30]. The boundary conditions shown in

Figure C-3b do not completely satisfy those of half-space theory because the pressure boundary condition extends to dimensions comparable to the fibre diameter. Nevertheless, Equations C-10 can serve to approximate the state of stress and be used to gain insight into increases/decreases in sensitivity between the sensor presented here and those based on bare D-shape fibre. The state of stress given by Equations C-10 can be substituted into Hooke's Law for plane strain to obtain the strains in a similar form to Equations C-9.

The contact force-induced strains for the sensor presented here (Equations C-9), and those for a bare D-shape sensor, can then be substituted into Equations C-5 to calculate the Bragg wavelength shifts for the fast and slow axes for the sensor presented in this work and that of a bare D-shape fibre subjected to contact force.

Force-induced Bragg wavelength shift calculations were completed for contact forces ranging from 0 N/mm to 2 N/mm to predict force sensitivity. Equations C-5 were also used to calculate the axial strain sensitivity, for the contact force sensor, as described in Section 2.4.

2.4 Sensor calibration protocols

A contact force sensor was constructed and calibrated for sensitivity to contact-force, axial strain and temperature in three separate calibration protocols.

2.4.1 Contact force calibration protocol

The apparatus used for contact force calibration was identical to that used in a previous study (Figure C-4a) [19]. The force sensor and a support cylinder of identical outside diameter were subjected to contact force between two metrology gauge blocks (Class 0, 24.1 mm × 24.1 mm, steel, Mitutoyo Can., Toronto, ON). The bottom gauge block supported the force sensor and support cylinder and the top block applied contact forces. Both gauge blocks were constrained by guide blocks allowing motion only in the direction of load application.

Contact forces were applied by compressing a calibrated spring with a manual screw-follower (not shown in Figure C-4a). These forces were transmitted through a pre-calibrated load cell (445 N capacity, ±0.1% FS non-repeatability, Futek Inc., Irvine, CA), fixed to the top gauge block, connected to a data-acquisition system implemented in LabView™ (version 8, National Instruments Inc., Austin, TX). Force was transmitted through the top gauge block, through the sensor and support cylinder and finally to the bottom gauge block. Applied contact forces in all calibrations ranged from 0 N mm^{-1} to, nominally, 2 N mm^{-1}. This range of forces was chosen because it brackets the range of forces experienced in the hip during walking [57].

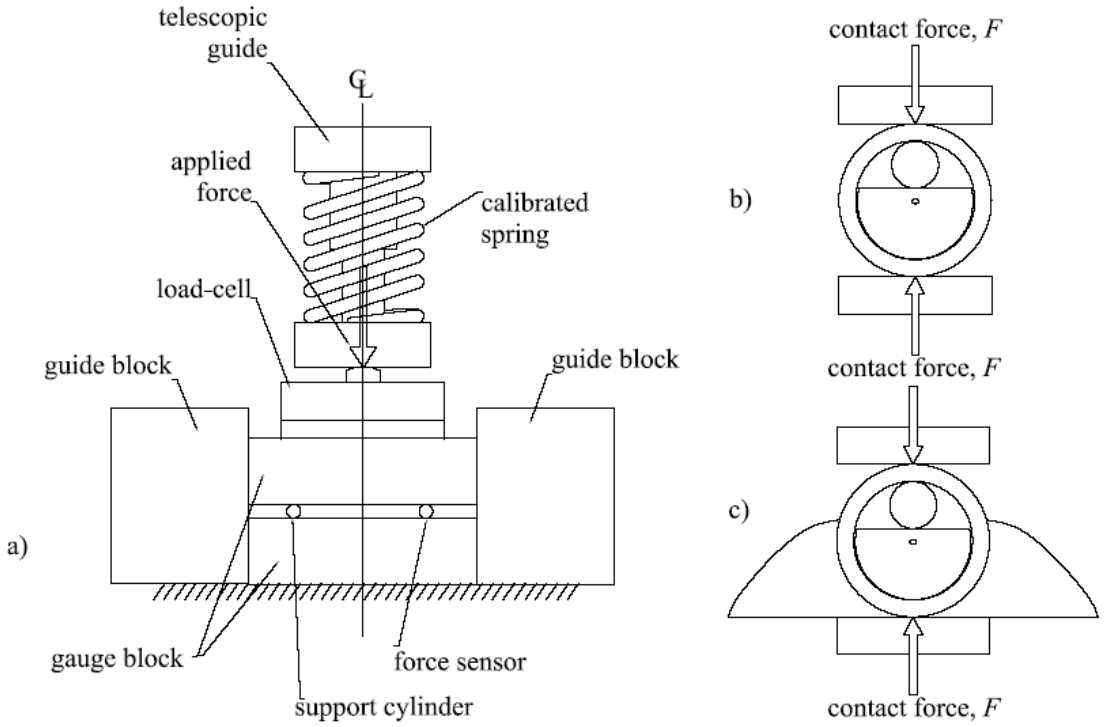

Figure C-4: a) schematic showing relevant features of contact force calibration apparatus. Force is applied by compressing a calibrated spring that is in contact with a load cell and top gauge block. Forces are transmitted through the force sensor and support cylinder, and to the bottom gauge block. b) schematic showing forces applied to force sensor without alignment feature, and c) with alignment feature.

Calibration for sensitivity was completed for a sensor without an alignment feature (Figure C-4b), and for a sensor with the alignment feature (Figure C-4c). For the sensor without the alignment feature, sensor orientation was controlled with an external fibre rotator while contact forces were applied. The alignment feature was then added to the sensor and calibration was repeated without external orientation control. One calibration was performed for the sensor without an alignment feature, while three were performed for the sensor with the alignment feature. Bragg wavelength shifts of the fast and slow axes were measured using an optical spectrum analyzer (ANDO AQ6331, Tokyo, Japan).

Bragg wavelengths were demodulated by directing light from a broad C-band light source (AFC-BBS1550, Milpitas, California) into a linear polarizer (PR 2000, JDS Uniphase, Milpitas, California) and then into one of the input channels of a 3 dB optical coupler (Blue Road Research). The light was then directed *via* the coupler to the FBG in the test fiber, and the reflected spectrum was directed back through the optical coupler and into the optical spectrum analyzer. The polarization of the light was adjusted to illuminate either the fast or the slow axis of the fiber by using the tuning facilities of the linear polarizer. The demodulation scheme described is similar to that presented by numerous researchers [3, 31, 32].

Contact force sensitivity was calculated using linear regression (SigmaPlot 9.01®, Systat Software Inc., Chicago IL) as the slope in the recorded data (slope ± standard deviation for slope), in terms of wavelength shift versus applied force. Sensitivity was also calculated based on the spectral separation of the slow and fast axes (i.e. the difference between the sensitivities of the slow and fast axes).

2.4.2 Axial strain calibration protocol

In the axial strain protocol, the sensor was affixed to the top surface of an aluminum cantilever (Figure C-5, cantilever width = 25 mm, depth = 0.25 mm, L = 45 mm, and l = 10 mm) using a UV curable adhesive (Norland Products Inc., Cranbury NJ, Blocking adhesive 107). To create axial strains in the cantilever, prescribed deflections were applied to the end of the cantilever. The prescribed deflections were measured using a mechanical indicator (Mitutoyo Corp., JP, Indicator 2046F, 10 mm range), while Bragg wavelengths of the fast and slow axes were recorded. As mentioned in Section 2.3, the axial strains transmitted to the sensor from the cantilever were estimated from the

deflections using classical beam equations [33] by assuming that the tensile strains at the sensor/beam interface (at location *l*, Figure C-5) were transmitted to the sensor. The estimated axial strains ranged from 0 με to 70 με. The protocol was conducted twice.

The sensitivity to strain, for both the slow and the fast axes and based on spectral separation, was calculated by using linear regression as the slope in the recorded data, in terms of wavelength shift versus strain. To verify that results from this experiment agreed with strain-optic theory and the known behaviour of D-shape fibres subjected to axial strain [15], the axial strains, and corresponding transverse Poisson strains, for the cantilever beam were used with Equations C-5 to predict the Bragg wavelength shifts. Verification involved comparison of the experimentally measured wavelength shifts to the strain-optic model predicted wavelength shifts.

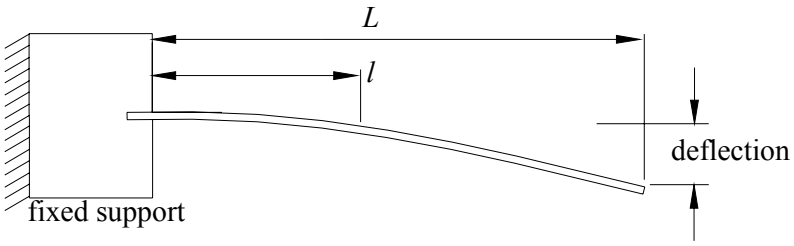

Figure C-5: schematic (not to scale) showing relevant features of axial strain calibration apparatus. The force sensor was affixed to the top of the cantilever at a distance, *l* from the fixed support. Prescribed deflections were applied to the end of the cantilever, *L*.

2.4.3 Temperature calibration protocol

Temperature calibration was performed within a controllable oven (Watlow Controls Inc., Winona MN, Model CascadeTEK, controller series 982). The force sensor and a pre-calibrated thermocouple (Omega Engineering Inc., Stamford CT, Type-T), interrogated with a thermocouple amplifier (Omega Engineering, Super MCJ), were fixed to a glass slide (VWR International™, 76 mm by 26 mm by 1 mm) and placed within the

oven. The temperature of the force sensor, as measured by the thermocouple, was increased from 30 ˚C to 60 ˚C, in 5 ˚C increments, while the Bragg wavelengths of the fast and slow axes were recorded. This temperature range was chosen because it spans a larger range than that experienced in most *ex vivo* experiments with cadaveric material. The protocol was repeated three times. The sensitivity to temperature, for both the slow and the fast axes and based on spectral separation, was calculated by using linear regression as the slope in the recorded data, in terms of wavelength shift versus temperature.

3. Results

Figure C-6 shows spectra recorded using the optical spectrum analyzer for both the fast and slow axes. As shown, the Bragg spectra of both the fast and slow axes are symmetric about their initial Bragg wavelength when the sensor is not subjected to contact force. As force is applied to the sensor, both the fast and slow axis Bragg wavelengths shift to longer wavelengths while the spectra retain symmetry. The symmetry exhibited by the fast and slow axis spectra, when the sensor is subjected to force, indicates that the strains experienced along the FBG are uniform along the grating length. Non-uniform strains over the grating length would manifest in increased width, along the wavelength axis, of the Bragg spectra and decreased peak intensity [25]. As shown in Figure C-6, the slow axis Bragg wavelength experiences greater shift than the fast axis. Therefore, as described below, the slow axis Bragg wavelength exhibits greater sensitivity to contact force than the fast axis (Figure C-7 and Table C-1).

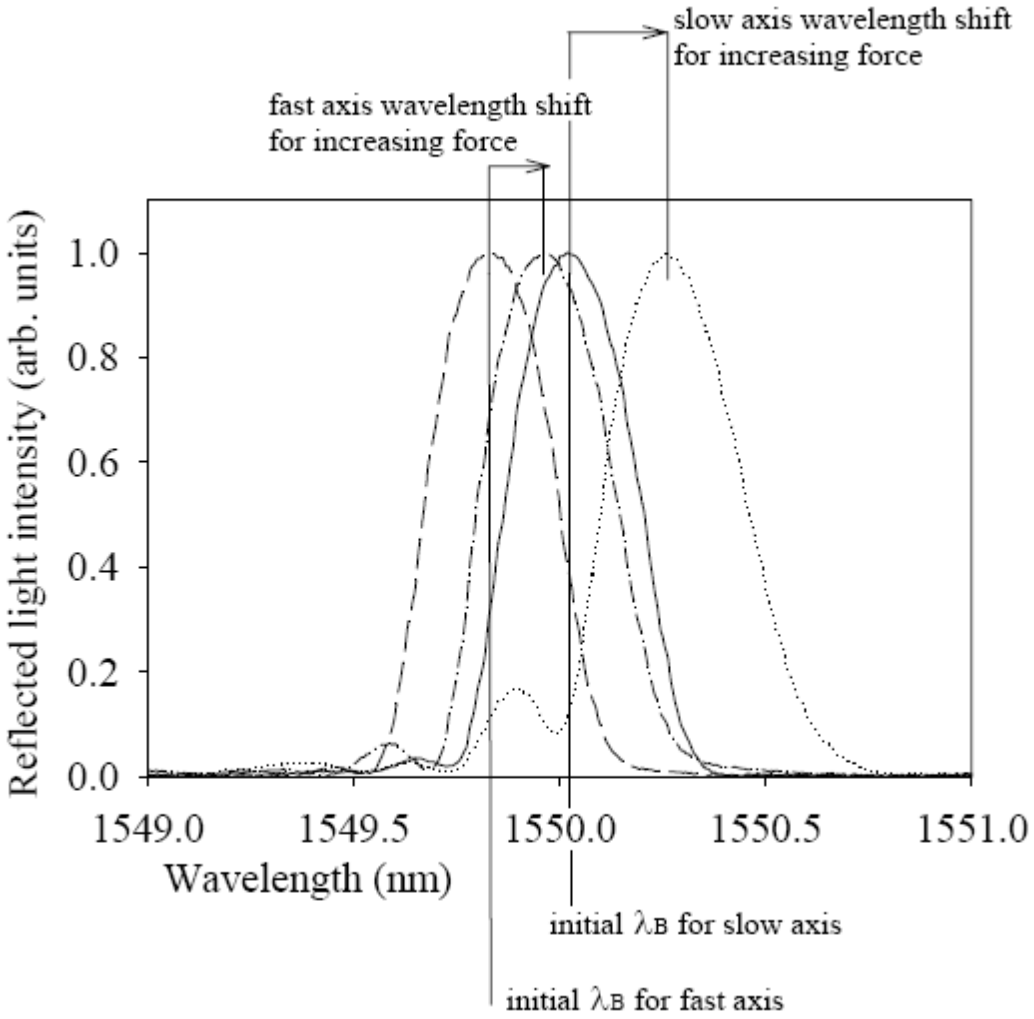

Figure C-6: Bragg spectra for the fast and slow axes recorded using the optical spectrum analyzer. Contact forces applied to sensor cause shifts to longer Bragg wavelengths. The symmetry of the spectra indicate that strains along grating are uniform while the relative shifts of the slow and fast axis indicate that the slow axis has greater force sensitivity than the fast axis.

Figure C-7a shows the predicted wavelength shifts of the fast and slow axis Bragg wavelengths obtained from the half-space/strain-optic model, while Figure C-7b shows the measured Bragg wavelength shifts for the contact force sensor without the alignment feature. As shown, for the super-structured sensor, the model predicted (Figure C-7a) and measured (Figure C-7b) slopes, or sensitivities to contact force, match to within 1.8 %

and 13.2 % (relative to experimental slope) for the slow and fast axes, respectively. The modeled slow and fast axis sensitivities for the super-structured sensor are 125.4 % and 3.5% (Figure C-7a) greater than those modeled for a bare D-shape sensor.

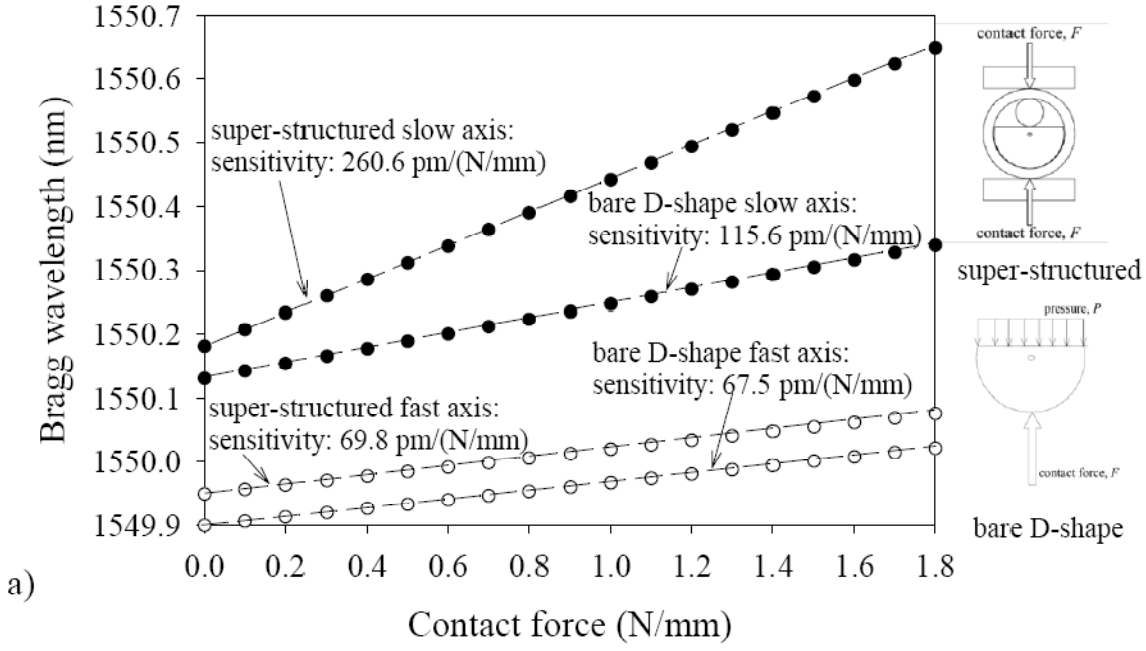

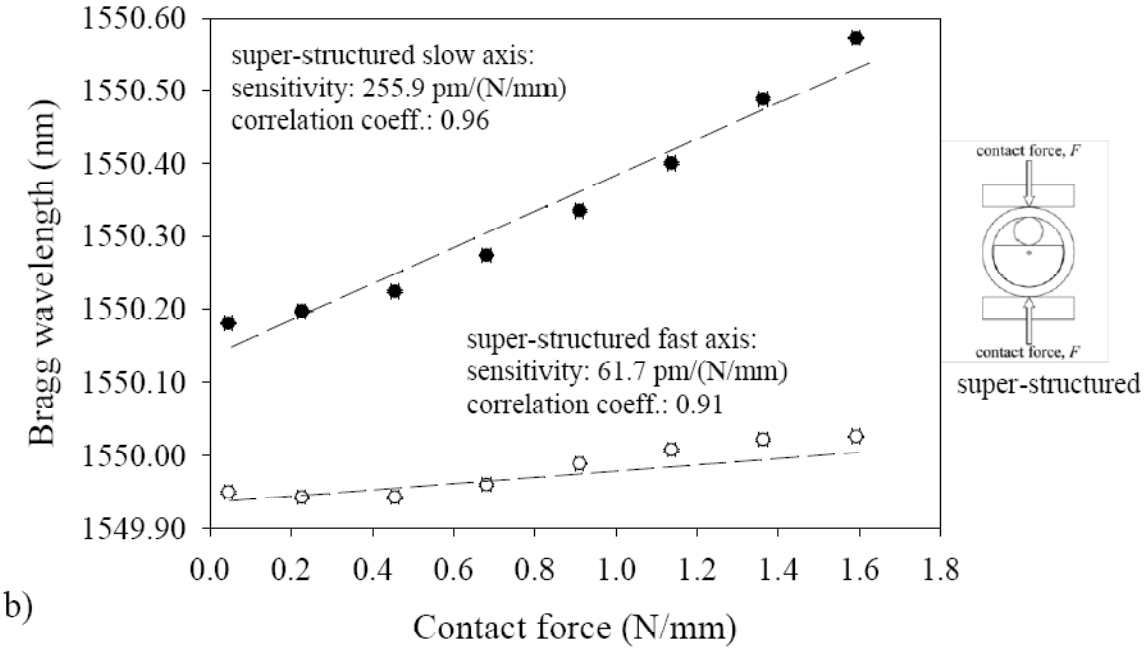

Figure C-7: a) Predicted sensitivities of the fast and slow axis Bragg wavelengths obtained from the half-space/strain-optic model for both the super-structured sensor and a bare D-shape sensor. b) measured wavelength shifts of the fast and slow axis Bragg

wavelengths for the sensor without the alignment feature. Sensitivities are reported as slope from regressions (dashed lines). Error bars shown are not visible at given scale but convey non-repeatability of contact force measurements (±0.02 N/mm) and observed non-repeatability of wavelength shift measurements (mean of ±1 pm for all data points presented) from optical spectrum analyzer.

Table C-1: Summary of experimental results for slow and fast axis sensitivity to contact force, axial strain and temperature of contact force sensor. Sensitivities reported obtained using linear regression and are reported as the best-fit slope ± the standard deviation on slope. Correlation coefficients, r^2, also obtained from regression calculations.

			Sensitivity (pm/measurand unit)				
Calibration protocol	Measurand unit	Trial	Slow axis	r^2†	Fast axis	r^2†	Spectral separation
contact force, without alignment feature	(N/mm)	1	255.9±21.1	0.96	61.7±8.00	0.91	194.2
contact force, with alignment feature	(N/mm)	1	228.6±4.0	0.99	62.4±3.7	0.98	166.2
		2	232.1±4.3	0.99	62.5±4.1	0.98	169.6
		3	234.3±4.1	0.99	61.6±5.4	0.96	172.7
		mean	231.7	0.99	62.2	0.97	169.5
axial strain, with alignment feature	(micro-strain)	1	1.10±0.08	0.97	1.09±0.10	0.95	0.01
		2	1.13±0.08	0.96	1.13±0.02	0.99	0.00‡
		mean	1.12	0.97	1.11	0.97	0.01
temperature, with alignment feature	(degree Celsius)	1	8.44±0.16	0.99	9.58±0.31	0.99	-1.14
		2	8.45±0.13	0.99	9.53±0.31	0.99	-1.08
		3	8.41±0.14	0.99	9.55±0.31	0.99	-1.14
		mean	8.43	0.99	9.55	0.99	-1.12

notes:

† r^2 is abbreviated notation for linear correlation coefficient from least squares regression

‡ no measurable difference

Figure C-8 shows typical measured Bragg wavelength shifts for the contact force sensor with the alignment feature (trial 1, results also noted in Table C-1). As shown by the results in Table C-1 (force, with alignment feature), both the slow and fast axis sensitivities are nearly constant over the three trials in which the sensor aligns itself (experimental configuration shown in Figure C-4c). The lowest and highest sensitivities over the three trials deviate from the tabulated mean sensitivities for the slow and fast axis by only -1.3% and 1.1% for the slow axis and -0.9% and 0.5% for the fast axis

(Table C-1). The lowest and highest spectral separation sensitivities deviate from the mean (i.e. 169.5 pm/(N/mm)) by only -1.9% and 1.9% (Table C-1).

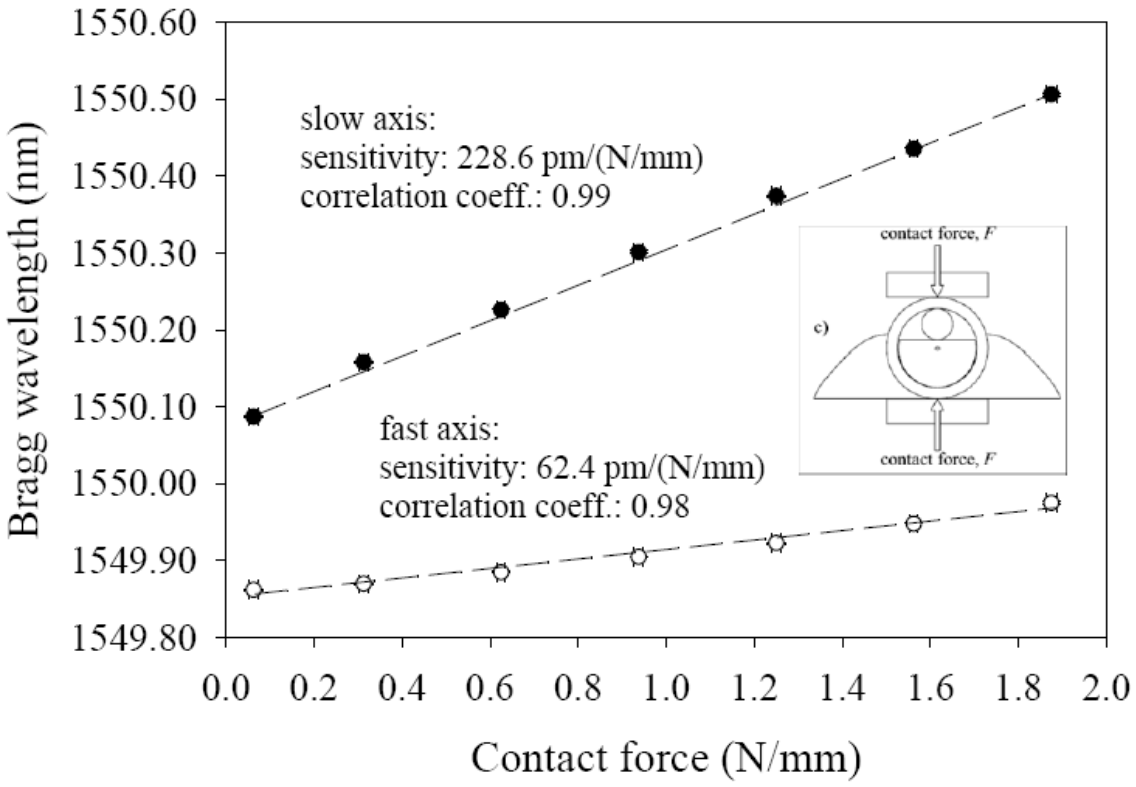

Figure C-8: measured wavelength shifts of fast and slow axis Bragg wavelengths for contact force sensor with alignment feature (trial 1 in Table 1). Error bars (±0.02 N/mm and ±1 pm) not visible at given scale.

Figure C-9a shows the strain/strain-optic model predicted wavelength shifts for the fast and slow axis as a function of axial strain along the FBG. As shown, the model predicted sensitivities of the fast and slow axis differ by only 0.008% of the mean sensitivity of the fast and slow axis (i.e. 1.24475 pm/microstrain). Note that the number of significant digits reported above and in Figure C-9a is chosen to convey the 0.008% difference and should not be interpreted as indicating ability to measure wavelength shifts to 10^{-4} pm. The measured changes in Bragg wavelength versus axial strain (Figure C-9b) also show nearly identical sensitivity for the fast and slow axis (also shown in Table C-1,

axial strain, with alignment feature). The mean difference between the fast and slow axis sensitivities reported for trial 1 and 2, shown in Table C-1, is 0.9%.

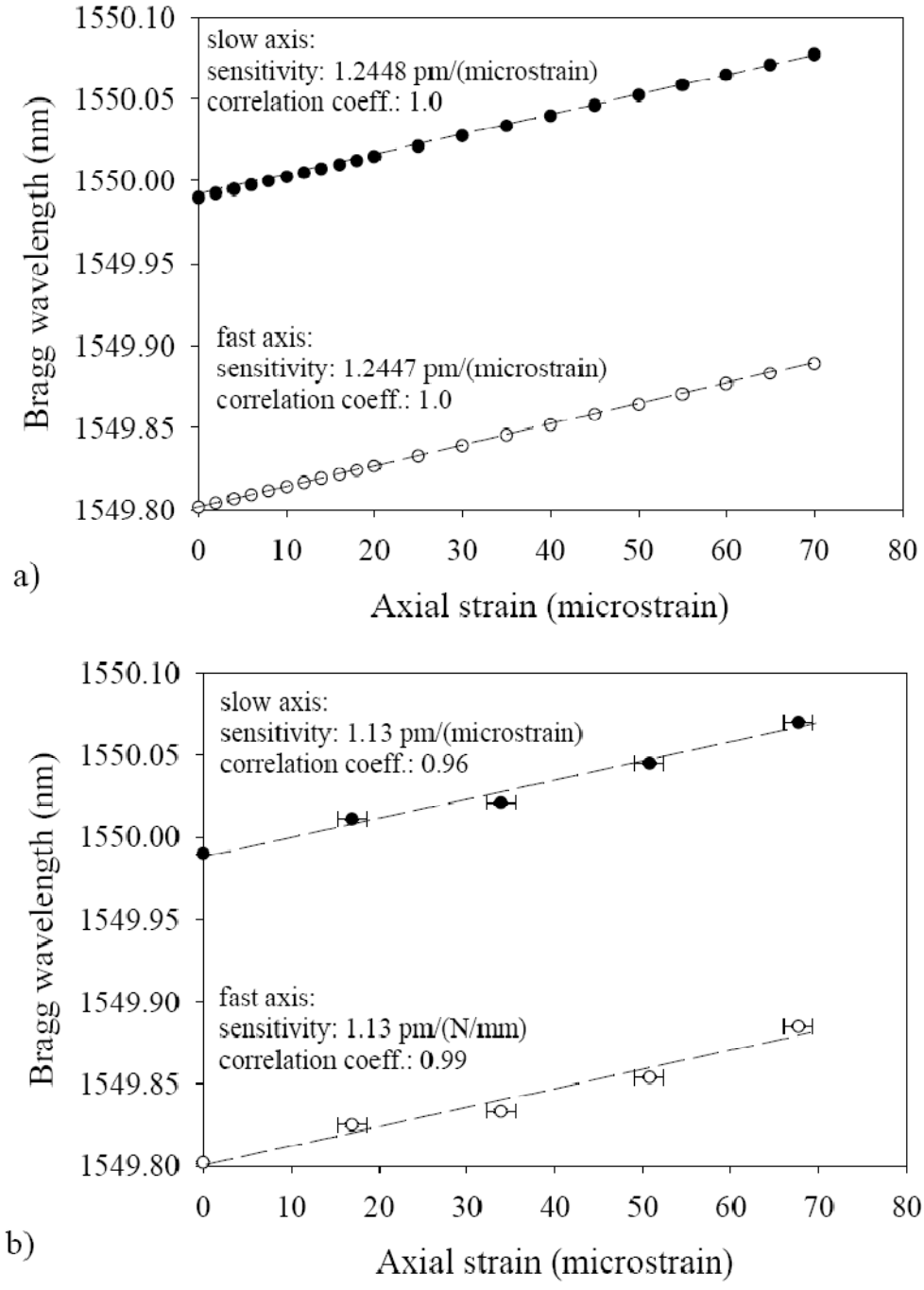

Figure C-9: a) Predicted sensitivities to axial strain of the fast and slow axis Bragg wavelengths obtained from the strain/strain-optic model. b) measured (trial 2) wavelength shifts of the fast and slow axis Bragg wavelengths for the sensor with the alignment feature. Sensitivities are reported as slope from regressions (dashed lines). Error bars

shown are not clearly visible at given scale but convey non-repeatability of axial strain values (±1.69 micro-strain) and observed non-repeatability of wavelength shift measurements (mean of ±1 pm for all data points presented) from optical spectrum analyzer.

Figure C-10 shows typical results obtained during the temperature calibration protocol (Table C-1, temperature, with alignment feature). Like the results for axial strain calibration, the fast and slow axis sensitivities to temperature are similar. For example, as shown by the results based on spectral separation (Table C-1), the mean difference between the fast and slow axis sensitivities was 12.4 % of the mean of the fast and slow axis sensitivities (i.e. 8.99 pm/degree Celsius).

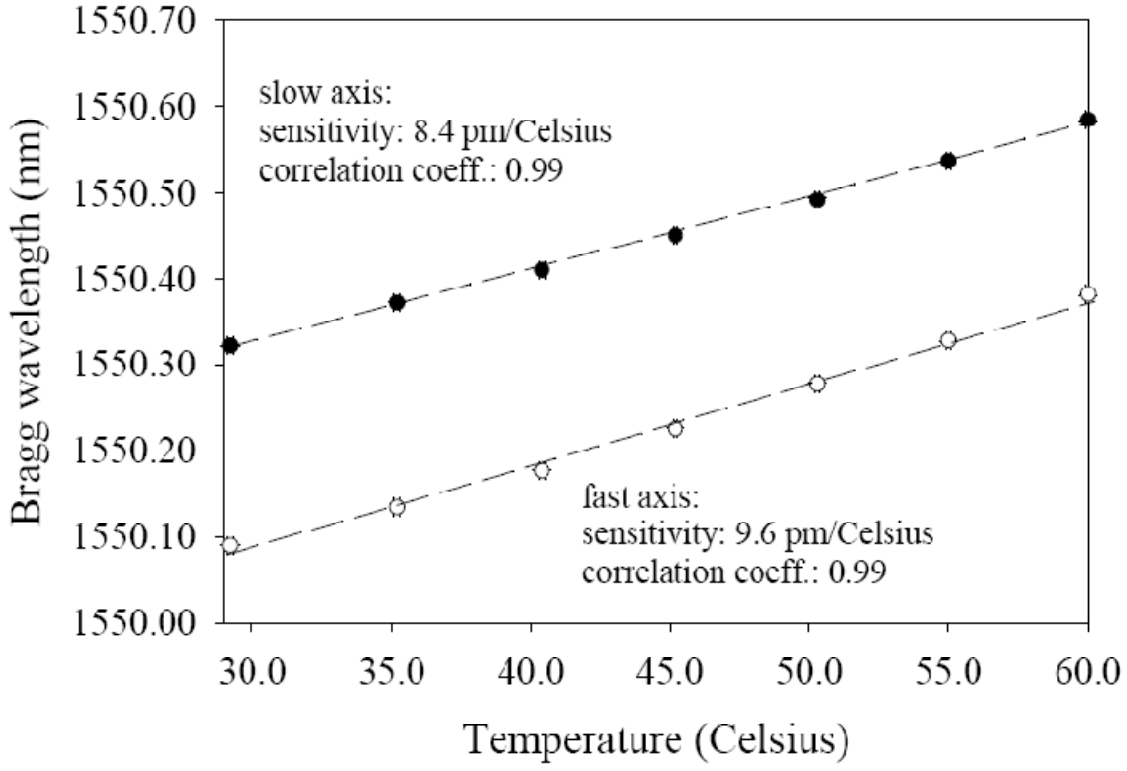

Figure C-10: measured (trial 1) fast and slow axis Bragg wavelengths versus temperature for the contact force sensor with the alignment feature. Sensitivities are reported as slope from regressions (dashed lines). Error bars shown are not clearly visible at given scale but convey non-repeatability of thermocouple measurements (±0.1 degrees Celsius) and observed non-repeatability of wavelength shift measurements (mean of ±1 pm for all data points presented) from optical spectrum analyzer.

4. Discussion

The contact force sensor presented in this work has desirable characteristics when compared to other birefringence-based force sensors including: increased sensitivity to contact force relative to bare-D shape fibre; near-constant force sensitivity without external orientation control; and negligible co-sensitivity to extraneous axial strain and temperature changes. Insights gained from the half-space/strain-optic model, with reference to sensor design features, can be used to elucidate the causes of these benefits.

4.1 Contact force, axial strain and temperature calibration

The principal cause of the increase in slow axis sensitivity shown in Figure C-7a is a 273% increase (not explicitly reported in Section 3.0), relative to the case of bare D-shape fibre, in compressive stresses, σ_y, that results from concentrating contact forces at contact 1 with the Nitinol© wire. Conversely, fast axis sensitivities of the super-structured and bare D-shape sensors match to within 3.5% (Figure C-7a) because the state of stresses in the two sensors (Equations C-8 for super-structured and Equations C-10 for bare fibre) lead to mechanical strains in the core that cause nearly identical fast axis wavelength shifts for a given contact force. Experimental measurements of sensitivity agree with model-predicted sensitivities for the super-structured sensor and, thereby, validate that model predicted increases in compressive stresses lead to increased sensitivity of the slow axis Bragg wavelength (Figure C-7a and Figure C-7b).

The reported sensitivities for the super-structured sensor with the alignment feature (Figure C-8 and Table C-1) show that the alignment feature repeatably orients the sensor with respect to contact forces. It is worth noting that, for the sensor with the alignment feature, the mean slow axis sensitivity (i.e. 231.7 pm/(N/mm)) is 9.5% lower

than the slow axis sensitivity measured without the alignment feature (i.e. 255.9 pm/(N/mm)). For the fast axis, differences in sensitivities are negligible. We hypothesize that the alignment feature on the underside of the sensor (Figure C-2a) could diminish the force transferred to the D-shape fibre at contact 2 (Figure C-3b). The result of diminished force transfer at contact 2 is diminished compressive stress in the fibre core and, as a consequence, diminished sensitivity. Nevertheless, the slow axis sensitivity of the sensor with the alignment feature remains comparable to that of the sensor without the alignment feature and nearly constant over the three trials reported in Table C-1 without external control of sensor orientation. The sensitivity is also comparable to the highest sensitivity measured for commercially available birefringent fibre.

In a recent study by Chehura *et al.* (2004), the sensitivities of several commercial birefringent fibres were measured and the highest sensitivity was 230 ± 20 pm/(N/mm) for Elliptical core fibre [4] that is not self aligning with respect to contact forces. The self aligning super-structured sensor reported here has a mean sensitivity of 231.7 pm/(N/mm) (Table C-1).

The super-structured sensor presented here also has negligible co-sensitivity to both axial strain and changes in temperature. The mean force sensitivity of the super-structured sensor in terms of spectral separation sensitivity is 169.5 pm/(N/mm) (Table C-1). The mean axial strain sensitivity, in terms of spectral separation, is 0.01 pm/(microstrain). Based on these sensitivities, a force measurement error of 1% due to axial strain would require that approximately 170 microstrain be applied to the sensor. The mean temperature sensitivity is -1.12 pm/(degrees Celsius) and a 1% error due to temperature would require a temperature change of approximately 1.5 degree Celsius.

Both of these error scenarios indicate that axial strain and temperature errors of the super-structured sensor are negligible over strain and temperature ranges that would be experienced in the *ex vivo* applications described for our previous work [19].

The results for slow and fast axis sensitivity to axial strain and temperature are in close agreement with previous literature. The mean of the slow and fast axis sensitivities to axial strain is 1.12 pm/(microstrain), which is approximately identical to the axial strain sensitivity reported for FBGs in many optical fibres (e.g. approximately 1.20 pm/(microstrain) [12]. For temperature, the mean of the slow and fast axis sensitivities is 9.00 pm/(degree Celsius), which is approximately 18 % lower than that reported for bare D-shape fibre (i.e. approximately 11 pm/(degree Celsius) [4]).

The super-structured sensor also addresses the well-known fragility of bare D-shape fibre [34] by encasing the D-shape fibre in adhesive and a rugged polyimide sheath. Although the sensor was not systematically tested for robustness relative to bare D-shape fibre, there is anecdotal evidence from the work presented here that the sensor is robust. Specifically, the sensor presented was subjected to repeated tests for axial strain sensitivity, temperature sensitivity, and force sensitivity in various orientations over several days of consecutive testing while the light guiding properties of the fibre and reflection spectrum of the grating remained essentially unchanged.

4.2 Half-space/strain-optic modeling

Although the half-space/strain-optic models predict increases in sensitivity and correctly predict the sensitivity of the super-structured sensor, there are significant differences between the modeled sensitivity of the bare D-shape fibre (Figure C-7a) and measured results published by previous researchers [4]. These differences indicate

limitations of the half-space model when applied to the bare D-shape sensor. As shown in Figure C-7a, the predicted slow and fast axis sensitivities for the bare D-shape sensor are 115.6 pm/(N/mm) and 67.5 pm/(N/mm), respectively. Published sensitivities for bare D-shape fibre are 180 ± 20 pm/(N/mm) and 61 ± 9 pm/(N/mm) for the slow and fast axis, respectively [4]. For the fast axis, the modeled sensitivity is only 10.6% larger than the measured sensitivity, while for the slow axis the modeled sensitivity is 35.8% lower than the measured sensitivity. We hypothesize that a significant factor contributing to these differences is differences between the assumed boundary conditions applied in half-space approximations and those of the actual fibre subjected to force. More specifically, half-space theory requires that stresses/strains vanish as distance from the point of contact increases. However, inspection of Figure C-3c shows that for the bare D-shape fibre there is a stress, or pressure, P, boundary condition that extends along the boundary of the flat of the D-shape clad. Although the differences in modeled and measured sensitivity are significant for the bare D-shape sensor, the half-space model served its purpose of approximating the state of stress/strain within the fibre and offering insights into increases in sensitivity of the super-structured sensor.

The super-structured force sensor addresses limitations with the authors' previous force sensor that was applied to intact cadaveric hips [19] as well as limitations with other birefringence-based FBG contact force sensors presented in the literature. Future work will include pilot experiments, similar to those presented in our past work [19], to validate the performance of the sensor for application to articular joints.

5. Conclusions

In this work a new super-structured, FBG-based, contact force sensor is presented that is based on birefringent D-shape optical fibre. The sensor addresses limitations of existing fibre-based contact force sensors that are based on FBGs in birefringent fibre, FBGs in conventional optical fibre and tilted FBGs. Relative to other birefringent fibre sensors, the sensor has contact force sensitivity comparable to the highest sensitivity of commercially available birefringent fibres and, unlike other birefringent fibre sensors, is self aligning with respect to contact forces. Unlike sensors based on Bragg gratings in conventional fibre and tilted Bragg gratings, the sensor has negligible co-sensitivity to both axial strain and changes in temperature.

References

[1] Pieter, L. S., Beatrys, M. L., and Anatoli, A. C., 2005, "Chirped fiber Bragg grating sensor for pressure and position sensing," Optical Engineering, 44(5), p. 054402.

[2] Udd, E., Lawrence, C., and Nelson, D., 1997, "Development of a Three Axis Strain and Temperature Fiber Optic Grating Sensor," Proceedings of SPIE, 3042, pp. 229-236.

[3] Xu, M. G., Reekie, L., Chow, Y. T., and Dakin, J. P., 1993, "Optical in-fibre grating high pressure sensor," Electronics Letters, 29, pp. 398-399.

[4] Chehura, E., Ye, C.-C., Staines, S. E., James, S. W., and Tatam, R. P., 2004, "Characterization of the response of fibre Bragg gratings fabricated in stress and geometrically induced high birefringence fibres to temperature and transverse load," Smart Materials and Structures, 13, pp. 888-895.

[5] Yeo, T. L., Sun, T., Grattan, K. T. V., Parry, D., Lade, R., and Powell, B. D., 2005, "Characterisation of a polymer-coated fibre Bragg grating sensor for relative humidity sensing," Sensors and Actuators B: Chemical, 110, pp. 148-155.

[6] Fernandez, A. F., Brichard, B., Berghmans, F., and Decreton, M., 2002, "Dose-Rate Dependencies in Gamma-Irradiated Fiber Bragg Grating Filters," IEEE Transactions on Nuclear Science, 49(6), pp. 2874-2878.

[7] Lawrence, C. M., Nelson, D. V., and Udd, E., 1996, "Multi-Parameter Sensing with Fiber Bragg Gratings," Proceedings of SPIE, 2872, pp. 24-31.

[8] Udd, E., 1991, Fibre Optic Sensors, An Introduction for Engineers and Scientists, Wiley InterScience.

[9] Liu, Y., Guo, Z., Zhang, Y., Seng, K., Dong, C., and Dong, X., 2000, "Simultaneous pressure and temperature measurement with polymer-coated fibre Bragg grating," Electronics Letters, 36(6), pp. 564-566.

[10] Nunes, L. C. S., Valente, L. C. G., Llerena, R. W. A., Braga, A. M. B., and Triques, A. L. C., 2004, "Simultaneous measurement of temperature and pressure using single fiber Bragg grating and fixed filter demodulation technique," Proceedings of SPIE, 5622, pp. 906-911.

[11] Sun, A., Qiao, X. G., Jia, Z. A., Li, M., and Zhao, D. Z., 2005, "Study of simultaneous measurement of temperature and pressure using double fiber Bragg gratings with polymer package," 44(3), p. 034402.

[12] Measures, R. M., 2001, Structural Health Monitoring with Fiber Optic Technology, Academic Press.

[13] Okamoto, K., Hosaka, T., and Edahiro, T., 1981, "Stress analysis of optical fibers by a finite element method," IEEE Journal of Quantum Electronics, QE-17(10), pp. 2123-2129.

[14] Barlow, A. J., and Payne, D., 1983, "The stress-optic effect in optical fibers," IEEE Journal of Quantum Electronics, QE-19(5), pp. 834-839.

[15] Zhao, D., Zhou, K., Chen, X., Zhang, L., Bennion, I., Flockhart, G., MacPherson, W. N., Barton, J. S., and Jone, J. D. C., 2004, "Implementation of vectorial bend sensors using long-period gratings UV-inscribed in special shape fibres," Measurement Science and Technology, 15, pp. 1647-1650.

[16] Udd, E., Nelson, D., and Lawrence, C., 1996, "Three Axis Strain and Temperature Fiber Optic Grating Sensor," Proceedings of SPIE, 2718, pp. 104-109.

[17] Wierzba, P., and Kosmowski, B. B., 2003, "Application of polarisation-maintaining side-hole fibres to direct force measurement," Opto-Electronics Review, 11(4), pp. 305-312.

[18] Abe, I., Frazao, O., Schiller, M. W., Noqueira, R. N., Kalinowski, H. J., and Pinto, J. L., 2006, "Bragg gratings in normal and reduced diameter high birefringence fibre optics," Measurement Science and Technology, 17, pp. 1477-1484.

[19] Dennison, C. R., Wild, P. M., Wilson, D. R., and Gilbart, M. K., 2010, "An in-fiber Bragg grating sensor for contact force and stress measurements in articular joints," Measurement Science and Technology, 21, p. 115803.

[20] Wilson, D. R., McWalter, E. J., and Johnston, J. D., 2008, "The measurement of joint mechanics and their role in osteoarthritis genesis and progression," Rheumatic Disease Clinics of North America, 34, pp. 605-622.

[21] Anderson, A. E., Ellis, B. J., Maas, S. A., Peters, C. L., and Weiss, J. A., 2008, "Validation of finite element predictions of cartilage contact pressure in the human hip joint," Journal of Biomechanical Engineering, 130, p. 10pp.

[22] Cottrell, J. M., Scholten, P., Wanich, T., Warren, R. F., Wright, T. M., and Maher, S. A., 2008, "A new technique to measure the dynamic contact pressures on the tibial plateau," Journal of Biomechanics, 41, pp. 2324-2329.

[23] Shao, L.-Y., Jiang, Q., and Albert, J., 2010, "Fiber optic pressure sensing with conforming elastomers," Applied Optics, 49(35), pp. 6784-6788.

[24] Hill, K. O., Fujii, Y., Johnson, D. C., and Kawasaki, B. S., 1978, "Photosensitivity in optical fiber waveguides: Application to reflection filter fabrication," Applied Physics Letters, 32(10), pp. 647-649.

[25] Huang, S., LeBlanc, M., Ohn, M. M., and Measures, R. M., 1995, "Bragg intragrating structural sensing," Applied Optics, 34(22), pp. 5003-5009.

[26] Noda, J., Okamoto, K., and Sasaki, Y., 1986, "Polarization maintaining fibers and their applications," Journal of Lightwave TEchnology, 4(8), pp. 1071-1089.

[27] Mendez, A., and Morse, T. F., 2007, Specialty optical fibers handbook, Academic Press.

[28] Kumar, A., Gupta, V., and Thyagarajan, K., 1987, "Geometrical birefringence of polished and D-shape fibers," Optics Communications, 61(3), pp. 195-198.

[29] Urbanczyk, W., Martynkien, T., and Bock, W. J., 2001, "Dispersion effects in elliptical-core highly birefringent fibers," Applied Optics, 40(12), pp. 1911-1920.

[30] Johnson, K. L., 1987, Contact mechanics, Cambridge University Press.

[31] Xu, M. G., Geiger, H., and Dakin, J. P., 1996, "Fibre grating pressure sensor with enhanced sensitivity using a glass-bubble housing," Electronics Letters, 32, pp. 128-129.

[32] Yamate, T., Ramos, R. T., Schroeder, R. J., and Udd, E., 2000, "Thermally insensitive pressure measurements up to 300 degree C using fiber Bragg gratings written onto side hole single mode fiber," Proceedings of SPIE, 4185, pp. 628-632.

[33] Norton, R. L., 2000, Machine Design, An integrated approach, Prentice Hall.

[34] Kou, J.-I., Huang, Z.-d., Zhu, G., Xu, F., and Lu, Y.-q., 2010, "Wave guiding properties and sensitivity of D-shaped optical fiber microwire devices," Applied Physics B: Lasers and Optics, DOI 10.1007/s00340-010-4244-y.